Print ISSN 0033-9008
Online ISSN 1880-1765

QUARTERLY REPORT of RTRI

Aug. 2025 Vol. 66 No. 3

CONTENTS

[H] Human factors
[I] Infrastructure
[N] Natural hazards
[O] Operations
[R] Rolling stock
[T] Technical system integration and interaction

RAILWAY TECHNICAL RESEARCH INSTITUTE

QUARTERLY REPORT of RTRI

Print ISSN 0033-9008
Online ISSN 1880-1765

August 2025 Vol. 66 No. 3

CONTENTS

PAPERS

SUMMARIES

[H] Human factors
[I] Infrastructure
[N] Natural hazards
[O] Operations
[R] Rolling stock
[T] Technical system integration and interaction

Development of Gaze Allocation Data Feedback System for Train Drivers

Daisuke SUZUKI **Fumitoshi KIKUCHI**
Ergonomics Laboratory, Human Science Division

Takaharu KOIKE
Emovis Corporation

This study aimed at developing a gaze allocation data feedback system for conducting driving simulator training using quantitative gaze data of train drivers. The system can preset driving scenes to efficiently instruct trainees within a limited training time. The system can also compare trainees with experts using face direction data and gaze target data graphs to clarify the characteristics of trainee allocation of visual attention. In addition, the system can visualize the gaze allocation data and clearly show the objects that trainees were looking at while driving a simulator. Instructors from a railway company tested the system and gave a positive evaluation of it as a training tool for trainee visual attention.

Key words**:** *gaze, support for reflection, train driving simulator, training*

1. Introduction

1.1 Background and purpose

Train drivers are required to deal with various abnormal events, such as signal problems and obstacles on the track. In order to improve driver skills in dealing with abnormal events, railway operating companies often conduct vocational training sessions using a driving simulator. Endoh [1] proposed a vocational training program to improve train driver skills for dealing with abnormal events promptly and accurately. The training program included a support system for reflection (Fig. 1), in which drivers could review video recordings of their behavior while driving the simulator and reflect on their psychological condition and reactions to abnormal events.

However, for quick detection of abnormal events, the way drivers allocate their visual attention is crucial. In previous studies in the railway field, Yamauchi [2] and Yamauchi et al. [3] argued that evidence-based instruction is effective for railway crew education. It therefore follows that for visual attention allocation, training that uses gaze allocation data to allow trainees to reflect objectively on where they place their visual attention should be effective. In previous studies in the automobile field, Zhang et al. [4] have indicated that training supported by numerical data improved outcomes. They proposed that a driver's gaze allocation, like any other action, can be developed by observing the behavior of a role model, calling this approach "training based on experienced drivers' performance."

Fig. 1 Example of screen of the support system for reflection

They carried out an experiment using a driving simulator to select drivers with the best gaze allocation and obtained video footage of gaze allocation to produce training videos on hazard perception. Their results showed that among novice drivers who received video training, the training based on the experienced drivers' performance helped novice drivers improve their visual hazard perception. According to the previous study, the visual attention of novice drivers can be improved by watching and learning the gaze allocation techniques of experienced drivers.

This study therefore aimed to develop a gaze allocation data feedback system that would allow trainees to reflect on their visual attention immediately after driving a simulator, using an eye-tacking method without driver fatigue. In this study, "feedback" refers to the objective data given to trainees, which is based on the results of their behavior, and related necessary knowledge.

1.2 Literature review of gaze allocation

Several studies have investigated gaze allocation by train drivers. Luke et al. [5] analyzed the gaze allocation of 86 drivers while operating in-service trains to investigate how signal aspect, i.e., the color of a signal, influenced driver gaze allocation and showed that the preceding aspect, the color of the next signal, and signal complexity were important factors that affect driver gaze allocation. Naweed and Balakrishnan [6] examined the tasks and activities of urban passenger-train drivers to understand the nature of visual attention in their driving activities and showed that driving in an urban environment required the mastery of gaze allocation skills. Groeger et al. [7] investigated the gaze allocation of 10 train drivers and showed that approximately 50% of the time spent approaching signals was used to scan the visual scene. The remaining time was spent looking at railway signage and infrastructure, trackside locations, and signals. Although previous studies have investigated ordinary railway-driving situations, few have examined a training method using objective data to detect abnormal events.

It is important to investigate the relationship between gaze allocation and the detection of abnormal events in railway driving. The authors [8] previously examined an effective gaze allocation during coasting at a high speed of approximately 90 km/h and showed that long periods of looking straight far ahead contributed to the detection of abnormal events. Furthermore, the authors [9] investigated

an effective gaze allocation while accelerating at a low speed of approximately 30 km/h and showed that drivers who were able to detect abnormal events looked ahead more widely with short glances. The authors [10] showed that the failure to detect abnormal events was due to excessive concentration on looking straight ahead.

There have been many studies in the field of automobile research that have attempted to correlate gaze allocation with driver skill levels. Mourant and Rockwell [11] investigated differences in gaze allocation by novice and experienced drivers and indicated that the novice drivers concentrated their gaze in a smaller area than experienced drivers did. Crundall and Underwood [12] investigated the differences between novice and experienced drivers in gaze allocation under different levels of cognitive load imposed by different road types and found a significant difference between experienced and novice drivers on the dual carriageway. Experienced drivers had a wider search spread along the horizontal axis than novices. Underwood et al. [13] observed how experienced drivers looked at a road scene while watching a video recording taken from a traveling car. The effect of the driving experience was that experienced drivers had increased variance in their gaze as compared with novices. Konstantopoulos et al. [14] focused on experience-related differences in gaze allocation. Their results showed that driving instructors had a broader spread of gaze in the horizontal axes than learner drivers did. According to these previous studies, experience-related differences led to differences in driver gaze allocation, and a wider range of gaze was an effective gaze allocation characteristic adopted by experienced drivers.

In this way, many studies have reported that the gaze allocation of experts differs from that of novices. Regarding the training method to help novices become experts, one of the effective methods is for novices to receive feedback on their own gaze allocation data and reflect on the differences between the characteristics of novices and experts.

2. Development of gaze allocation data feedback system

In order to conduct training using gaze allocation data, we developed a gaze allocation data feedback system that provides trainees with feedback on the gaze allocation data measured while driving a simulator immediately after driving a simulator. The gaze allocation data feedback system consists of a "function of measuring gaze and determining gaze target" and a "function of aggregating and displaying gaze allocation data."

2.1 Function of measuring gaze and determining gaze target

2.1.1 Eye tracking system

We used EMR ACTUS made by nac Image Technology Inc. to measure gaze. EMR ACTUS used two cameras to capture the images of the head and eyes (Fig. 2). Its features were to measure gaze without contact and calibration. In order to collect gaze data during actual training, it is important to measure gaze without putting a burden on the drivers. Furthermore, in order to collect gaze allocation data similar to that during normal driving, it is also important that the drivers are not aware that their gaze is being measured. In addition, since simulator training time is limited during actual training, it is necessary to collect gaze allocation data efficiently without spending time on calibration. Taking these points into consideration, we used a method that could measure gaze without contact and calibration.

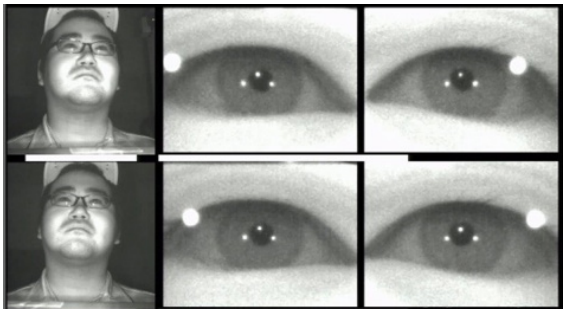

Fig. 2 Imagines of a head and eyes captured (Citation from reference [16])

2.1.2 Determining face direction and measuring gaze

Taking into account the characteristics of the eye mark recorder, the gaze-measuring range was set to be within the front screen of the driving simulator. When driving a train, it is important for the drivers to look not only at the track ahead, but also at the speedometer and timetable in the cab. Therefore, we used image analysis to calculate the amount of head rotation and tilt, determining the face direction (forward, timetable, speedometer, and driver's desk) (Figs. 3 and 4).

In order to determine the threshold for determining face direction, we carried out an experiment to measure face direction while driving a simulator. The participants were four employees of the

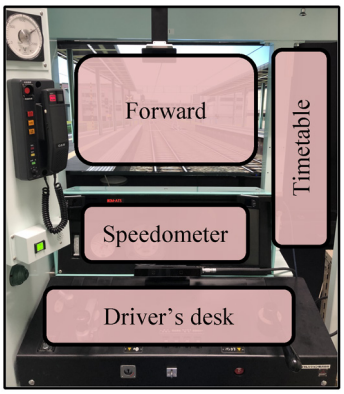

Fig. 3 Area of face direction

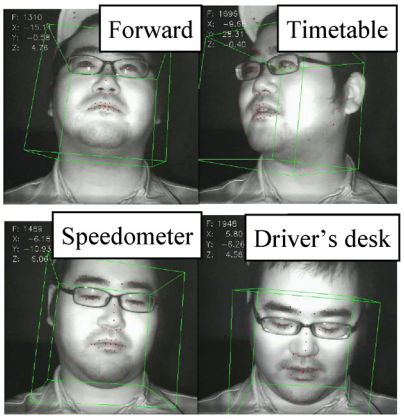

Fig. 4 Calculating the amount of head rotation and tilt (Citation from reference [16])

Table 1 Participant attributes and results of determining face direction

Participants		A	B	C	D
Attributes	Sex	F	M	F	M
	Glasses	w/o	w/	w/o	w/
Determining face direction	Forward (%)	85	94	92	91
	Timetable (%)	5	3	3	4
	Speedometer (%)	7	2	4	4
	Driver's desk (%)	3	1	1	1

Railway Technical Research Institute (two males and two females). While driving between stations in the driving simulator, the participants were verbally instructed to look at the timetable, the speedometer, and the driver's desk. The instructions were given twice between each station. From the data of the face angle while gazing at the timetable, the speedometer, and the driver's desk, we set the threshold for determining the direction that the participants were facing. Table 1 shows the participants' attributes and the results of the face direction determination. Regarding the timetable, speedometer, and driver's desk, we confirmed that we could determine the face direction using image analysis. We compared the video footage with the face direction results determined by the image analysis and confirmed that the face direction results determined by the image analysis were generally consistent with the face direction results determined by the video footage.

After determining whether the participant's face was directed inside or outside the front screen (timetable, speedometer, and driver's desk), we measured the participant's eye movement on the screen and extracted the location of gaze when the face was directed inside the front screen.

2.1.3 Determining gaze target

Since a feature of train driving is that the scene ahead (the location of a traffic signal or a traffic sign etc. on the front screen) is exactly the same when the distance is the same, we measured the coordinates of each object (a traffic signal or a traffic sign, etc.) on the front screen for each distance (in 0.1 m increments), and generated the object area data. We used an OI-Editor made by Emovis Corporation to generate the object area data. After specifying the rectangle of an object on the front screen, the OI-Editor output the data of the continuous rectangular coordinate using object tracking processing while the video was playing. The OI-Editor added frame information from the video to the data of the continuous rectangular coordinate, referring to the distance information in the driving simulator log file, and generated object area data for each distance (Fig. 5). For object tracking, the original video was played in reverse.

After the trainees had completed their training drive, we compared the rectangular data of each object with the location of each gaze on the front screen to determine what they were looking at (Fig. 6). We confirmed that it is possible to automatically determine the objects that the trainee was gazing at while driving a simulator by using the pre-generated object area data for each distance.

2.2 Function of aggregating and displaying gaze allocation data

To compare drivers, we aggregated driving data output from the driving simulator (driving speed, powering notch, braking notch), face direction data, and gaze target data based on distance. Figure 7 is a screenshot of the gaze allocation data feedback system. The display of the gaze allocation data feedback system consists of three areas: (1) Area for setting the driving context, (2) Graph display, and (3) Video display.

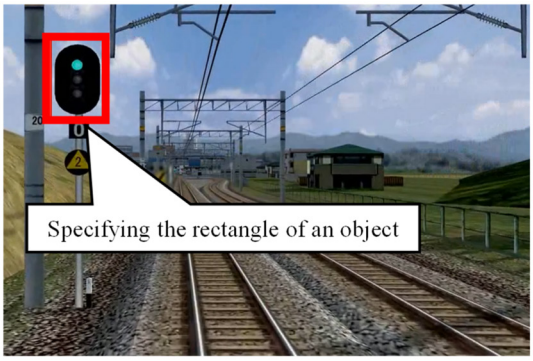

(A) Initial specifying of an object

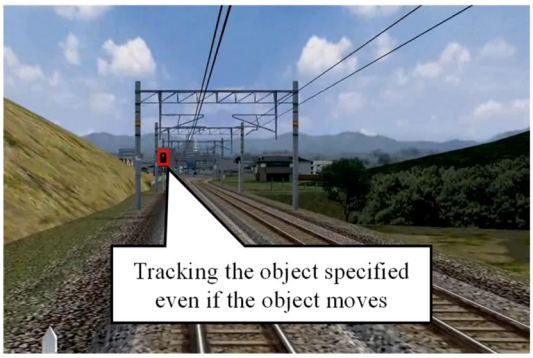

(B) Tracking the object specified initially

Fig. 5 Generating object area data

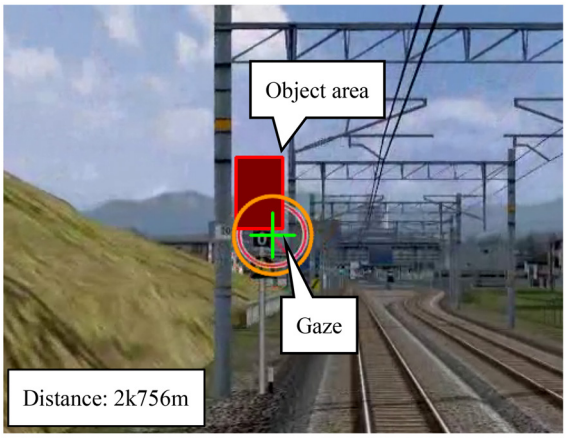

Fig. 6 Image of determining a gaze target

2.2.1 Area for setting the driving context

The area for setting the driving context allows the instructor to select pre-defined driving moments to focus on, according to the purpose of the training. For example, approaching a station or crossing a level crossing. As the time available for actual simulator train-

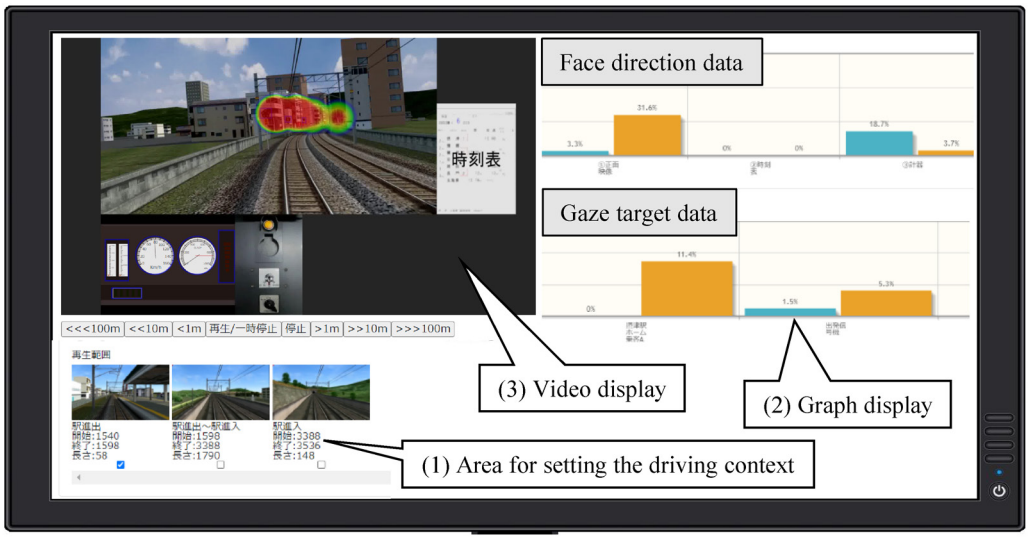

Fig. 7 Display example of gaze allocation data feedback system

ing is limited, it is difficult to watch through the entire recorded video of a training session. For example, if the total simulator training time is 60 minutes and the simulated driving time is about 40 minutes, this leaves only about 20 minutes to review the gaze allocation data. The driving situation setting allows the instructor to pre-select the driving moments that trainees should review to reflect on their gaze allocation. This contributes to efficient reflection even in limited training time.

2.2.2 Graph display

The graph display collects and displays data on face direction and gaze target, comparing a trainee's data with that of another driver to identify characteristics of the trainee's visual attention. For example, face direction data show whether a trainee tends to look more or less frequently at the front scene or at the speedometer. Additionally, gaze target data show the number of times a trainee looks at traffic lights or level crossings in the scene ahead.

2.2.3 Video display

The video display visualizes gaze data. For example, instructors can instantly switch between a trainee's gaze and another driver's gaze, showing the difference in what they were looking at in the exact same scene.

2.3 Using the gaze allocation data feedback system

We explain how to use the gaze allocation data feedback system with an example that uses the gaze data of an experienced driver as benchmark data.

First, instructors set up the target driving scenarios, such as train delays or receiving operational notifications. An experienced driver then drives the simulator to provide benchmark data. The instructor then talks through this with the experienced driver to find out what they paid attention to when looking ahead while driving. For example, immediately after running through a curve, the experienced driver paid visual attention to an obstruction warning signal for a level crossing. Based on this interview, the instructor identifies key driving points to focus and reflect on during and after the training. For example, the focal driving situation would extend from the location of the obstruction warning signal for a level crossing to the location of the level crossing. The instructor also specifies the objects that drivers should pay visual attention to in each driving situation. For example, departure signals, passengers on platforms, obstruction warning signals for level crossings, level crossings, signs, etc.

Next, the trainees are asked to drive the simulator. Just after the simulator exercise, the instructor then provides feedback on their gaze allocation data, and they reflect on their driving. For example, the gaze target data show that the experienced driver often looked at the obstruction warning signal, whereas the trainee looked at it less often. After that, the instructors provide guidance based on the visualization of the gaze data. Figure 8 shows an example of the visualization of gaze allocation data looking ahead. By comparing what

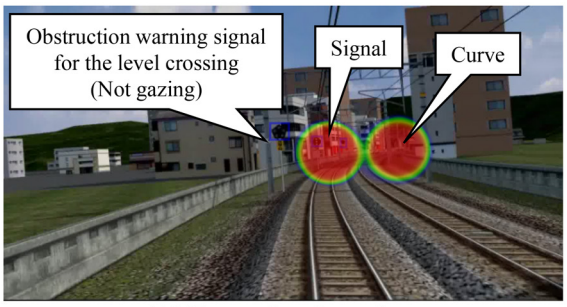

(A) Example of a trainee

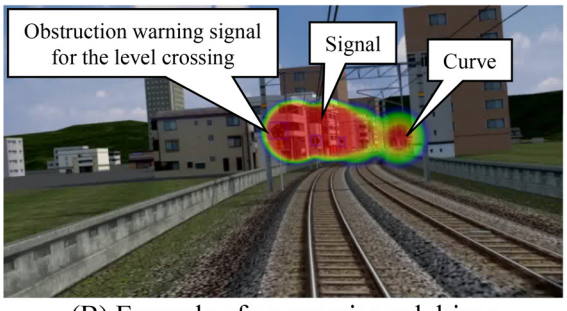

(B) Example of an experienced driver

Fig. 8 Example of visualizing the gaze allocation data in a front scenery

the trainee was looking at with what the experienced driver was looking at in the same scene, it is possible to verify that the trainee was only looking at the traffic lights and the curve ahead, whereas the experienced driver was clearly looking not only at the traffic lights and the curve ahead but also at the obstruction warning signals for the level crossing. In this way, the instructors can confirm the characteristics of visual attention and provide specific guidance to the trainee for improvement using visualized gaze allocation data.

3. Evaluation of the effectiveness of the gaze allocation data feedback system

In order to evaluate the effectiveness of the gaze allocation data feedback system, we installed the system on a driving simulator equipped with an eye tracker used by a railway operating company. Figure 9 shows the eye mark recorder installed. Four instructors involved in simulator training tried it out and answered questions about its effectiveness in training (Fig. 10). As a result, we received positive feedback, such as, "This system is a tool that makes it possible to provide instruction about the driver's visual attention that was not possible before," "This system makes it possible to provide more convincing instruction based on data," and "This system makes it possible to provide efficient instruction by aggregating data with the distance."

4. Conclusions

In this study, in order to implement simulator training using gaze allocation data, we developed a system called the gaze allocation data feedback system. This system provides trainees with feedback on their gaze allocation data measured during simulated driving immediately after driving a simulator. By using the gaze allocation data feedback system, instructors can specify which pre-defined driving moments from the recordings will form the focus of instruction. Instructors can then invite trainees to reflect on their gaze allocation data efficiently within the limited training time. In addition, with graphs of the face direction data and gaze target data, instructors can understand the characteristics of the trainees' visual attention compared with those of experienced drivers. Furthermore, with videos that visualize gaze allocation data, instructors can clearly show trainees the differences in visual attention between trainees and experienced drivers when they look at exactly the same scene. Instructors involved in simulator training at a railway operating company trialed the system and gave a positive evaluation.

Further study is needed to investigate how this system can be integrated with actual simulator training and how feedback on gaze allocation data for each training scenario can be provided.

This study was published in RTRI Report (in Japanese) [15] in 2024. Part of this paper was published in reference [16].

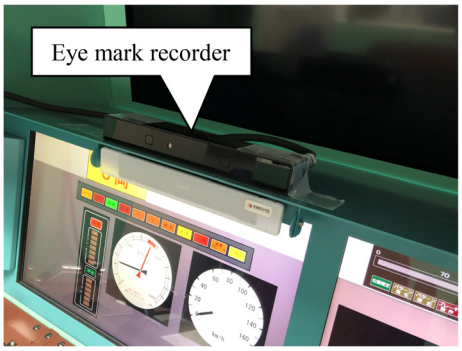

Fig. 9 Eye mark recorder installed in the experiment

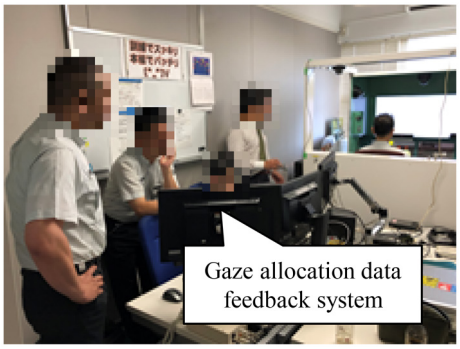

Fig. 10 Trial of the gaze allocation data feedback system

Acknowledgment

We would like to express our gratitude to the Hokkaido Railway Company and West Japan Railway Company for their considerable cooperation in the simulator training.

References

[1] Endoh, H. and Omino, K., "Practical System for Implementing Vocational Training Program for Improving Train Driver Skills for Coping with Abnormal Situations," *Quarterly Report of RTRI*, Vol. 54, No. 4, pp. 237-242, 2013.

[2] Yamauchi, K., "Evaluation and Promotion of Railways Employee Awareness about Observing Rules on Making Passenger Announcements," *Quarterly Report of RTRI*, Vol. 53, No. 4, pp. 241-246, 2012.

[3] Yamauchi, K., Kikuchi, F. and Fujinami, K., "Guidelines for Making Emergency Announcements Taking into Consideration the Psychological State of Passengers," *Quarterly Report of RTRI*, Vol. 58, No. 2, pp. 153-158, 2017.

[4] Zhang, W., Wang, Y., Feng, Z., Zhu, S., Cui, J., Hao, W. and Wang, C., "A method to improve the hazard perception of young novice drivers based on Bandura's observational learning theory: Supplement to expert commentary training," *Transportation Research Part F*, Vol. 85, pp. 133-149, 2022.

[5] Luke, T., Brook-Carter, N., Parkes, A. M., Grimes, E. and Mills, A., "An investigation of train driver visual strategies," *Cognition, Technology and Work*, Vol. 8, pp. 15-29, 2006.

[6] Naweed, A. and Balakrishnan, G., "Understanding the visual skills and strategies of train drivers in the urban rail environment," *Work*, Vol. 47, pp. 339-352, 2014.

[7] Groeger, J. A., Bradshaw, M. F., Everatt, J., Merat, N. and Field, D., "Pilot study of train drivers' eye-movements," *University of Survey Technical Report for Rail Safety and Standards Board*, London, 2003.

[8] Suzuki, D., Yamauchi, K. and Matsuura, S., "Identifying the effects of visual searching by railway drivers upon the recognition of extraordinary events," *presented at the 20th Congress of the International Ergonomics Association*, Florence, Italy, August 26-30, 2018, pp. 165-173.

[9] Suzuki, D., Yamauchi, K. and Matsuura, S., "Effective Visual

Behavior of Railway Drivers for Recognition of Extraordinary Events," *Quarterly Report of RTRI*, Vol. 60, No. 4, pp. 286-291, 2019.
[10] Suzuki, D., Koike, T. and Kawarai, R., "Identifying effective visual searching for the recognition of extraordinary events during the acceleration process of railway driving," *presented at the 22nd Congress of the International Ergonomics Association*, Jeju, Korea, August 25-29, 2024.
[11] Mourant, R. R. and Rockwell, T. H., "Strategies of visual search by novice and experimental drivers," *Human Factors*, Vol. 14, pp. 325-335, 1972.
[12] Crundall, D. E. and Underwood, G., "Effects of experience and processing demands on visual information acquisition in drivers," *Ergonomics*, Vol. 41, pp. 448-458, 1998.
[13] Underwood, G., Chapman, P., Bowden, K. and Crundall, D., "Visual search while driving: Skill and awareness during inspection of the scene," *Transportation Research Part F*, Vol. 5, pp. 87-97, 2002.
[14] Konstantopoulos, P., Chapman, P. and Crundall, D., "Driver's visual attention as a function of driving experience and visibility. Using a driving simulator to explore drivers' eye movements in day, night and rain driving," *Accident; Analysis and Prevention*, Vol. 42, pp. 827-834, 2010.
[15] Suzuki, D., Kikuchi, F. and Koike, T., "Development of a Gaze Distribution Data Feedback System for Train Drivers," *RTRI Report*, Vol. 38, No. 11, pp. 71-77, 2024 (in Japanese).
[16] Suzuki, D., Matsuura, S., Koike, T. and Matsuu, K., "Gaze Data Feedback System on Railway Driving Simulator," *The Japanese Journal of Ergonomics*, Vol. 55, Supplement, 1B1-5, 2019 (in Japanese).

Authors

Daisuke SUZUKI, Ph.D.
Senior Researcher, Ergonomics Laboratory, Human Science Division
Research Areas: Safety Ergonomics, Human Factors

Fumitoshi KIKUCHI, Ph.D.
Senior Researcher, Ergonomics Laboratory, Human Science Division
Research Areas: Social Psychology, Emotional Psychology

Takaharu KOIKE
Emovis Corporation
Research Areas: Eye Tracking, Gaze Analysis

Evaluation of Shear Capacity of RC Pile Head Based on Equivalent Shear Span Method

Yuki NAKATA
Concrete Structures Laboratory, Structures Technology Division

Haruyuki KITAGAWA
Structural Mechanics Laboratory, Railway Dynamics Division

Ken WATANABE
Concrete Structures Laboratory, Structures Technology Division

Toshiya TADOKORO
Structures Technology Division

In the verification of reinforced concrete (RC) piles, the design shear capacity V_{yd} of linear members is used based on the experimental results of simply supported RC beams. On the other hand, since RC piles are subjected to ground reaction forces, the shear capacity may be greater than V_{yd}, unlike simply supported conditions. In this paper, we have used nonlinear finite element analysis to evaluate the shear capacity of RC pile heads taking into account ground reaction forces. We have shown that the equivalent shear span method, which is applied to the analysis of slabs of underground box structures, can also be applied to the analysis of RC pile heads.

Key words**:** *RC pile head, shear capacity, equivalent shear span method, finite element analysis*

1. Introduction

The calculation equation of the design shear strength V_{yd} for linear members in concrete structures is given in the Design Standard for Railway Structures and Commentary (Concrete Structures) [1] (the concrete standard). It is set on the conservative side based on the results of experiments on reinforced concrete (RC) rectangular cross-section beams subjected to simply supported concentrated loads. On the other hand, RC piles are characterized by having a circular cross section, being subject to axial forces and distributed loads due to ground reaction forces, and often having an inflection point in the moment distribution at the pile head. In such cases, the shear capacity of the pile head may be greater than V_{yd} [2].

Note that the concrete standard in the 2023 edition sets an upper limit on the effect of shear reinforcement in V_{yd} [1, 3]. Recent design examples have shown that shear reinforcement in the heads of cast-in-place RC piles is often placed above this upper limit. According to V_{yd}, which takes into account the upper limit of the effect of shear reinforcement, it would be necessary to change the concrete strength and cross-sectional dimensions, even though the actual shear capacity of the RC piles may be large.

On the other hand, the use of nonlinear finite element analysis (FEM) makes it to possible to evaluate the capacity in accordance with actual specifications, load and support conditions, etc. However, because RC piles are frequently used members, if the scope of application of calculation equations based on the load-bearing mechanism can be clarified in the verification of the shear capacity of the pile head, it will not be necessary to rely on FEM every time, which is thought to lead to a reduction in the labor required for the verification process.

The purpose of this study is to evaluate the load-bearing mechanism and shear capacity of full-scale RC piles using FEM, considering ground reaction forces (distributed load). Based on the results obtained by FEM, we then decided to verify the applicability of the equivalent shear span method [4, 5] to the RC pile heads, with a view to using it in verification by frame analysis. In addition, the study focused on the shear capacity at the RC pile heads, which have a flexural moment inflection point, when the structure is subjected to inertial forces due to an earthquake.

2. Research for design examples

Figure 1 shows the relationship between pile diameter and $p_w \cdot f_{wyd}/f'_{cd}$ (p_w: shear reinforcement ratio, f_{wyd}: design yield strength of shear reinforcement, f'_{cd}: design compressive strength of concrete). Generally, the amount of shear reinforcement in piles is stepped down so that it is less toward the tip of the pile. Here, however, the pile is divided into the pile head (2D section from the pile head, D: pile diameter) and the underground section (outside the 2D section). In addition, the concrete standard sets an upper limit for the calculation of V_{yd} as $p_w \cdot f_{wyd}/f'_{cd} \leqq 0.1$. In this paper, p_w is calculated using the side length b_w of an equal-area square as $p_w = A_w/(b_w \cdot s_s)$ (A_w: total area of the shear reinforcement in section s_s (mm^2), s_s: spacing of the shear reinforcement (mm)), and the reduction factor [1, 6] related to the construction conditions of concrete is taken into account for f'_{cd} in $p_w \cdot f_{wyd}/f'_{cd}$.

As can be seen from the figure, the pile diameter was 1 m to 2 m. Regarding $p_w \cdot f_{wyd}/f'_{cd}$, there is a tendency that $p_w \cdot f_{wyd}/f'_{cd} > 0.1$ at the pile head and $p_w \cdot f_{wyd}/f'_{cd} < 0.1$ at the underground. Therefore, when verifying using V_{yd}, it may be necessary to change the specifications of the pile by verifying the pile head, taking into account the upper limit of $p_w \cdot f_{wyd}/f'_{cd} \leqq 0.1$.

Figure 2 shows the relationship between the ratio a_1/D of the distance a_1 from the pile head to the flexural moment inflection point and the pile diameter D, and the axial stress σ_d at the pile head. The axial stress σ_d is the axial force of the pile divided by the cross-sectional area of the pile and gives the maximum value (tension side) and minimum value (compression side) when axial force fluctuations are taken into account. In addition, the results are from a static

nonlinear analysis that takes into account only the inertial forces during an earthquake using a two-dimensional frame analysis. They are shown separately for loading in the direction of the bridge axis and for loading perpendicular to the bridge axis. The results are from a two-dimensional frame analysis using a static nonlinear analysis that considers only the inertial force during an earthquake.

a_1/D was generally less than 2. σ_d at the pile head was approximately −7 to 3 N/mm^2 for rigid frame viaducts and −10 to 6 N/mm^2 for piers, showing a wide distribution due to axial force fluctuations.

3. Analysis Overview

3.1 Modeling of RC piles

Figure 3 shows the analysis model of RC pile. The RC pile considered in this study is based on the verification example of railway RC rigid frame viaduct [7], and is a single pile with a diameter of 1000 mm and a length of 21000 mm. A 3D model was constructed using the general-purpose nonlinear finite element analysis software DIANA ver. 10.3.

The scope of the analysis was limited to RC piles only, and the superstructure was reproduced by applying the sectional force transmitted to the RC piles as a load. The concrete was modeled using solid elements, and the reinforcing bars were modeled using embedded reinforcing bars that transmit only axial forces. The bond stress-slip relationship between the longitudinal bars and concrete was calculated by multiplying the bond stress in Shima et al.'s equation [8] by a reduction factor of 0.4. The shear reinforcement was assumed to be perfectly bonded. The stub (corresponding to the joint or footing) was assumed to be a linear elastic body.

A fixed crack model was used for the concrete. A parabolic model was used for the stress-strain relationship on the compression side, and the Hordijk model was used for the tension side. The compressive fracture energy was set at 35.3 N/mm according to Nakamura et al [9], and the tensile side was set at 0.074 N/mm according to the concrete standard. The decrease in shear stiffness due to cracking was calculated using the Al-mahaidhi model.

The mechanical properties of concrete were calculated using compressive strength, considering the reduction factor and the material coefficient γ_c related to the concrete construction conditions [1, 6].

The longitudinal bars were D32 and were made linear elastic to facilitate shear failure. The shear reinforcement bars were modeled as a bilinear model with a secondary gradient of 1/1000 of the elastic modulus, and the yield strength was set to 345 N/mm^2. The spacing was set to 125 mm, and the shear reinforcement ratio was set by arbitrarily determining the diameter of the shear reinforcement bars. The Young's modulus is 200 kN/mm^2 for all of them.

3.2 Modeling of ground reaction forces

Figure 4 shows a model of the sectional force distribution of the RC pile and Fig. 5 shows the distribution of the load applied to the RC pile. In this study, the ground was not modeled to easily set a_1/D, and the load was applied directly to the RC piles to reproduce the sectional force distribution of the RC piles due to ground reaction forces [10].

Based on previous design examples, the sectional force distribution of the RC piles was assumed to be a flexural moment distribution with an inflection point at the pile head. The concentrated load of the stub and the ground reaction forces (distributed load) of

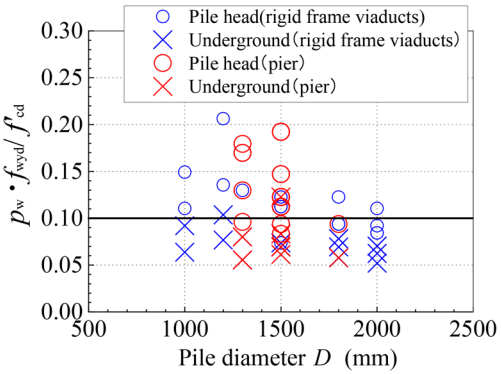

Fig. 1 Examples of pile diameter (D) and $p_w \cdot f_{wyd}/f'_{cd}$

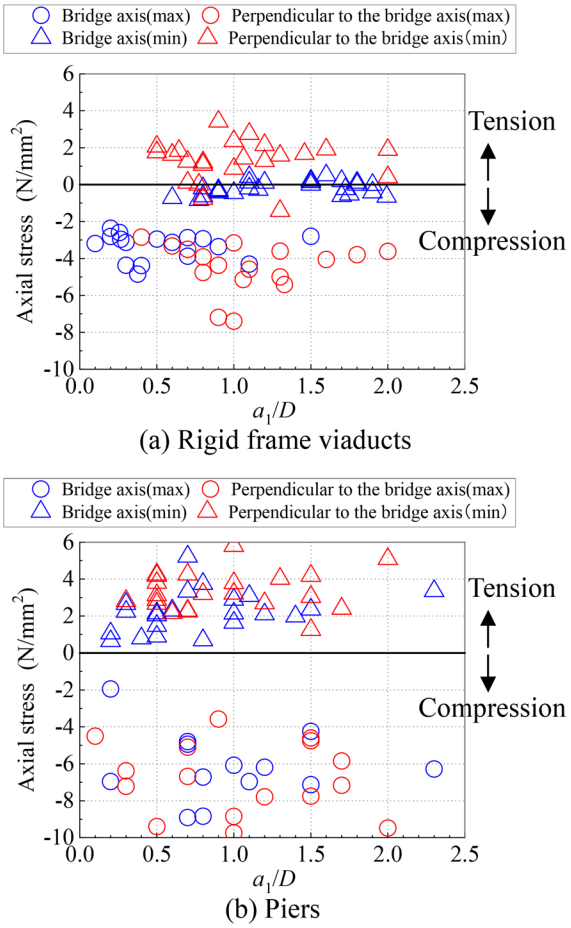

Fig. 2 Examples of relationship between a_1/D and axial stress at pile head

the piles were then applied by load control to maintain this distribution shape (Fig. 5). The flexural moment distribution at the pile head was assumed to be expressed by a quadratic function, and the lower part of the RC pile was reproduced by another quadratic function so that it was continuous with the section force at the pile head. As a result, the shear force distribution became linear, and the distributed load became uniform.

Table 1 shows the settings for each section of the flexural moment distribution. Having set the positions of the inflection points and the vertices of the quadratic function, we consider the continuity of the sectional forces at the head and bottom of the pile. The

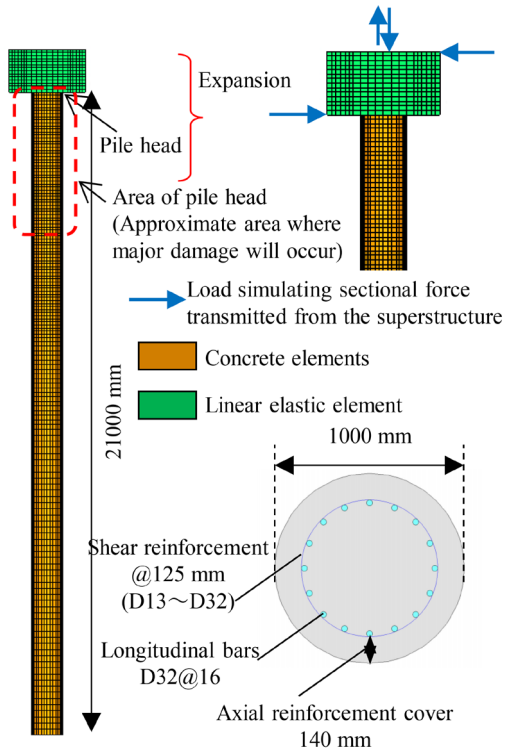

Fig. 3 Overview of analysis model

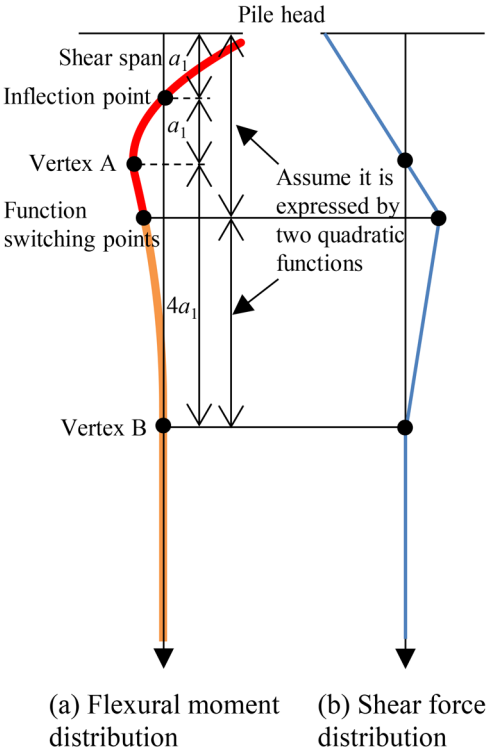

Fig. 4 Modeling of sectional force distribution

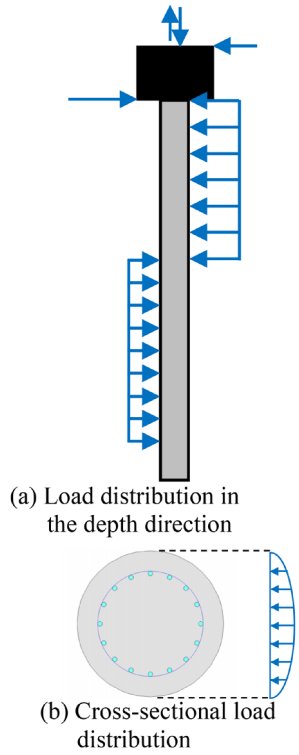

Fig. 5 Load applied to RC pile

Table 1 Setting the section for flexural moment ditribution

Flexural moment distribution interval	Ratio to a_1
Pile head - inflection point (a_1)	1
Inflection point - Vertex A	1
Vertex A - Vertex B	4

Table 2 Analysis parameters

Parameter	Value
a_1/D	0.5, 1.0, 2.0
Shear reinforcement ratiopw (%)	0.23(D13), 0.52(D19), 0.91(D25), 1.43(D32)
Axial stress (N/mm^2)	− 7(Compression), 0, 3(Tension)

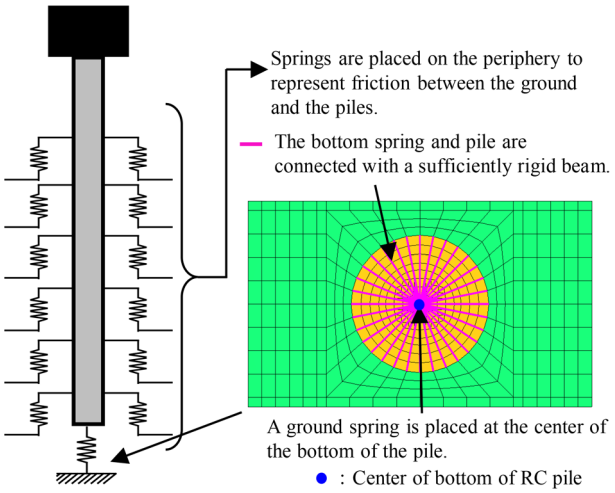

Fig. 6 Boundary conditions and arrangement of ground springs

quadratic function expressing the flexural moment distribution, the shear force distribution, and the magnitude of the distributed load acting on the RC pile are then determined. This simple, alternative modeling makes it easier to study. It has been separately confirmed that slight differences in the shape of the quadratic function or the position of vertex A and vertex B do not significantly affect the analysis results.

As shown in Fig. 5(b), the load distribution in the sectional direction of the RC pile was sinusoidal to be similar to the reaction force caused by the horizontal ground spring [6] around the pile. The axial force was reproduced by applying it to the upper edge of the stub.

Figure 6 shows the boundary conditions and the arrangement of the vertical ground spring at the tip of the pile and the vertical shear ground spring around the pile [6, 7]. The boundary conditions are fixed via the ground springs. However, the springs at the tip of the pile are connected to each node of the RC pile at the base of the pile via rigid beams and are not assumed to resist tensile forces in the axial direction of the RC pile. In addition, ground springs around the piles are not placed in the $1/\beta$ [6] area (4 m) from the pile head.

3.3 Analysis parameters

The analytical parameters are shown in Table 2. Based on Fig. 2, a_1/D was set at 0.5, 1.0, and 2.0, and the axial stress σ_d was

set at −7 (compression), 0, and 3 (tensile) N/mm^2. In addition, p_w was set at 0.23, 0.52, 0.91, and 1.43%. p_w is 0.47% when $p_w \cdot f_{wyd}/f'_{cd}$=0.1.

4. Results of analyses

4.1 Effect of a_1/D and p_w

The effect of differences in a_1/D on the shear capacity of the RC pile head was verified, under the condition where no axial force was applied.

Figure 7 shows the shear force and horizontal displacement at the pile head. The displacement increments per step from a certain horizontal displacement due to load control increases sharply compared to previous steps. Here, the shear force at the pile head of the step just before this displacement increment increases sharply was defined as the capacity V_{ana} (black circle in Fig. 7). As shown in the figure, the shear force does not increase significantly after the defined point.

Figure 8 shows the minimum principal stress distribution when p_w=0.52% and V_{ana}. In both cases, a compression strut, which is the region where the minimum principal stress occurs predominantly, is formed between the compression edge of the pile head and the position where the distributed load at the pile head (hereinafter referred to as the pile head distributed load) acts. Then, when V_{ana} is reached, a minimum principal stress equivalent to the compressive strength occurs in the compression strut.

Figure 9 shows the strain distribution of the shear reinforcement at V_{ana} when a_1/D = 1.0. The shear reinforcement at the pile head yielded at V_{ana}, but as p_w increased, the number of shear reinforcement that yielded decreased. This suggests an upper limit to the effectiveness of shear reinforcement.

Figure 10 shows the relationship between p_w and V_{ana}. Since compressive damage was significant at the pile head, the shear force at the pile head was used to evaluate the capacity of the RC piles. In addition, V_{yd} is also shown in the figure with or without consideration of $p_w \cdot f_{wyd}/f'_{cd} \leqq 0.1$. At a_1/D = 0.5, the increase in V_{ana} relative to p_w was small, and the tendency was similar to that of the shear reinforcement effect of deep beams with very small shear span ratios [11]. On the other hand, when a_1/D = 1.0, V_{ana} increased as p_w increased, and when a_1/D = 2.0, the increase rate of V_{ana} with respect to p_w became small at $p_w \geqq 0.52\%$. The shear force V_{mu} when the cross section of the pile head reaches the flexural capacity [1] is 6014 kN for a_1/D =0.5, 3007 kN for a_1/D =1.0, and 1504 kN for a_1/D =2.0. Since it is recognized that flexural compression failure occurred in the region where p_w is large for a_1/D =2.0, the actual shear capacity is considered to be greater than this.

When $p_w \cdot f_{wyd}/f'_{cd} \leqq 0.1$ was considered, V_{yd} significantly underestimated V_{ana}. However, although V_{ana} increases with increasing p_w, the rate of increase is smaller than that of V_{yd}. This is thought to be because the shape of the shear reinforcement bars are circular, so the shear reinforcement effect assumed in truss theory cannot be expected, and as p_w increases [12], the number of shear reinforcement bars that yield, decreases.

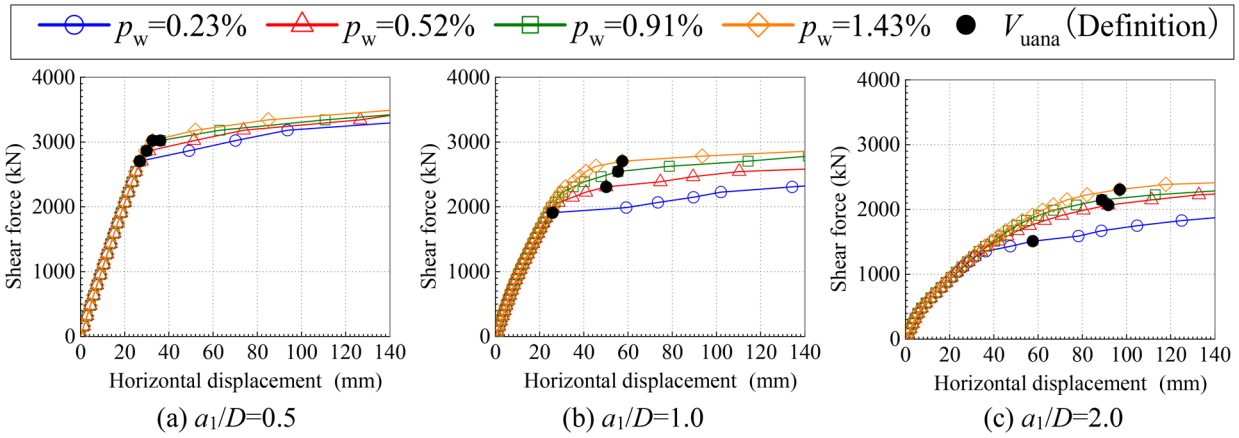

Fig. 7 Relationship between shear force and horizontal displacement at pile head (σ_d=0 N/mm^2)

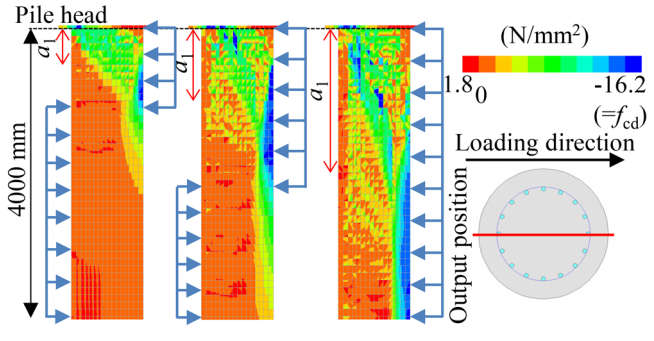

Fig. 8 Minimum principal stress distribution (V_{ana}, p_w=0.52%, σ_d=0 N/mm^2)

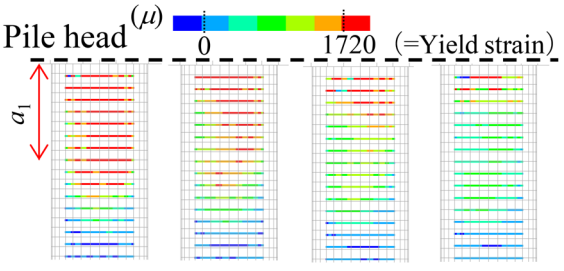

Fig. 9 Strain distribution of shear reinforcement (V_{ana}, a_1/D=0.52%, σ_d=0 N/mm^2)

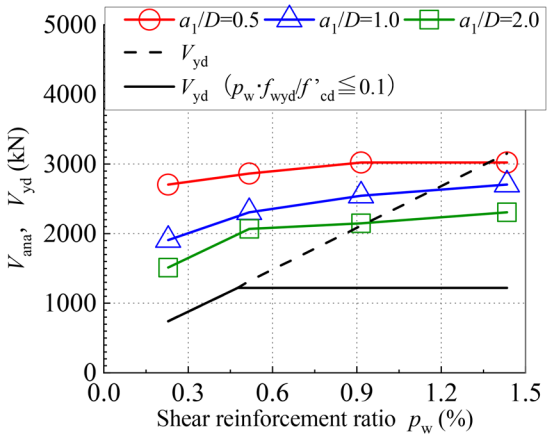

Fig. 10 Relationship between p_w and V_{ana} (σ_d=0 N/mm²)

4.2 Effect of axial force

The effect of an axial stress on the shear capacity of the RC pile head is verified when an axial stress σ_d of −7 (compression) or 3 (tension) N/mm² is applied.

Figures 11 and 12 show the minimum principal stress distribution in V_{ana} at p_w = 0.52%, σ_d = −7 N/mm² and at p_w = 0.52%, σ_d = −7 N/mm² respectively. At σ_d = −7 N/mm² (Fig. 11), the axial length of the compression strut increased, and its width also increased significantly compared to the case where a_1/D and p_w were the same at σ_d = 0 N/mm² (Fig. 8). On the other hand, at σ_d =3 N/mm²(Fig. 12), no significant difference was observed in the minimum principal stress distribution (compression struts) compared to at σ_d =0 N/mm² (Fig. 8).

Figures 13 and 14 show the relationship between p_w and V_{ana}. The effect of the axial force on V_{yd} was considered by β_n (M_0 method) [1]. At σ_d = −7N/mm², regardless of a_1/D, there was no increase in V_{ana} even when p_w increased. This is because V_{mu} was 5411 kN for a_1/D = 0.5, 2705 kN for a_1/D = 1.0, and 1352 kN for a_1/D = 2.0, and is thought to be due to shear compression failure for a_1/D = 0.5 and flexural compression failure for a_1/D = 1.0 and 2.0.

The case where σ_d = 3 N/mm² showed a similar trend to the case where σ_d = 0 N/mm². That is, when a_1/D = 0.5, the effect of p_w on V_{ana} was small, when a_1/D = 1.0, V_{ana} increased with increasing p_w, and when a_1/D = 2.0, flexural compression failure occurred with increasing p_w. In addition, V_{mu} is 6341 kN when a_1/D = 0.5, 3171 kN when a_1/D = 1.0 and 1585 kN when a_1/D = 2.0.

In comparison with V_{yd}, although it is not possible to evaluate the shear capacity in cases of flexural compression failure, considering that the shear capacity is greater than V_{mu}, it is thought that V_{yd} underestimates the shear capacity.

From the above, it is considered that compression struts are clearly formed at the head of the RC pile subjected to ground reaction forces (distributed load), and the failure mode shows shear compression failure.

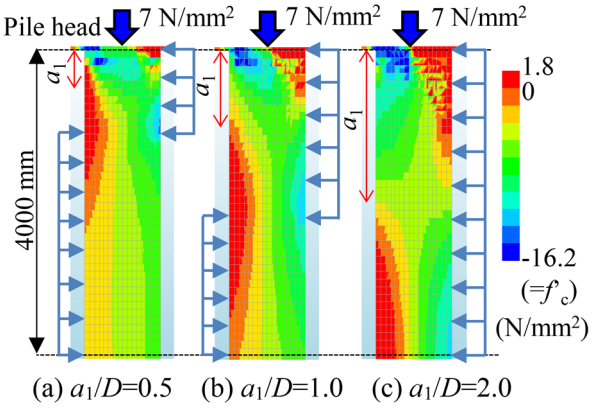

Fig. 11 Minimum principal stress distribution (V_{ana}, p_w=0.52%, σ_d=-7 N/mm²)

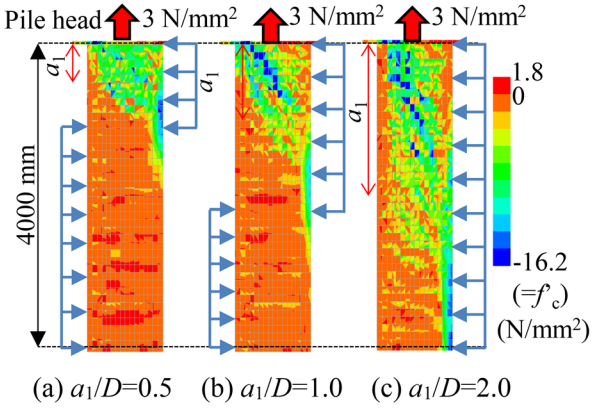

Fig. 12 Minimum principal stress distribution (V_{ana}, p_w=0.52%, σ_d=3 N/mm²)

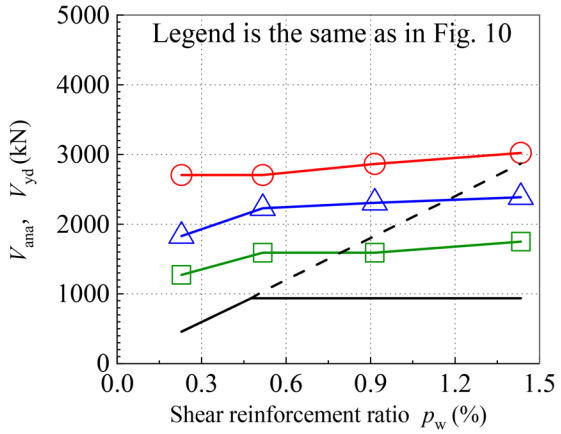

Fig. 13 Relationship between p_w and V_{ana} (σ_d=−7 N/mm²)

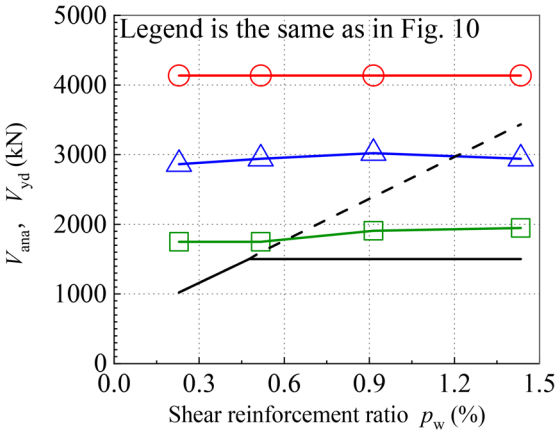

Fig. 14 Relationship between p_w and V_{ana} (σ_d=3 N/mm²)

5. Verification of applicability of equivalent shear span method

The nuclear energy guidelines [4] indicate a verification method for the top and bottom slabs and side walls of a rigid box frame structure subjected to earth pressure (distributed load) using the design shear compression capacity V_{dd} and an equivalent shear span (equivalent shear span method).

From the load bearing mechanism and failure mode obtained from the analysis, it is considered possible to apply the equivalent shear span method to evaluate the shear capacity of RC pile heads. However, the applicability of this method to RC piles was verified because the equivalent shear span and the location of the verification section were determined based on limited experimental results [4, 5], and RC piles are subject to large axial forces.

Figure 15 shows an overview of the equivalent shear span method. The distance from the pile head to the inflection point is taken as the equivalent shear span a_1, and V_{dd} is calculated using a_1. Note that based on the findings in references [1, 3], the shear capacity of the RC pile head V_{ud} is given by (1).

$$V_{ud} = \max(V_{dd}, V_{yd}) \quad (1)$$

The shear force used in the verification is the value at the position of depth $a_1/2$ [4]. At present, V_{yd} is applied at depths below the inflection point.

Figure 16 shows the relationship between p_w and the ratio of V_{ana} to V_{ud} at the position $a_1/2$. For comparison, the ratio of V_{ana} at the pile head to V_{yd} is also shown, taking into account $p_w \cdot f_{wyd}/f'_{cd} \leqq 0.1$. By applying the equivalent shear span method, V_{ana}/V_{ud} approached 1, improving the accuracy of calculation of shear capacity.

Figure 17 shows an example of verification on shear force. The pile heads of $p_w \cdot f_{wyd}/f'_{cd} > 0.1$ for RC rigid frame viaducts and RC piers recently designed under general conditions [6] were targeted. When V_{yd} was used without taking into account $p_w \cdot f_{wyd}/f'_{cd} \leqq 0.1$, the verification on shear force was satisfactory, but when V_{yd} was used taking into account $p_w \cdot f_{wyd}/f'_{cd} \leqq 0.1$, there were cases where the verification value was greater than 1.0. On the other hand, by applying the equivalent shear span method, the shear capacity and the shear forces to be considered could be rationally evaluated, and the value would be less than 1.0.

6. Conclusions

(1) When subjected to ground reaction forces (distributed load), the RC pile head having a flexural moment inflection point formed a compression strut connecting the compression edge of the pile head and the inflection point, and the failure mode was shear compression failure. It was also found that the shear reinforcement effect expected from truss theory could not be expected at the head of the RC pile.

(2) The shear capacity of the RC pile head was greater than the design shear capacity V_{yd} of the linear member taking into account $p_w \cdot f_{wyd}/f'_{cd} \leqq 0.1$.

(3) Even when subjected to axial force, the application of the equivalent shear span method improved the accuracy of calculating the shear capacity of the RC pile head.

Based on the above, it is considered that a design that relies on conventional shear reinforcement to prevent shear failure is not reasonable for the conditions considered. In the future, we will continue to perform trial calculations for various ground conditions to confirm the scope of applicability of this method, as well as to consider methods for evaluating shear capacity deep underground.

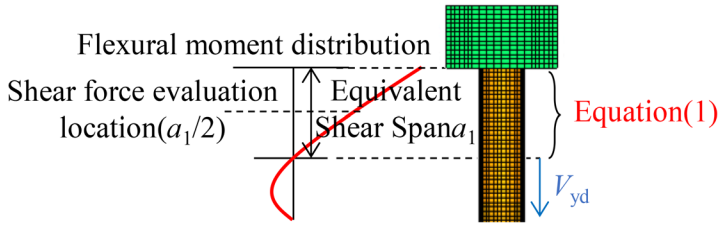

Fig. 15 Overview of the equivalent shear span method

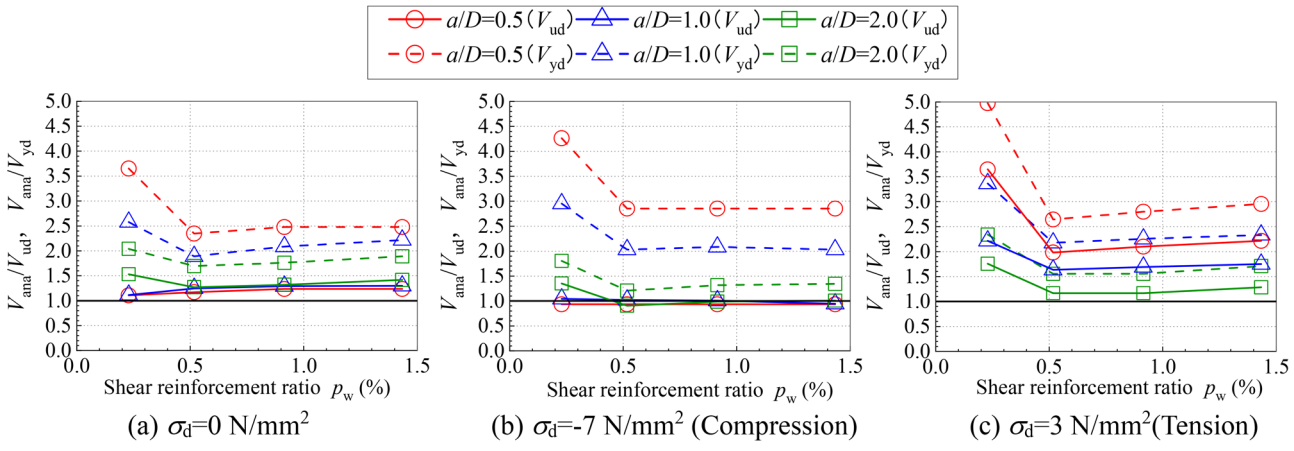

Fig. 16 Accuracy of shear capacity calculation

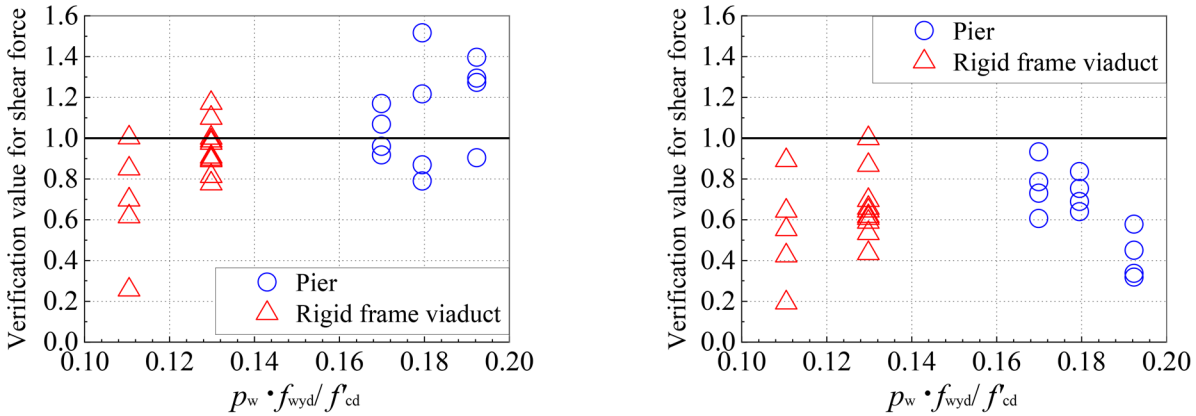

(a) V_{yd} ($p_w \cdot f_{wyd}/f'_{cd} \leqq 0.1$)　　(b) Equivalent shear span method (1)

Fig. 17　Example of verification on shear force

References

[1] Railway Technical Research Institute, *Design Standard for Railway Structures and commentary* (*Concrete Structures*). Maruzen, 2023 (in Japanese).

[2] Japan Society of Civil Engineers (351 Committee), *Design of concrete structures and evaluation method for coupled performance -Future prospect of spatiotemporal performance evaluation technology II-*, *Concrete engineering series 125*, 2020 (in Japanese).

[3] Nakata, Y., Watanabe, K. and Tanimura, Y., "Method for Calculating of the Design Shear Capacity of Reinforced Concrete Members with Continuity of Ratio of Shear-span to Effective Depth," *RTRI Report*, Vol. 38, No. 11, pp. 27-35, 2024 (in Japanese).

[4] Japan Society of Civil Engineers, *Guidelines for verification, manual and verification example of seismic performance of underground reinforced concrete structure in nuclear power stations, Nuclear civil engineering series 5*, 2021 (in Japanese).

[5] Endo, T., Aoyagi, M. and Matsumura, T., "Estimation of shear strength for limit state design of underground reinforced concrete structures," *Central Research Institute of Electric Power Industry report*, 1992 (in Japanese).

[6] Railway Technical Research Institute, *Design Standard for Railway Structures and commentary* (*Foundation Structures*), Maruzen, 2012 (in Japanese).

[7] Railway technical research institute, *Design standards for railway structures and commentary (concrete structure) -verification example of RC rigid frame viaduct-*, 2005 (in Japanese).

[8] Shima, H., Chou, L. and Okamura, H., "Bond-slip-strain relationship of deformed bars embedded in massive concrete," *Journal of Japan Society of Civil Engineers*, Vol. 378/V-6, pp. 165-174, 1987 (in Japanese).

[9] Nakamura, H. and Higai, T., "Compressive fracture energy and fracture zone length of concrete, seminar on post-peak behavior of RC structures subjected to seismic loads," JCI-C51E, Vol. 2, pp. 259-272, 1999.

[10] Nakata, Y., Sakaguchi, J. and Watanabe, K., "Influence of Hysteresis of Axial Force and Ground Reaction Force on Shear Capacity of RC Piles," *Concrete Structure Scenarios, JSMS*, Vol. 24, pp. 357-362, 2024 (in Japanese).

[11] Tanimura, Y., Sato, T., Watanabe, T. and Matsuoka, S., "Shear Strength of Deep Beams with Stirrups," *Journal of Japan Society of Civil Engineers*, No. 760/V-63, pp. 29-44, 2004 (in Japanese).

[12] Tadokoro, T., Tanimura, Y. and Hattori, H., "Evaluation of Shear Strength of the Head of RC Piles," *RTRI Report*, Vol. 20, No. 5, pp. 23-28, 2006 (in Japanese).

Authors

Yuki NAKATA, Dr.Eng.
Senior Researcher, Concrete Structure Laboratory, Structures Technology Division
Research Areas: Concrete Structures

Ken WATANABE, Ph.D.
Senior Chief Researcher, Head of Concrete Structure Laboratory, Structures Technology Division
Research Areas: Concrete Structures

Haruyuki KITAGAWA
Researcher, Structural Mechanics Laboratory, Railway Dynamics Division
Research Areas: Bridge Mechanics, Vehicle Interaction

Toshiya TADOKORO, Dr.Eng.
Director, Head of Structures Technology Division
Research Areas: Concrete Structures

Effect of Snow Cover on Slope Stability of Embankment during Rainfall and Snowmelt

Tsuyoshi TAKAYANAGI **Shoma FUJIWARA**
Geo-hazard & Risk Mitigation Laboratory, Disaster Prevention Technology Division

Ryota SATO
Meteorological Disaster Prevention Laboratory, Disaster Prevention Technology Division

In this study, the effect of snow cover on slope stability was examined to more accurately evaluate the risk of snowmelt hazards. Firstly, laboratory tests were carried out to determine strength characteristics of snow. In addition to laboratory tests, sprinkling model experiments were conducted on a snow-covered embankment model to observe the moisture response and deformation of the embankment. In addition, slope stability analysis using a finite element method was carried out on the snow-covered embankment model. The result confirmed that snow cover could restrict the surface layer of an embankment and slightly improve the slope stability.

***Key words*:** *snowmelt, snow cover, slope failure, maintenance, slope stability*

1. Introduction

In snowy areas along railway lines in Hokkaido and on the Sea of Japan side of Honshu, there have been reports of cases of landslides triggered by the infiltration of melting snow, for example [1, 2]. In this paper "ground slope" is used to refer to embankment slopes, cut slopes and natural slopes; "snowmelt hazard" is defined as a landslide that occurs during the snow season due to the infiltration of melting snow or rain, and not due to external forces such as seismic activity. When a snowmelt hazards occurs, as shown in Fig. 1, there are many cases where snow cover remains on the slopes. In this study, slopes with residual snow cover are referred to as "snow-covered slopes." Snow is composed of ice grains and the soil is composed of minerals, and each of these objects has its own weight, permeability, strength and deformation characteristics. It is therefore assumed that the presence or absence of snow has some effect on the stability of the ground slope in relation to issues such as permeability and stress deformation.

2. Research Objective

The objective of this research is to verify the effects of snow on slope stability where snowmelt and rainfall act on snow-covered slopes. In this research, we focus on snow-covered slopes in case of embankments. To collect information on the characteristics of the snow for the above verification, we conducted a laboratory test using a constant-pressure direct box shear test with snow specimens. In addition, after we conducted sprinkling experiments on embankment models of snow-covered slopes to observe the behavior of the models in rain, we evaluated the stability of snow-covered slopes based on slope stability analysis.

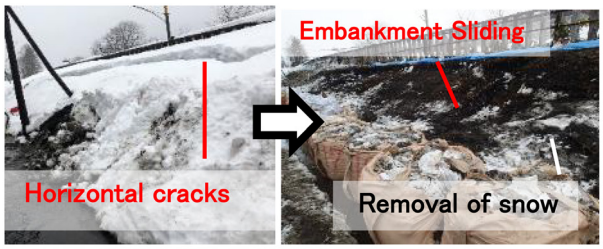

Fig. 1 Case of landslide on a slope with snow cover (embankment) [1]

3. Relationship between snow cover and shear strength of the ground [1]

In this chapter, we report on the results of constant-pressure direct box shear test [3] (Fig. 2 and Fig. 3) which was conducted with snow and sand specimens under various conditions using a field direct box shear test machine to obtain the strength parameters. The conditions of each test case are summarized in Table 1. The purpose of changing the condition of specimens is to understand the effects of conditions such as "water content," "snow particle size," "undisturbed or reconstructed," "shear rate," and "snow/ground boundary" on the strength parameters.

For the constant-pressure direct box shear test, a horizontal displacement meter and shear force meter were installed at the field direct box shear testing machine (Fig. 2). The test was conducted in a low-temperature chamber (room temperature was 2°C) with the aim of suppressing snow melting. The test machine has a rectangular shear box (cross-sectional area 100 mm × 100 mm, height 50 mm, upper box and lower box).

In preparation for the snow test specimens, outdoor snow accumulation was sampled at Shiozawa Snow Testing Station. Prior to sampling of snow specimens, the vertical excavation surface of the accumulated snow was observed. Small samples were taken at 10 cm interval depths from the snow surface to check the condition of the snow, including the wet density. In addition, the weight moisture content of the snow was measured with a dielectric moisture meter and the hardness PR [4] was measured using a push gauge at the same height at the vertical excavation surface of the snow. When collecting in-situ "undisturbed" snow specimens, the appropriate snow layer was selected based on the results of the above snow observations, and a shear box (cooled in advance in the snow) was pushed into the target snow layer to sample it. When using "reconstituted samples," disturbed snow material was removed from the snow layer and placed in the shear box, and the snow specimens were produced by compaction.

In the test to determine the shear strength of the "snow-ground

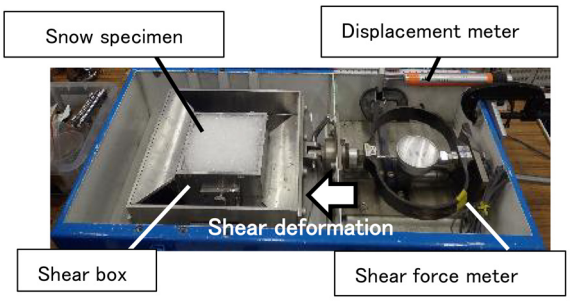

Fig. 2 Preparations for the constant-pressure direct box shear test

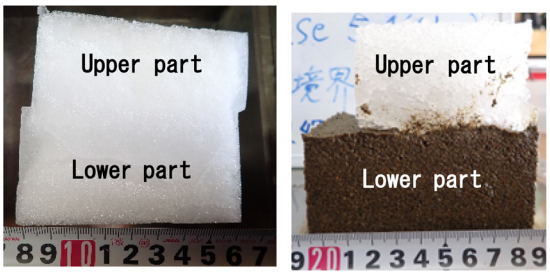

Fig. 3 Examples of test specimens after constant-pressure direct box shear test (Left: Test case S-1, Right: Test case SG-2)

interface," the ground was compacted in the lower shear box and then compacted snow specimens were placed in the upper shear box. Note that the name of ground material used in the test is *Inagi* sand.

The basic procedure for the constant-pressure direct box shear test is as follows. The snow specimen was placed in the testing machine and was saturated by filling the test box with cooling water for the saturation case. A loading plate was then placed on top of the specimen, and a weight was used to apply a vertical stress (three hypothetical stress conditions of snow accumulation with 2 m height: 0.6 kPa, 5.5 kPa, and 10.4 kPa) on the specimen at a constant pressure. For the shear test, the jack of the testing machine was manually operated at a constant speed to apply horizontal displacement to the shear box. The relationship between horizontal displacement D and shear stress τ was determined by shearing the specimen.

An example of the specimen after the test is shown in Fig. 3. Note that the shear stress was calculated by dividing the shear force T by the shear box cross-sectional area A. For the constant-pressure direct box shear test, the specimens were tested with the same snow condition for each of the three different normal stress patterns, and the relationship between normal stress and maximum shear stress was analyzed to determine the internal friction angle φ and cohesion c. The internal friction angle and cohesion for each test case are shown in Table 1.

Figure 4 shows the relationship between horizontal displacement and shear stress of the granular snow (case S-2) and *Inagi* sand (case G-1). The *Inagi* sand was a highly compacted test specimen, and the shear stress behavior shows a peak at a horizontal displacement of around 4 mm (around 4% horizontal strain). On the other hand, for the case of granular snow (case S-2), the shear stress increases gradually with horizontal displacement, even in the relatively large deformation region of approximately 10 mm horizontal displacement (10% horizontal strain). The cause of this is thought to be due to the sintering effect that occurs when the pressure between ice particles increases.

Figure 5 shows the relationship between the maximum shear stress and the normal stress. The legend in the figure corresponds to Table 1. To verify the effect of the water content of granular snow on the shear strength, three cases of S-2, S-3 and S-4 with different water contents are compared. In the case of S-4, a decrease in maximum shear stress is observed at low normal stress condition, but at other stress conditions, the maximum shear stress is almost the same in each case. From this, it can be concluded that the strength of granular snow, which is often observed during late season snowmelt, does not change significantly with the water content, except in saturated conditions and low stress conditions.

Next, we examined S-2, G-1, and SG-1 in order to compare the shear strength of unsaturated granular snow, *Inagi* sand, and the snow/ground interface. It is confirmed that snow (S-2) has a higher shear strength than sand (G-1). On the other hand, the shear strength of the snow/ground interface (SG-1) is the lowest. Therefore, in cases where there is no vegetation on the ground to increase the adhesion between the snow and the ground, the avalanche failure mode would be selected because the snow/ground interface has the lowest shear strength. On the other hand, in cases where the adhesion between the snow and the ground is high, the ground becomes the weakest, and it is assumed that the slope failure mode would be selected.

Next, we examine the shear rate dependence of snow cover strength by comparison of S-5 and S-6. Under the experimental conditions of the study, no clear velocity dependence is observed. In addition, the effect of snow type on shear strength is examined by comparing the internal friction angles and cohesion of S-1 and S-2 in Table 1, and it is confirmed that firmer snow had higher strength than granular snow in this study. This result confirms that changes in snow type are one of the main factors in changes in snow cover strength.

In terms of comparing undisturbed samples with reconstructed

Table 1 Conditions and test results for the constant-pressure direct box shear test

Case	Snow									Inagi sand			Test conditions			Results		Fig. 5
	Initial wet density ρ_{st} (g/cm³)	Initial dry density ρ_{sd} (g/cm³)	Initial weight moisture content θ_m (%)	Saturated weight moisture content θ_{msat} (%)	Maximum load settlement δ_{max} (mm)	Sample composition	Snow type	Particle diameter (mm)	Hardness PR (kPa)	Initial wet density ρ_t (g/cm³)	Initial dry density ρ_d (g/cm³)	Water content ratio w (%)	Specimen	Unsaturated or saturated	Shear rate vs (%/min)	Friction angle φ_d (°)	Cohesion c_d (kPa)	
S-1	0.536	0.471	12.1	—	2.8	Undisturbed	Compacted	0.2～0.5	109.4	—	—	—	Snow	Unsaturated	1.7	46.7	17.8	
S-2	0.463	0.394	14.9	—	8.3	Undisturbed	Granulated	1～2	26.2	—	—	—	Snow	Unsaturated	1.7	38.5	7.5	(a), (b)
S-3	0.563	0.394	30.0	—	8.3	Undisturbed	Granulated	1～2	—	—	—	—	Snow	Unsaturated	1.7	37.1	7.6	(b)
S-4	0.463	0.394	14.9	0.0	15.7	Undisturbed	Granulated	1～2	—	—	—	—	Snow	Saturated	1.7	50.7	4.5	(b)
S-5	0.511	0.444	13.2	—	7.8	Reconst	Granulated	2～5	13.9	—	—	—	Snow	Unsaturated	11.1	37.4	5.8	(c)
S-6	0.510	0.443	13.2	—	12.5	Reconst	Granulated	2～5	17.5	—	—	—	Snow	Unsaturated	1.7	25.2	5.5	(c)
S-7	0.510	0.443	13.2	0.0	9.6	Reconst	Granulated	2～5	—	—	—	—	Snow	Saturated	11.1	47.5	6.8	
S-8	0.510	0.443	13.2	0.0	12.0	Reconst	Granulated	2～5	—	—	—	—	Snow	Saturated	1.7	50.9	1.7	
SG-1	0.463	0.394	14.9	—	5.2	Undisturbed	Granulated	1～2	—	1.47	1.41	3.98	Snow & sand	Unsaturated	1.7	41.4	1.1	(a)
G-1	—	—	—	—	—	—	—	—	—	1.51	1.41	5.30	Sand	Unsaturated	1.7	38.3	4.3	(a)

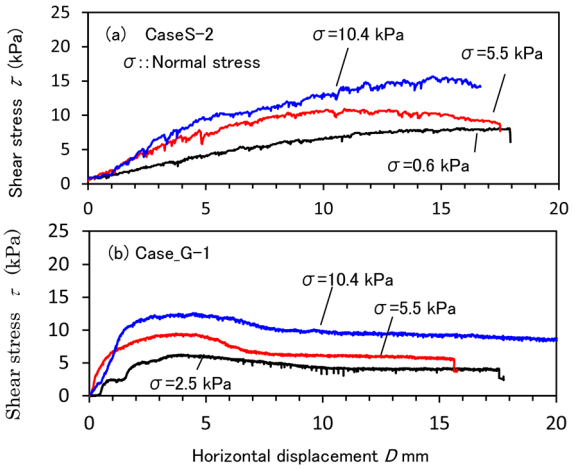

Fig. 4 Shear stress vs. horizontal displacement relationship

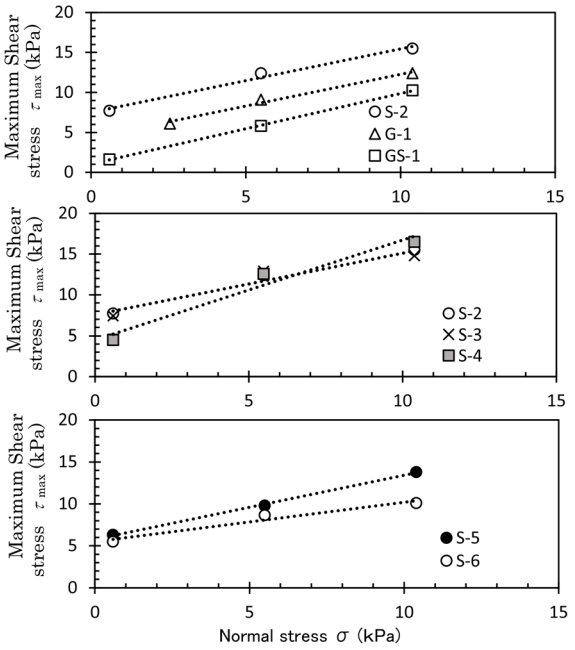

Fig. 5 Maximum shear stress vs. normal stress relationship

samples, the comparison of S-2 and S-6 shows that the reconstructed sample (S-6) has a slightly lower maximum shear stress. One reason for this is that the in-situ undisturbed sample has undergone consolidation between ice particles due to freezing. This is also confirmed from hardness PR (Table 1).

In this chapter, we have reported the results of the basic strength constants of the snowpack obtained from the constant-pressure direct box shear test. From these results, we have confirmed that even if the snow cover is granular snow, the maximum shear stress of snow is higher than that of *Inagi* sand.

4. Sprinkling model experiments on snow-covered slopes [1]

4.1 Overview

In this chapter, we report on the results of a sprinkling model experiment that simulated the conditions where a snow-covered slope on an embankment is subjected to rainfall, in order to understand the mechanism of snow-covered slope instability. We focus on the deformation of the snow-covered slope. In addition to this, we also report on the measured results of water behavior in the embankment during sprinkling.

4.2 Experimental Method

The geometric shape of the snow-covered slope model (experimental case with snow depth *Hs*=0.25 m) and the sensor installation location are shown in Fig. 6. The conditions for the experimental cases (snow, ground, and sprinkling conditions) are shown in Table 2. The main difference between each experimental case is the depth of snow cover on the embankment (*Hs*=0 m, 0.125 m, 0.25 m). In the sprinkling model experiment, the embankment was constructed twice in total. Case 1-1 was mainly conducted to observe the behavior of soil moisture during the sprinkling of the embankment without snow, and the sprinkling was stopped when deformation occurred at the toe of the slope. The damaged area of the embankment was repaired and reused to examine case 1-2. This case was used to examine the relationship between the occurrence of damage and the behavior of soil moisture in the embankment with snow cover. Case 2-1 was conducted with the aim of comparing it with case 1-1 (Fig.7). It was used to observe the behavior of soil moisture in the embankment with snow cover during water sprinkling. The embankment was then reused for case 2-2, which was to examine deformation and soil moisture behavior of the embankment without snow cover. In case 2-1, slope sprinkling was stopped before the embankment collapsed. In Case 2-3 however, sprinkling was continued to induce a clear collapse. However, due to the influence of the snow cover, no clear collapse occurred. Therefore, the snow cover was thinned, and the sprinkling experiment was repeated in Case 2-4.

The method for constructing the embankment is explained below. The physical properties of the embankment ground material, "*Inagi* sand," are shown in Table 3. This ground material was placed in a rigid soil tank after being adjusted with water, and the ground was built by evenly compacting it to a compaction ratio of 84%.

The ground was then shaped into an embankment with a height of 1 m and a slope gradient of 1:1.2. The slope gradient is steeper than the current design values for railway embankments (1:1.5, performance rank III, height less than 9 m) [5]. The strength characteristics of the *Inagi* sand embankment were obtained from a triaxial compression test (CD test), with an internal friction angle of φ_d = 35.0° and cohesion of c_d = 6.3 kPa. For the snow build-up method, snow material (granular snow: grain diameter 2-5 mm) collected outdoors at Shiozawa Snow Testing Station was spread over the embankment surface by free fall (average fall height approx. 0.5 m) through a 1 cm mesh sieve and shaped to the planned thickness. In the sprinkling model experiment, the snow-covered slope was continuously sprayed with water at a rate of 27 mm/h indoors (air temperature was 4-10°C), based on the assumption that it would rain during the snow-melting season. In order to reduce the melting of the snow due to the warmth of the water, the water was supplied through a simple rapid cooler to lower the water temperature to 4°C. The main items measured during the sprinkling model experiment were the pore water pressure, volumetric water content and water head measured by manometers at the bottom of the rigid box. Note that the pore water pressure was obtained as additional information, so the measurement results are not shown in this report. In addition, slope deformation was observed from photographs of the side of the

Table 2 Summary of conditions for the sprinkler experiment

Test case	Focused Phenomena	Snow conditions					Ground conditions							Sprinkling
		Snow depth H_s (m)	Initial wet density ρ_{st} (g/cm³)	Initial dry density ρ_{sd} (g/cm³)	Initial moisture content θ (%)	Saturated permeability k_{sat} (m/s)	Model preparation	Initial wet density ρ_t (g/cm³)	Initial dry density ρ_d (g/cm³)	Water content ratio w (%)	Initial moisture content θ (%)	Initial saturation Sr (%)	Saturated permeability k_{sat} (m/s)	Rainfall intensity r (mm/h)
Case1-1	Moisture	0	—	—	—	—	New	1.62	1.41	14.9	21.0	43.62	5.7×10-5	27
Case1-2	Deformation	0.25	0.51	0.445	6.5	1.99×10-3	Reuse	—	—	—	—	—	5.7×10-5	27
Case2-1	Moisture	0.25	0.42	0.371	4.9	1.99×10-3	New	1.66	1.43	16.4	23.5	49.45	3.9×10-5	27
Case2-2	Deformation	0	—	—	—	—	Reuse	—	—	—	—	—	3.9×10-5	27
Case2-3	Deformation	0.25	0.51	0.441	6.9	1.99×10-3	Reuse	—	—	—	—	—	3.9×10-5	27
Case2-4	Deformation	0.125	0.51	0.432	7.8	1.99×10-3	Reuse	—	—	—	—	—	3.9×10-5	27

Table 3 Physical properties of *Inagi* sand

Soil particle density ρ_s(g/cm³)	Average particle diameter D_{50}(mm)	Fine particle content F_c(%)	Maximum dry density ρ_{dmax}(g/cm³)	Optimum water content w_{opt}(%)
2.72	0.17	14.90	1.68	14.6

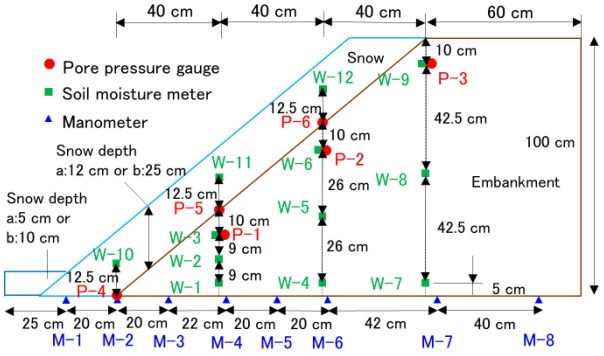

Fig. 6 Dimensions of the model experiment and sensor positions

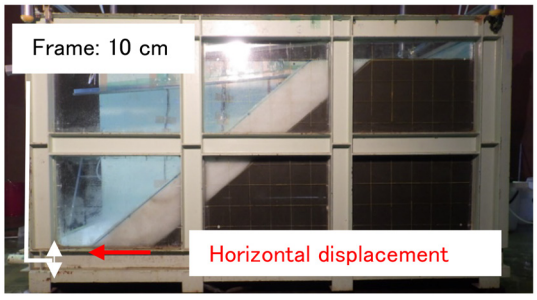

Fig. 7 Model construction (Case 2-1)

rigid box taken from fixed point.

4.3 Experimental results

Focusing on the infiltration phenomenon on a snow-covered slope, we report on the water behavior in case 2-1 with snow cover (snow depth = 0.25 m). Specifically, Fig. 8 shows the spatial distribution (contour map) of the volumetric water content and the water head distribution at four stages during the 342 minutes from the start of the sprinkling in case 2-1. To compare the results shown in Fig. 8, the results for case 1-1 with no snow cover from the start of sprinkling to 342 minutes are shown in Fig. 9. Comparing Fig. 8 (d) and Fig. 9, it can be seen that the presence or absence of snow cover had no significant effect on the water head of the manometer under the conditions of this experiment. On the other hand, it should be noted that there is a possibility that measurement errors occurred due to air bubbles in the manometer M-3 in Fig. 9, so this should be considered when interpreting results. As mentioned above, the effect of snow cover on the infiltration phenomenon in the embankment was limited under the conditions of this experiment. The reason for this is that the snow used in this experiment was coarse granular snow (grain diameter 2-5 mm) with high permeability, and the snow cover thickness was 0.25 m, which is not thick. On the other hand, in nature there are various types of snow with finer grain size and lower permeability, such as “compacted snow” (grain size of about 0.5 mm). Therefore, rainwater and snowmelt water can be expected to take a long time to infiltrate through the snow cover and reach the ground surface where such snow types are interspersed with layers of snow. In order to verify the overall impact of the combined effects of snow depth, snow type and snowmelt on the moisture behavior of the soil in the embankment, more detailed validation using seepage flow analysis modelling a snow-covered slope is required.

Next, we consider the deformation issue of a snow-covered slope. Figure 10 shows the relationship between the horizontal displacement of the embankment at a height of 10 cm from the bottom (Fig. 7) and the manometer’s water head. The horizontal displacement was obtained by analyzing the side photographs of the model experiment. The water head of M-4 and M-5 manometer is adopted as representative value at the toe of the embankment. From these results, it can be concluded that the horizontal displacement of the embankment caused by the increase in the water head of the manometer was suppressed by the effect of the snow cover in the case with snow cover compared to the case without snow cover.

In order to understand the differences in the deformation of snow-covered slopes with different snow depths, the changes of the slope of the embankment after water sprinkling in case 1-2 (snow depth = 0.25 m) and case 2-4 (snow depth = 0.125 m) are shown as examples in Fig. 11. In case 1-2 where the snow cover is relatively thick, the snow accumulation has a restraining effect on the surface which acts as a slope protection. As a result, although the snow cover was subjected to earth pressure due to shallow sliding at the toe of the embankment and volume changes occur at the rear of the snow cover, the displacement on the snow cover surface was small. On the other hand, in Case 2-4 where the snow cover was relatively thin, the entire snow cover slid, dragged by the sliding of the embankment surface. Figure 12 shows photographs of the deformation of the embankment observed after the water sprinkling. The effects of the snow cover on the deformation of the embankment were then considered using Fig. 10 and Fig. 11. In both case 1-1 and case 2-2, where there is no snow cover, horizontal cracks were observed at a

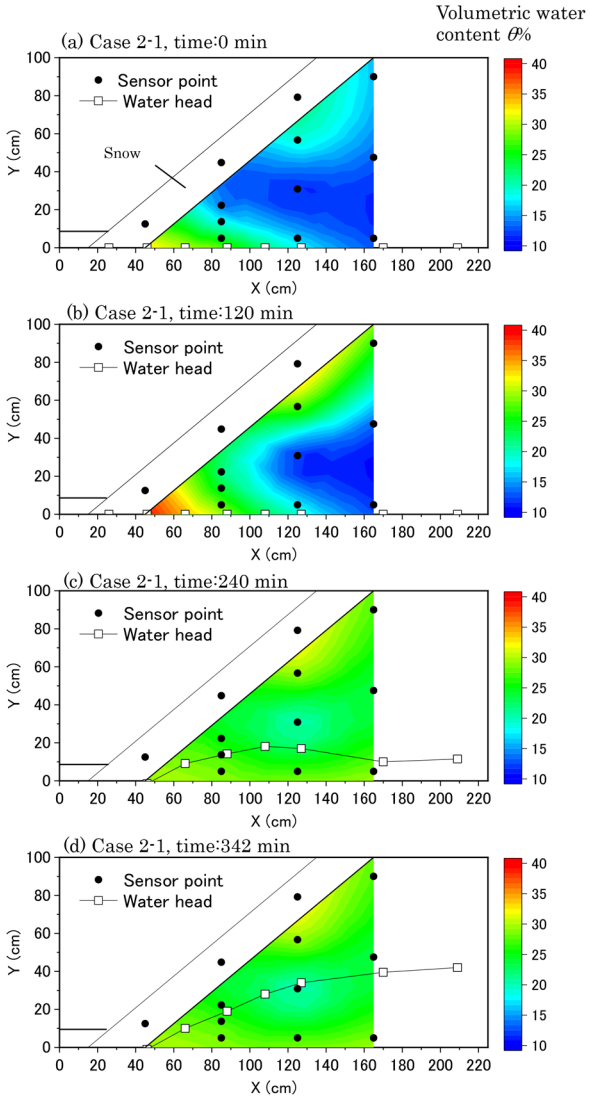

Fig. 8 Distribution of volumetric water content and water head (Case 2-1, from 0 to 342 minutes after the start of watering)

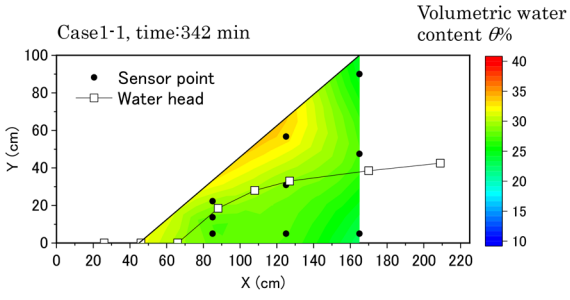

Fig. 9 Distribution of volumetric water content and water head (Case 1-1, 342 min after the start of watering)

slope length of 45 cm from the toe of the slope. These cracks were observed to be progressing at the time of their occurrence, and it was assessed that if the water sprinkling had not been stopped, the embankment would have slipped and collapsed. On the other hand, in cases 1-2 and 2-3, where the slope of the embankment was con-

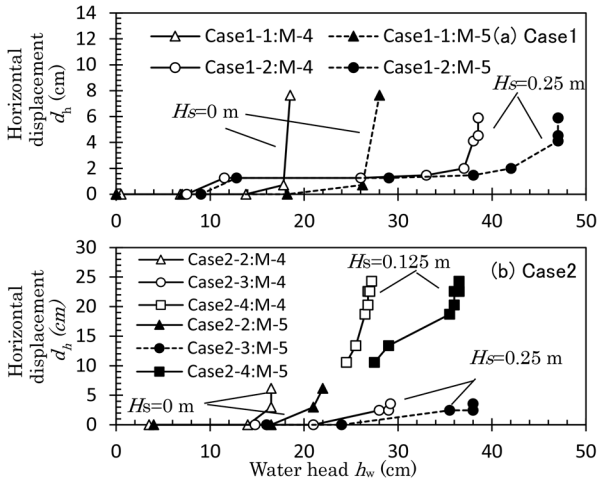

Fig. 10 Relationship between manometer's water head (M4, M5) and horizontal displacement amount : Horizontal displacement amount of the slope at a height of 10 cm

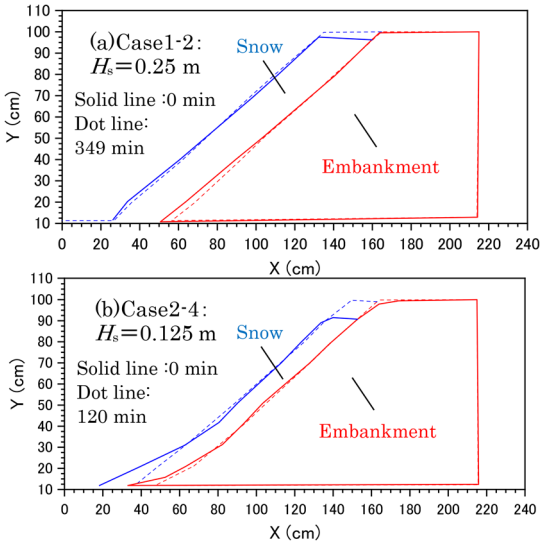

Fig. 11 Changes in the shape of the snow-covered embankment model (top: Case 1-2, bottom: Case 2-4)

strained by the thick snow cover, no clear progressive deformation was visually observed during the experiment, even under conditions with higher water heads of manometer than in cases without snow cover. However, in case 1-2, when the snow cover was removed after water sprinkling, a horizontal crack was observed as a deformation at a slope length of 35 cm from the slope shoulder. We consider the possibility that the shallow deformation on the embankment did not progress because of the restraining effect of the snow cover, and that the granular snow has a higher cohesion c than the *Inagi* sand, which increases the apparent cohesion across the snow-covered slope, in case 1-2. Therefore, a deeper arc-slip mode would be selected in the embankment.

In case 2-4, where the snow cover was thin, the toe of the slope showed progressive deformation, the snow cover became extremely thin around areas of melting snow (the middle of the slope) and the eroded soil flowed down from the area, but there was no clear slip failure as shown in Fig. 1. These results indicate that snow cover has

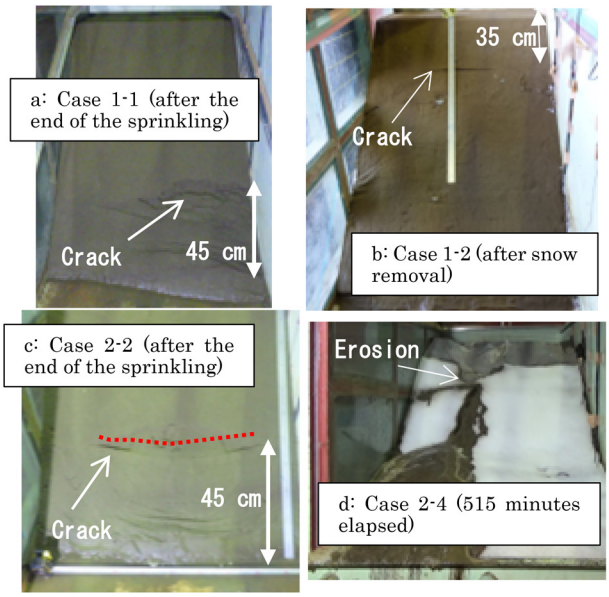

Fig. 12 Summary of slope deformation (Case 1-1, Case 1-2, Case 2-2, Case 2-4, front view)

the effect of restraining the movement of small slides and muddy sediments on the slope surface of the embankment.

5. Sprinkling model experiments on snow-covered slopes [1]

In this chapter, we report on the results of a verification of the stability of snow-covered slopes. Note that the result was obtained by performing stress deformation analysis and slope stability analysis using the finite element method analysis software "PLAXIS 2D."

The geometric shape of the analysis model, the material conditions and the boundary conditions were based on the model experiment in chapter 4, and the other conditions are shown in Fig. 13. In addition, Table 4 shows the analysis parameters for the snow-covered slope obtained from the laboratory tests, and Table 5 shows the conditions for the slope stability analysis. In the slope stability analysis, the conditions are basically the same as in the water sprinkling experiment in Chapter 4. When the cohesion c of the embankment material *Inagi* sand (the internal friction angle φ and other parameters are fixed) and the groundwater level in the embankment (the water head h_w at the M-4 location is used as the benchmark for the groundwater level in the embankment) are changed, the slope deformation mode and the slope safety factor Fs above conditions are confirmed.

The specific analysis procedure is described below. Since "PLAXIS 2D" can combine stress-deformation analysis and saturated-unsaturated seepage flow analysis, a steady seepage flow analysis was first performed for the entire embankment under rainfall. The rainfall conditions were varied by trial-and-error to reproduce the hydrostatic pressure distribution in the embankment that reproduces the water head h_w (4 profiles) of M-4 in Table 5.

The information on the four hydrostatic pressure distribution profiles obtained in this way were used in the stress deformation analysis, and the stresses of the embankment under the conditions of the above steady pore water pressure distribution were calculated. The slope safety factor Fs is evaluated using the shear stress reduction method based on the above stresses and hydrostatic pressure distribution. Note that if the calculation does not converge and

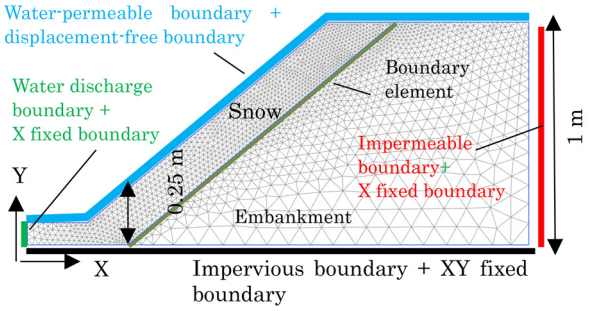

Fig. 13 Element and boundary conditions for slope stability analysis

Table 4 Summary of Analysis Parameters

Material type			Inagi sand	Compacted snow	Granulated snow	Snow/Sand boundary
Material model			Mohr-Coulomb			
Drainage model			Drainage (without excess pore pressure)			
Wet unit weight	γ_{unsat}	kN/m^3	16.2	4.2	4.2	4.2
Saturated unit weight	γ_{sat}	kN/m^3	18.9	9.7	9.7	9.7
Elastic coefficient	E	kN/m^2	6166	400	400	400
Poisson's ratio	ν		0.35	0.1	0.1	0.1
Shear rigidity	G	kN/m^2	2284	181.8	181.8	181.8
Dilatancy angle	ψ	°	5.0	0	0	0
Cohesion	c	kN/m^2	0～6	17.8	9.1	1.6
Tensile strength	c_t	kN/m^2	0	0	0	0
Friction angle	φ	°	35.0	46.7	46.3	47.0
Water retention model			van Genuheten			
Residual saturation	S_{res}		0.062	0.068	0.049	0.049
Submerged saturation	S_{sat}		1.0	0.9	0.9	0.9
Model coefficient	g_n		1.38	3.17	3.99	3.99
Model coefficient	g_a	1/m	3.83	10.8	37.6	37.6
Model coefficient	g_c		-0.420	-0.684	-0.749	-0.749
Model coefficient	g_l		1.25	0	0	0
Saturated permeability	k_{sat}	m/s	3.90×10^{-5}	1.00×10^{-3}	1.99×10^{-3}	1.99×10^{-3}

Table 5 Summary of Slope Stability Analysis Conditions

Analysis	Snow	Embankment	Water M-4 (Fig. 6)
A	Without	*Inagi* (Table 4), c=0～6 kPa	h_w=0 m, 0.18 m, 0.24 m, 0.27 m
B	Granulated (Table. 4)	*Inagi* (Table 4), c=0～6 kPa	h_w=0 m, 0.18 m, 0.24 m, 0.27 m

reaches a final state in the stress deformation analysis stage, the slope stability analysis using the shear stress reduction method will not be performed. In addition, we use the snow strength parameter of granular snow in these cases. Although the cohesion of *Inagi* sand in the triaxial compression test (CD test) was c=6.3 kPa, the slope safety factor did not fall below 1.0 under the hydrostatic pressure conditions under which cracks occurred at the toe of the embankment in the model experiments. On the other hand, the safety factor Fs falls below 1.0 when cohesion = 0.2 kPa. One of the reasons for this discrepancy is that the confining pressure conditions for the triaxial compression test of *Inagi* sand were carried out at 5 kPa to 20

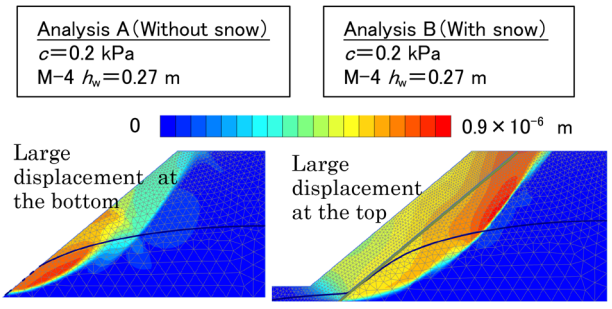

Fig. 14 Comparison of the distribution of the absolute value of the incremental displacement (with water level in embankment)

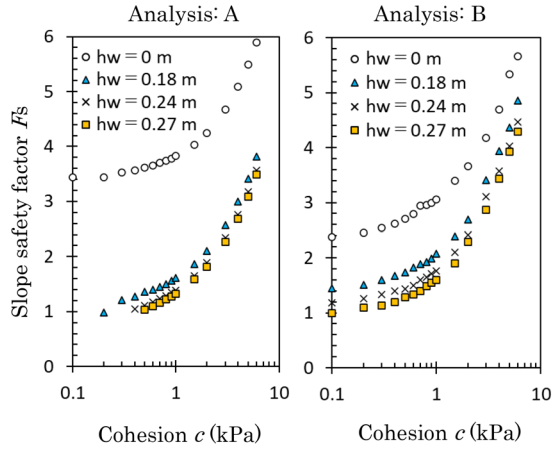

Fig. 15 Relationship between slope safety factor obtained from shear strength reduction method, cohesion of model embankment, and water head at manometer M4 position

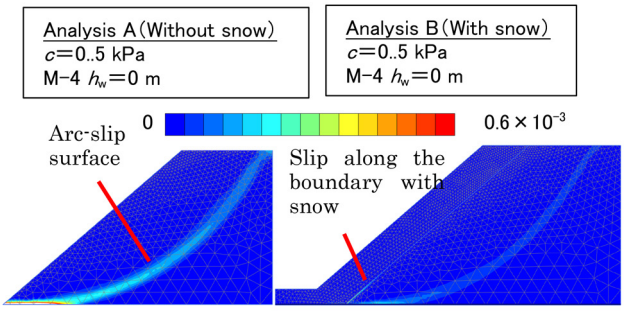

Fig. 16 Distribution of strain increment (no water level in embankment)

kPa. On the other hand, the confining pressure at the surface of the small embankment model was lower, so it is assumed that the cohesion was actually lower on the embankment surface. Assuming that the actual cohesion of *Inagi* sand is 0.2 kPa, Fig. 14 shows the collapse modes of the ultimate state under the conditions of stability analysis A (without snow cover, water head at M-4 = 0.27 m) and stability analysis B (with snow cover, water head at M-4 = 0.27 m) based on an incremental displacement. The former shows the state that was reached the ultimate state as a result of the preliminary stress deformation analysis, and the latter shows the state that reached the ultimate state as a result of the shear strength reduction method. The deformation mode of stability analysis A (without snow cover) is similar to that observed in the sprinkling model experiment case 1-1 in chapter 5 (Fig. 12), with relatively large displacements occurring at the toe of the embankment. On the other hand, in stability analysis B (with snow cover), relatively large displacements occur in the area around the embankment shoulder. This deformation mode is consistent with the deformation tendency observed after the sprinkling model experiment case 1-2, when the snow was removed (Fig. 12).

Here, the results of the parameter study of the slope safety factor based on the conditions in Table 5 are shown in Fig. 15. These results confirm that the slope safety factor *F*s in the stability analysis B (with snow cover) is higher than in the stability analysis A under the conditions where the water level in the embankment was formed by water sprinkling (water heads h_w at M-4 =0.18 m, 0.24 m, and 0.27 m). This is because the snow cover restrains the shallow collapse of the toe of the embankment, as can be seen from the difference in deformation modes in Fig. 14. From these results, it is thought that the slope safety factor of snow-covered slope is higher than the slope without snow cover. On the other hand, as a peculiar phenomenon, the slope safety factor of the snow-covered slope was found to decrease under the condition where the groundwater level in the embankment was not formed (water head at M-4 = 0 m). In order to confirm the cause, Fig. 16 shows the distribution of incremental strain as the ultimate state after analysis using the shear strength reduction method under the condition that the water level in the embankment was not formed (water head at M-4 = 0 m). Here, in stability analysis B (with snow cover), a region of major shear strain increments $\Delta\gamma$ is observed along the boundary between the snow cover and the embankment. In other words, under the condition where the groundwater level is not formed in the embankment in stability analysis B (with snow cover), it is assumed that the slip at the boundary between the snow cover and the ground was selected as the weakest failure mode. This can be called the all-layer avalanche mode.

In this study, we examined slope stability of snow-covered slope, and the results showed that snow generally has a positive effect on the stability of embankment slope, excluding the effects of snowmelt. However, depending on the slope gradient and ground surface conditions on natural slopes, for example, under conditions where snow accumulates thickly on the slope shoulders and snow loads are applied, it is assumed that snow accumulation may have a negative effect on the slope stability of snow-covered slopes. In the future, we would like to verify the stability of snow-covered slopes under various conditions.

6. Summary

In this study, we examined the effects of snow on slope stability from the perspective of evaluating the risk of snowmelt hazards caused by melting snow and rain in snowy regions. Specifically, the strength characteristics of snow were determined by laboratory test, and then a sprinkling model experiment was conducted on a 1m-high embankment model with snow cover, and the moisture response and deformation of the embankment were observed. Furthermore, slope stability analysis (shear stress reduction method) using the finite element method was carried out on this embankment model with snow. As a result, the following findings were obtained.

It was confirmed that the shear strength of the "granular snow" used in the experiment was higher than that of "*Inagi* sand" (sand ground) with a compaction degree of 84%. Note that while a peak in shear stress for the *Inagi* sand appeared at a horizontal strain of

around 4%, that for the granular snow often appeared at a horizontal strain of 10% or more and in some cases no clear peak appeared. The reason for this is assumed to be caused by the sintering process that occurs when the pressure between ice particles increases as snow accumulates.

The result of a water sprinkling experiment on a model embankment with snow cover confirmed that in the case of a snow cover built on an embankment, the deformation around the toe of the embankment caused by the water sprinkling was suppressed compared to the case without snow cover.

The slope safety factor of the snow-covered slope (embankment) model was obtained using slope stability analysis (shear strength reduction method), which uses the strength, deformation and physical properties of the granular snow obtained in this study. As a result, it was found that although the melting water increases the water content of the embankment, the snow itself may slightly improve the slope safety factor of the embankment in the case of a snow-covered slope (embankment) affected by rain and melting snow.

The evaluation reported in this paper was carried out using a small embankment model, and we subsequently plan to apply the results of this research to evaluate the stability of various snow-covered slopes in their natural state.

References

[1] Takayanagi, T., Manome, R., Fujiwara, S., Sato, R. and Naito, N., "Verification of the Effect of Snow Accumulation on Embankment Stability," *JSCE Journal*, Vol. 80, No. 4, 2024 (in Japanese).

[2] Japan Transport Safety Board, "Derailment of a train between Myoko Kogen Station and Sekiyama Station on the Shinetsu Line of East Japan Railway Company," *Report on Railway Accident Investigation*, Report No. RA2014-3-1, 2014 (in Japanese).

[3] Japanese Geotechnical Society, *Japanese Geotechnical Society Standards*, Laboratory Testing Standards of Geomaterials - Volume 2 of 2, Maruzen, pp. 705-709, 2020.

[4] The Japanese Society of Snow and Ice, *Handbook of Snow Observation*, Asakura Publishing Co., pp. 44-45, 2010 (in Japanese).

[5] Railway Technical Research Institute, *Design Standards for Railway Structures, Railway Earth Structures*, Maruzen, 2007 (in Japanese).

Authors

Tsuyoshi TAKAYANAGI
Senior Researcher, Geo-hazard & Risk Mitigation Laboratory, Disaster Prevention Technology Division
Research Areas: Geotechnology, Slope Stability Assessment, Snowmelt Hazard.

Shoma FUJIWARA
Researcher, Geo-hazard & Risk Mitigation Laboratory, Disaster Prevention Technology Division
Research Areas: Geotechnology, Slope Stability Assessment.

Ryota SATO
Assistant Senior Researcher, Meteorological Disaster Prevention Laboratory, Disaster Prevention Technology Division
Research Areas: Glaciology

Practical Method for Setting Nonlinear Response Spectrum for Seismic Design of Railway Bridges and Viaducts

Kimitoshi SAKAI
Structural Dynamics and Response Control Laboratory, Center for Railway Earthquake Engineering Research

A Non-linear Response Spectrum Method is one of the methods used to calculate the seismic response values of railway bridges and viaducts. In this study, a method for expressing the non-linear response spectrum is proposed using a relatively simple mathematical equation. In addition, a procedure for estimating the parameters for the equation is proposed. The proposed method was applied to seismic records, and results confirmed that the proposed method can automatically represent the overall trend of the spectra of seismic records while significantly reducing the number of parameters used compared to conventional methods.

Key words: *yield seismic coefficient demand spectrum, seismic design, earthquake motion prediction equation*

1. Introduction

The design earthquake motion used in the seismic design of railway structures is represented by an elastic acceleration response spectrum and time history waveforms [1]. However, in design practice, the calculation of earthquake response values for general railway bridges or viaducts subjected to an Level2 earthquake typically uses a method that utilizes a nonlinear response spectrum. For this purpose, a "required yielding seismic coefficient spectrum" is prepared corresponding to each ground and structural condition. The use of this spectrum allows designers to calculate the nonlinear response of structures with greater accuracy than other approximate seismic response calculation methods, such as those based on energy conservation or displacement conservation properties. Moreover, since nonlinear dynamic analysis is not required, it serves as an effective and practical method for calculating structural response values during seismic design [2].

The required yielding seismic coefficient spectrum can be calculated relatively easily by repeating a nonlinear dynamic analysis using the time history waveform of the input earthquake motion. However, in the seismic design of railway structures, the calculation results (e.g., the orange line in Fig. 1) are not used as they are, but are displayed as a combination of several straight lines, as shown by the blue lines in Fig. 1. This approach is used to avoid drastic changes in the yielding seismic coefficient required for a structure due to slight change of its natural period. It also ensures ease of handling during the design process.

Setting this linearized procedure involves defining several straight lines for each response ductility factor. For instance, as shown in Fig. 1, a total of 37 control points (corresponding to 74 values of the equivalent natural period T_{eq} and the required yielding seismic coefficient k_{hy}) are defined manually within the range of response ductility factor μ=1–10. These control points are selected to replicate the calculated results as closely as possible. However, as there are no quantitative judgment criteria, this process may include empirical decision of the individual performing the task. Furthermore, the determination of the bedrock earthquake motion requires yielding seismic coefficient spectrum for each ground condition and structure type. However, preparing the spectra used in the design is time and labor intensive. Furthermore, recent years have seen an increase in situations where the design earthquake motion at the bedrock is evaluated on a case-by-case basis considering local construction site conditions [3]. In such cases, visual linearization of the spectrum is time and labor intensive. Developing a method to automatically determine the required yielding seismic coefficient spectrum for a given earthquake motion using a predefined equation could significantly reduce the time and labor required in design practice and minimize worker-induced variations in results.

This study presents a method to automatically and rationally determine the required yielding seismic coefficient spectrum for design [4].

2. Examination of the automatic setting method of yield seismic coefficient demand spectrum

2.1 Examination of the display method

The required yield seismic coefficient spectrum is represented by connecting the set of T_{eq} and k_{hy} of structures that give the same response ductility factor μ (maximum response displacement δ_{max}/yield displacement δ_y). Since the required yield seismic intensity spectrum is often calculated and displayed in increments of 1 across the range μ 1–10, this display method is also adopted in this study.

Previous research has shown that the shape of the undamped

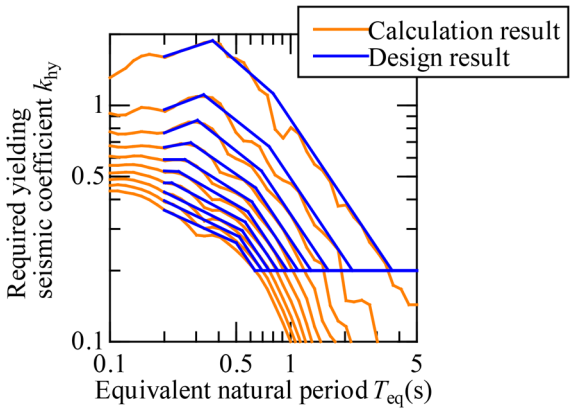

Fig. 1 Example of yield seismic coefficient demand spectrum (Response ductility factor μ =1–10)

velocity response spectrum closely resembles the Fourier amplitude spectrum of earthquake motion [5]. The response spectrum can be easily and approximately converted by multiplying or dividing the natural circular frequency ω by the acceleration, velocity, or displacement. Therefore, the use of a mathematical representation of the Fourier amplitude spectrum is considered an effective approach. The relationship between periods can be determined using a method that represents the Fourier amplitude spectrum based on the superposition of hypocenter, propagation path, and site characteristics. Using this approach, it is expected that the mathematical expression of the required yield seismic coefficient spectrum for the first earthquake motion wave can be easily determined. For instance, the Fourier amplitude spectrum $A(f)$ at the bedrock position, assuming a point hypocenter, can be calculated as follows:

$$A(f)=\frac{R_{\theta\phi}\cdot FS\cdot PRTITN}{4\pi\rho V_s^3}\times M_0 \times\frac{(2\pi f)^2}{1+(f/f_c)^2}\times\frac{\exp(-\pi fR/Q_s V_s)}{R} \quad (1)$$

where M_0, $R_{\theta\phi}$, FS, $PRTITN$, ρ, V_s, f_c, R, and Q_s represent the seismic moment, radiation pattern coefficient, amplification due to the effect of the free surface, coefficient representing the dispersion of energy into two horizontal components, soil density, soil shear wave velocity, corner frequency, distance from the hypocenter (km), and Q value in the propagation path, respectively. In this representation, terms related to distance attenuation are omitted, and the terms preceding M_0 are consolidated into a constant α. The exponent components governing the gradients on the long-period and short-period sides of the spectrum are denoted as variables β and γ, respectively, to simplify the expression. Accordingly, Eq. (1) can be reduced to:

$$A(f)=\alpha\cdot\frac{(2\pi f)^\gamma}{1+(f/f_c)^\beta} \quad (2)$$

This allows us to control the shape of the spectrum only by the parameters α, β, γ, and f_c, while preserving the physical background of the earthquake motion amplitude spectrum. If the procedure for automatically identifying these four parameters is systematically organized and if the required yield seismic coefficient spectrum of the design earthquake motion at the relevant point is accurately reproduced using Eq. (2), the design spectrum can be displayed with significantly less effort and fewer indices than previous methods. This approach is expected to greatly improve the convenience of design practice.

Figure 2 shows the change in the spectrum shape when each parameter is changed for $A(f)$ calculated using Eq. (2). The basic values $\alpha = 0.01$, $\beta = 2.0$, $\gamma = 2.0$, and $f_c = 2.0$ were used as a reference. The results presented in Fig. 2 show that the overall shape of the spectrum closely resembles the yield seismic coefficient demand spectrum shown in Fig. 1. Consequently, modifying the four parameters provides a relatively high degree of flexibility in spectrum representation. Eq. (2) facilitates easy control of the gradients on the short-period and long-period sides of the spectrum for each earthquake motion by evaluating the square of the exponents in Eq. (1) using the parameters β and γ. This approach allows the convenient and appropriate configuration of the yield seismic coefficient demand spectrum for design earthquake motion waveform, which may have various frequency characteristics.

Accordingly, we propose to present the required yield seismic coefficient spectrum for earthquake motion using Eq. (3). This equation is modified for better comprehension by railway structure designers based on Eq. (2). This modification expresses the spectrum in terms of the period, (T_{eq}) and yield seismic coefficient demand (k_{hy}) instead of frequency.

$$k_{hy}(\mu, T_{eq})=\alpha\cdot\frac{(2\pi/T_{eq})^\gamma}{1+(T_c/T_{eq})^\beta} \quad (3)$$

where T_{eq}, T_c, k_{hy} (μ, T_{eq}), and α, β, γ, and T_c represent the equivalent natural period (s) of the structure, corner period (s), yield seismic coefficient (yield seismic coefficient demand spectrum) that causes the structure with equivalent natural period T_{eq} (s) to respond with μ for the target earthquake motion, and regression coefficients that vary with μ of the structure, respectively.

2.2 Examination of parameter regression method

The parameter regression procedure for Eq. (3) is summarized in this section. All parameters for each earthquake motion and response ductility factor can be identified using the nonlinear least squares method. The lack of physical interpretation of the final parameters, however, makes further expansion to earthquake motion prediction equations difficult. Therefore, we consider the general shape of the yield seismic coefficient demand spectrum shown in Figs. 1 and 3 and estimate each parameter using the following procedure. Figure 3 shows the parameter estimation procedure and diagram.

Step1: Coefficient γ is calculated by the least squares method based on the gradient of the long-period component of the yield seismic coefficient demand spectrum. This γ does not depend on the response ductility factor μ and is common to all μ values.

Step2: With the parameter (γ) obtained in step 1 fixed, the coefficient α is calculated by the least squares method using the value of the short-period component of the yield seismic coefficient demand spectrum. The α is calculated for each response ductility factor μ (10 values are identified individually for μ = 1–10).

Step3: The coefficient T_c(f_c), is calculated from the intersection of the two lines obtained in steps 1 and 2. This parameter is also calculated for each μ (10 values are determined individually for μ = 1–10).

Step4: Once the parameters γ, α, and T_c are given, the coefficient β is calculated by the least squares method to fit the yield seismic coefficient demand spectrum. This β is also calculated for each μ (10 values are determined individually for μ = 1–10).

The ranges set for the long-period and short-period components in steps 1 and 2 are comprehensively determined for each earthquake record. These ranges were determined so that the sum of error squares of the required yield seismic coefficient spectrum is minimized. In addition, in Step1, coefficient γ is calculated from the gradient of the long-period component. As shown in Fig. 2, among the four parameters used in this examination, only γ contributes significantly to the long-period component. Changing the value of γ can change the shape of the entire spectrum, including the short-period side, depending on the period. Given γ, coefficient α, which primarily governs the overall shape, is set next, followed by coefficients T_c (f_c) and β in sequence, with the expectation that this order will result in stable coefficients. Additionally, by examining the yield seismic coefficient demand spectrum for various observation records, we confirmed that β, which determines the spectral shape of the short-period component, varies for each μ. Therefore, β is identified individually for each μ in this examination.

This procedure is expected to provide relatively stable parameter identification, even for yielding seismic coefficient demand spectrum with varying shapes due to seismic waves. Moreover, the

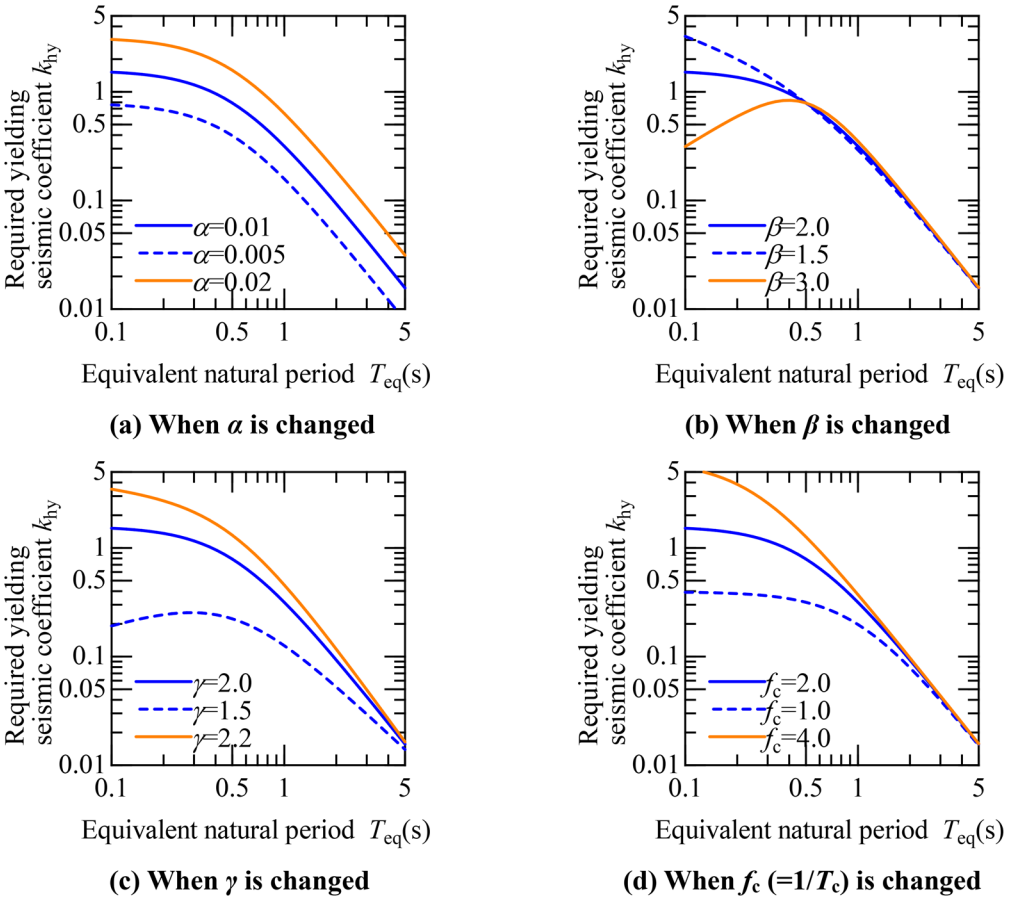

(a) When α is changed **(b) When β is changed**

(c) When γ is changed **(d) When f_c (=1/T_c) is changed**

Fig. 2 Changes in spectrum characteristics accompanying parameter changes (α = 0.01, β = 2.0, γ = 2.0, and fc = 2.0 as basis)

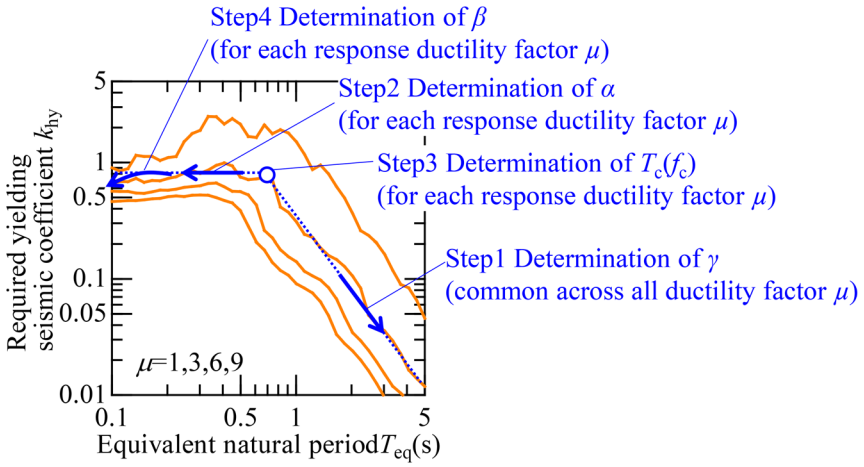

Fig. 3 Procedure for parameter regression of yield seismic coefficient demand spectrum

number of coefficients can be kept relatively small—e.g., 31 (γ: 1, α, T_c, β: 10 each), when μ ranges from 1 to 10. Expanding the display format of each parameter and identifying parameters for various earthquake records can further facilitate the development of a distance attenuation equation for the yield seismic coefficient demand spectrum, based on earthquake scale and distance.

3. Confirmation of the effectiveness of the proposed method

3.1 Target earthquake motion and calculation conditions

The effectiveness of the proposed method was confirmed by applying the mathematical expression of the yield seismic coefficient demand spectrum and the parameter regression method to actual earthquake motions. Figures 4 and 5 show the earthquake mo-

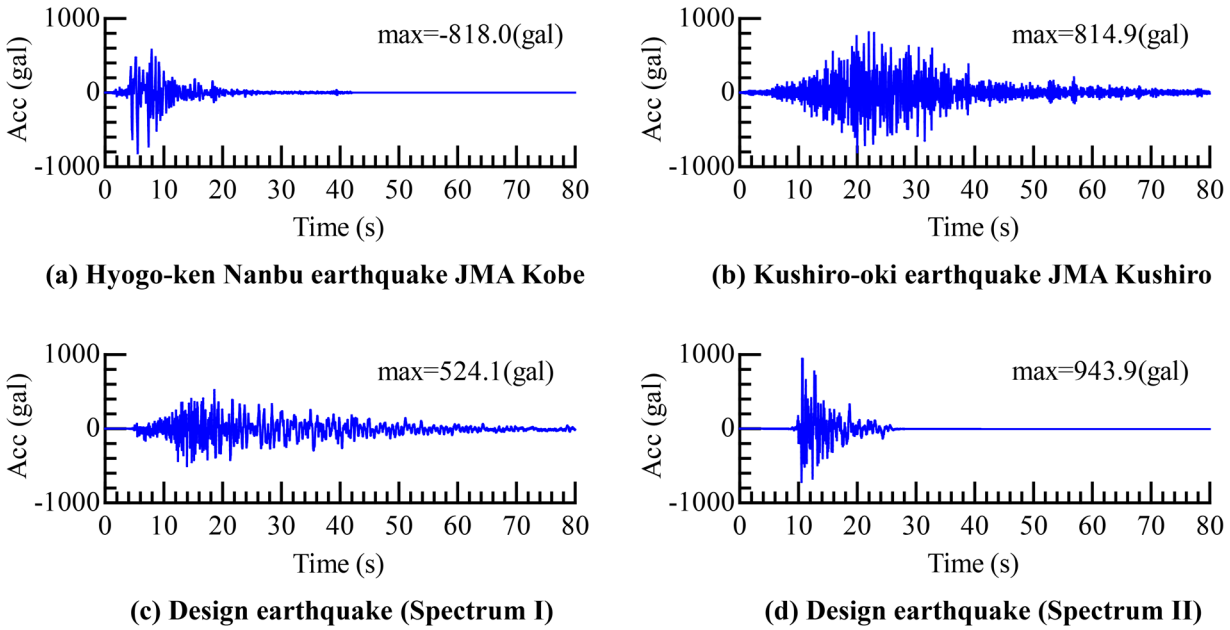

(a) Hyogo-ken Nanbu earthquake JMA Kobe

(b) Kushiro-oki earthquake JMA Kushiro

(c) Design earthquake (Spectrum I)

(d) Design earthquake (Spectrum II)

Fig. 4 Time history waveform of earthquake motion used for examination

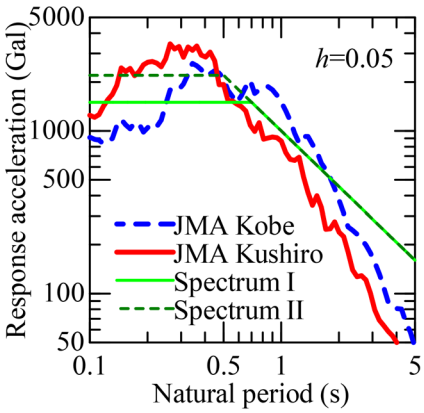

Fig. 5 Elastic response spectrum of earthquake motion used for examination

tion waveforms and the linear acceleration response spectrum used in this examination. The 1995 Hyogo-ken Nanbu earthquake (NS component) observed at JMA Kobe ("JMA Kobe"), the 1993 Kushiro-oki earthquake (NS component) observed at JMA Kushiro ("JMA Kushiro"), and the standard L2 earthquake motion spectrum I and II (G1 ground) time history waveform which are used in the seismic design of railway structures, were used as representative earthquakes. This standard L2 earthquake motion represents a time history waveform that statistically matches the linear acceleration response spectrum derived from past observation records, while exhibiting phase characteristics that result in relatively large yield seismic coefficient demand spectra for evaluating structural safety in seismic design.

The yield seismic coefficient demand spectrum was calculated for these earthquake motion waveforms. The target structure and calculation conditions were the same as those used in the calculation of required yield seismic coefficient spectrum for reinforced concrete bridges and viaducts. The nonlinear characteristics of the structure were modeled by a bilinear skeleton curve with a Clough hysteretic model. The second gradient ratio and the stiffness degradation index at unloading were selected as 0.1 and 0.2, respectively. The yield seismic coefficient (k_{hy}) of the structure with μ = 1–10 (in increments of 1) was obtained through convergent calculations. The equivalent natural period (T_{eq}) of the structure was set at 40 equal intervals on a logarithmic axis within the range of 0.1–5 s. The structural damping constant (h) was set to a constant value of 0.05, irrespective of the natural period.

Figure 6 shows the calculation result of the yield seismic coefficient demand spectrum (orange line) for each seismic wave shape (only μ = 1, 3, 6, 9) on the basic of the aforementioned conditions. As shown in Fig. 3, the rough shape of the yield seismic coefficient demand spectrum for each μ. is that k_{hy} becomes large at a certain natural period, and otherwise k_{hy} decreases gradually, with the downward slope on the long-period side being similar regardless of μ. In addition, the overall magnitude of the yield seismic coefficient demand, the period showing the peak, and the downward slope are different depending on the seismic wave shape used. Therefore, spectrum fitting needs to be carried out with some degree of freedom.

3.2 Spectrum fitting results

The proposed method was applied to the yield seismic coefficient demand spectrum of the four seismic wave shapes described above (orange line in Fig. 6). Meanwhile, the parameters γ, α, T_c, and β were identified using the procedure summarized in this examination. During parameter identification, we did not set any constraints or ranges for most of parameters. For parameter β, which controls the gradient of the spectrum on the short-period side, the final estimation results varied considerably for each seismic wave, and the shape and fit of the yield seismic coefficient demand spectrum did not change or improve considerably even when extremely large or small values were set. Therefore, we set a constraint in the range of $1.0 \leq \beta \leq 5.0$.

The above conditions were used to fit the yield seismic coefficient demand spectrum for each earthquake motion. The blue line in Fig. 6 shows the final yield seismic coefficient demand spectrum. These results indicate that the proposed formulation and fitting pro-

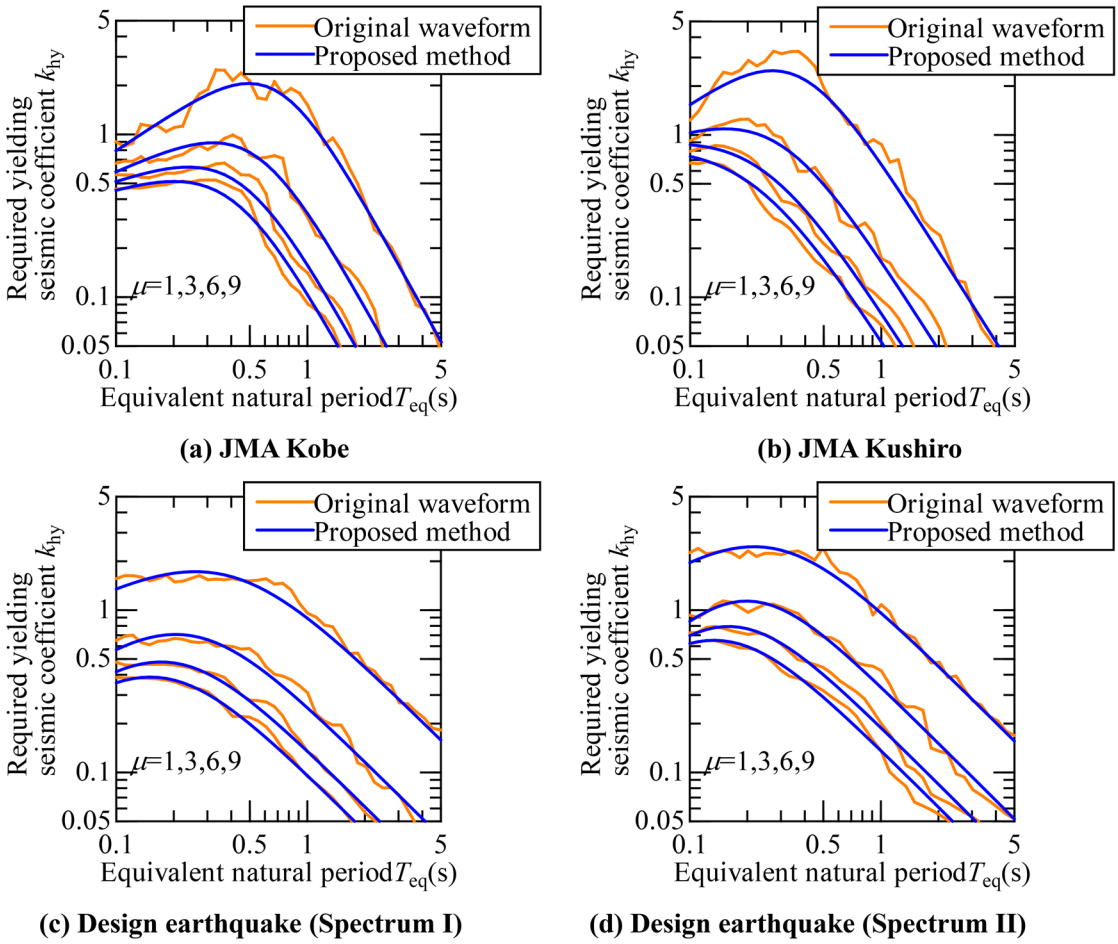

(a) JMA Kobe **(b) JMA Kushiro**

(c) Design earthquake (Spectrum I) **(d) Design earthquake (Spectrum II)**

Fig. 6 Required yielding seismic coefficient spectrum fitting results

cedure can adequately reproduce the characteristics of the yield seismic coefficient demand spectrum for any earthquake motion and μ. The spectrum obtained by this method has a result in which the spectrum for each period seen in the original waveform is smoothed and appropriately reflects the intention of the spectrum linearization conducted with the seismic design described in Section 1. In this examination, we seek parameters that reproduce the spectrum of a wide range of response ductility factors and equivalent natural periods on average, and therefore, there are some conditions where the yield seismic coefficient demand is slightly smaller than that of the original waveform, e.g., with JMA Kushiro, T_{eq} = 0.4 s and μ = 1 (Fig. 6(b)). This problem can be avoided by setting constraints such as including the results of the original waveform or exceeding them by a certain percentage, which takes into account how the original waveform will be handled during design.

Figure 7 shows the regression coefficients calculated for each earthquake motion. This figure shows that there is a gradual decrease in the index γ, which presents the degree of the gradient on the long-period side in the order of JMA Kobe, JMA Kushiro, and standard L2 earthquake motion (spectrum I, spectrum II), with almost equivalent values obtained for spectrum I and II. This shows a similar trend to the gradient of the long-period component of the linear acceleration response spectrum shown in Fig. 3. The gradient of the long-period component of the linear acceleration response spectrum for spectra I and II, was the same for the ease of handling the design earthquake motion, and the identified γ matched this trend.

The parameter α, which determines the maximum value of the yield seismic coefficient demand spectrum, reaches its maximum value when μ = 1 for each earthquake, and it gradually decreases with increasing μ. The parameter α at μ = 1 indicates the magnitude of the structural response in the elastic region. The change in α according to μ indicates the magnitude of the change rate of the yield seismic coefficient demand under inelastic response. A comparison between the observed records (JMA Kobe, JMA Kushiro) and the design earthquake motion (spectra I and II) from this perspective shows that the design earthquake motion has a larger α at μ = 1, and the change in α with changing μ is gradual. Spectra I and II are set with phase characteristics that are easily nonlinearized in the time history waveforms with the same elastic acceleration response, considering the effects of the nonlinear behavior of the structure. Our result confirms that the degree of change in α is smaller than that of the observed records, indicating the effectiveness of the phase setting of the design earthquake motion.

T_c affects the peak period of the yield seismic coefficient demand spectrum, becoming smaller with increasing μ, and the overall value is larger only in the JMA Kobe results. Figures 5 and 6 show that the peak period gradually shifts to the short-period side with increasing plasticity of the structure (i.e., longer dominant period during vibration); the peak period of the response is on the long-period side in JMA Kobe.

The coefficient β, which determines the degree of spectrum reduction on the short-period side, increases or decreases differently depending on the target earthquake motion. When targeting the ob-

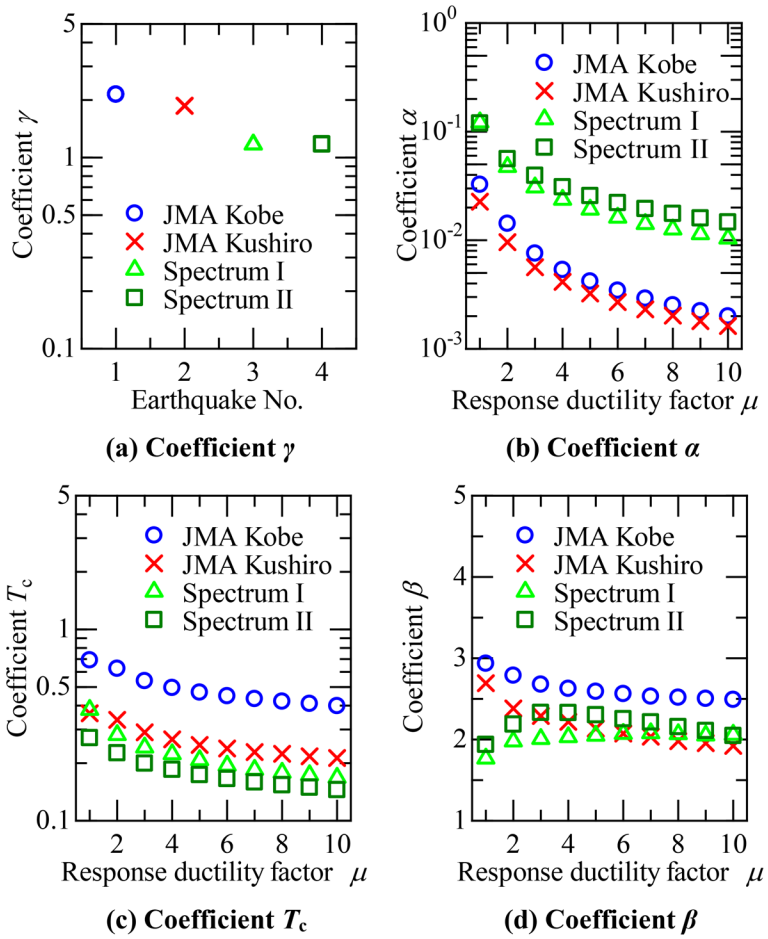

Fig. 7 Identification results for each parameter

servation records, β gradually decreases with increasing μ. This includes the effect of the target period band (T_{eq} = 0.1–5 s in this examination); however, this can be seen as the effect of the change in yield seismic coefficient demand for each period becoming smaller because of the increase in the hysteretic damping of the structure with increasing plasticity.

By setting the yield seismic coefficient demand spectrum according to Eq. (3) and the parameter estimation procedure, it was possible to appropriately reproduce the overall trend of the spectrum based on the actual earthquake motion and automatically set the spectrum shape. Therefore, a significant reduction in workload and number of parameters (74 vs. 31 for conventional vs. our examination in the range of μ = 1–10) was achieved compared to conventional visual linearization work.

3.3 Reduction of parameters and extension to arbitrary response ductility factor

The examination in the previous section confirmed that the yield seismic coefficient demand spectrum for each μ (in the range of μ = 1–10 in increments of 1) can be well determined using Eq. (3). However, when considering the design, μ and the response displacement of each structure needs to be determined arbitrarily, and a combination of T_{eq} and k_{hy} at any μ is required. Therefore, we regress the parameters α, T_c, and β using the following equations to extend the yield seismic coefficient demand spectrum to a form that can be easily displayed at any μ.

$$\log \alpha(\mu) = \sum_{n=0}^{3} k_{\alpha,n} \cdot \mu^n \tag{4}$$

$$T_c(\mu) = \sum_{n=0}^{3} k_{T_c,n} \cdot \mu^n \tag{5}$$

$$\beta(\mu) = \sum_{n=0}^{3} k_{\beta,n} \cdot \mu^n \tag{6}$$

where $k_{x,n}$ represents a coefficient for calculating each parameter x (n = 0, 1, 2, 3) and μ represents the response ductility factor ($1 \leq \mu \leq 10$).

Table 1 shows the results of calculating $k_{x,n}$ for the JMA Kobe earthquake motion studied in this examination using the least squares method. Figure 8 shows the yield seismic coefficient demand spectrum calculated using this method, which indicates that this method appropriately reproduces the spectrum of each μ. In addition, although not reported in this paper, we confirmed that the appropriate yield seismic coefficient demand spectra for the other three earthquake motions can be evaluated in a similar manner, and Eqs. (3)–(6) can be used to further reduce the number of parameters (13 in total) and set the yield seismic coefficient demand spectrum for any μ. Therefore, this setting method further improves the usefulness in design practice.

Table 1 γ and $k_{x,n}$ evaluation results (for JMA Kobe)

n	γ	$k_{a,n}$	$k_{T_c,n}$	$k_{\beta,n}$
0	2.143	-1.049	8.072×10^{-1}	3.111
1		-5.061×10^{-1}	-1.238×10^{-1}	-2.053×10^{-1}
2		6.071×10^{-2}	1.412×10^{-2}	2.538×10^{-2}
3		-2.673×10^{-3}	-5.827×10^{-4}	-1.109×10^{-3}

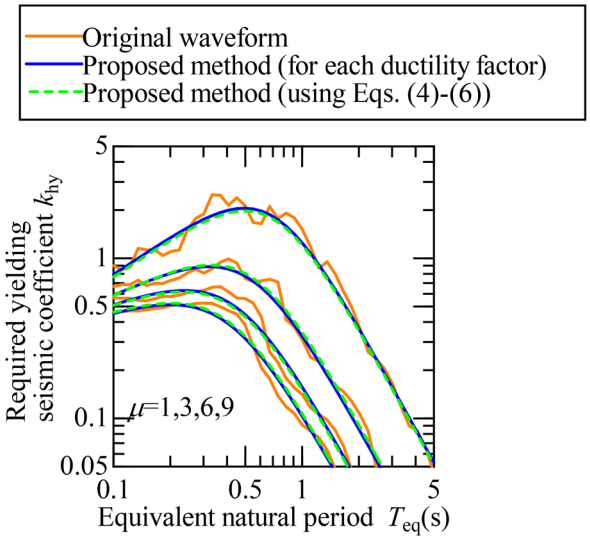

Fig. 8 Required yielding seismic coefficient spectrum fitting results (set by Eqs. (4)–(6) and Table 1)

4. Conclusion

We conducted an examination to develop a method capable of automatically setting the required yielding seismic coefficient spectrum, a key approach for representing seismic action to facilitate the calculation of nonlinear behavior during earthquakes in structural design. The results show that the proposed method can accurately and appropriately reproduce the overall trend of the spectrum. Compared to the conventional linearization process, which is performed visually, the proposed method significantly saves labor and reduces the number of parameters. This enables the design of structures with an effort comparable to using the standard L2 earthquake motion directly, even when regional characteristics are included into the design earthquake motion. As a result, the method is expected to facilitate the realization of rational structures that better reflect regional characteristics.

Furthermore, although not reported in this paper, the proposed method was applied to various earthquake observation records. The results confirmed the broad applicability of the method and showed that each coefficient exhibited a consistent tendency corresponding to changes in the characteristics of the earthquake records [4].

In this study, parameters were estimated using the least squares method to reproduce the average trend of the original waveform. However, depending on specific circumstances, additional considerations may be necessary, such as adjusting the spectrum fluctuation per period to the safer side. Appropriate parameter estimation can be achieved in such cases by introducing constraints, such as enveloping all results or exceeding them by a certain percentage. Therefore, the formulation and parameter estimation method proposed in this study are effective for setting and presenting the required yielding seismic coefficient spectrum in seismic design.

References

[1] Railway Technical Research Institute, *Design Standards for Railway Structures and Commentary (Seismic Design)*, Maruzen co., Ltd, Tokyo, 2012 (in Japanese).

[2] Iemura, H. and Mikami, T., "Demand Spectra of Yielding Strength and Ductility Factor for Required Seismic Performance Objectives," *Journal of JSCE*, No. 689/ I-57, pp. 333-342, 2001 (in Japanese).

[3] Tomonaga, H., Nishi, T., Aoyagi, H., Kanzawa, T. and Sakai, K., "Evaluation of Site Amplification Factor and Design Earthquake Motion Based on Microtremor Observation," *Journal of railway engineering, JSCE*, No. 23, pp. 155-162, 2019 (in Japanese).

[4] Sakai, K., "A Study on the Expression of Nonlinear Response Spectrum for Seismic Design of Railway Bridges and Viaducts," *Journal of Structural Engineering, A*, Vol. 70, pp. 279-288, 2024 (in Japanese).

[5] Osaki Y., *New Introduction to Spectral Analysis of Earthquake Motions*, Kajima Institute (in Japanese).

Author

Kimitoshi SAKAI, Dr. Eng.
Senior Chief Researcher, Head of Structural Dynamics and Response Control Laboratory, Center for Railway Earthquake Engineering Research
Research Areas: Earthquake Engineering, Seismic Design, Ground Motion Prediction

Method for Determining Resumption of Train Service on Railway Embankment Damaged by Rainfall

Taketo SATO **Takaki MATSUMARU**
Foundation & Geotechnical Engineering Laboratory, Structure Technology Division

Kazuki ITO
Track Structures and Geotechnology Laboratory, Track Technology Division

Takumi OZAKI
Foundation & Geotechnical Engineering Laboratory, Structure Technology Division

Since the stability of railway embankments damaged by rainfall is not easy to assess, the need for temporary restoration is often determined on the strength of experience of inspectors, or the damaged embankment is restored to its original shape. As a result, there are cases where temporary restorations are carried out with specifications which exceed what is required for embankments that already meet performance requirements for train operation. This study proposes a method for evaluating the performance of damaged embankments or temporary restoration embankments in terms of stability and settlement during train operation, and to quickly determine whether train operations can be resumed on a damaged embankment.

***Key words*:** *rainfall, embankment, stability, restoration*

1. Introduction

Recent years have seen an increase in the frequency of heavy rain and short, intense downpours, leading to an increase in rain damage to railway embankments. When precipitation exceeds limits set for train operation, train services are suspended, and safety checks are carried out to inspect facilities, such as earth structures along the railway line, before resumption of operations. If damage to an embankment is confirmed, the need for restoration is considered. If the damage is minor, the embankment will be protected with sheets or other means. When the damage is considered to be of medium seriousness or greater, and it is necessary to resume operations immediately, emergency restoration is often carried out to repair the embankment using sandbags or other means. In many cases, decisions about resuming operations and restoration are based on the experience of inspectors, and there is still room for further study.

To date few studies have focused on performance evaluation of damaged and emergency restoration embankments. This means that conditions needed to allow train operation on such embankments, are still unclear. It is assumed, therefore, that emergency restorations have probably been carried out on damaged embankments that already satisfied performance requirements to allow train operation, or that emergency restorations have been carried out to excessive specifications.

Various experiments were conducted on damaged and emergency restoration embankments to investigate their stability and dynamic subsidence properties. Experimental results were reproduced using existing stability analysis methods, and a method was proposed for quickly determining whether a damaged embankment should be restored and the specifications needed for emergency restoration.

2. Stability of embankments damaged by rainfall

Rainfall and loading experiments [1] were conducted using full-scale embankments to evaluate the stability of the damaged embankment when loaded with train-equivalent loads. A stability evaluation method for railway embankments during rainfall [2, 3] verified the reproducibility of the experimental results. The validated stability evaluation method will be used in the stability study of the damaged embankment discussed in Chapter 4.

2.1 Overview of rainfall and loading experiments

Rainfall and loading experiments were conducted using the Large-Scale Rainfall Simulator owned by the Railway Technical Research Institute. The outline of the full-scale embankment is shown in Fig. 1. The full-scale embankment is assumed to be a conventional railway embankment of 11.0 m in width, 6.0 m in depth, and 4.0 m in height, 1V:1.5H in the slope gradient and 0.70 m in thickness of roadbed ballast. The embankment material is Inagi sand, classified as a material with good constructability in the Design Standard and Commentary for Railway Structures (Soil Structures) (hereafter referred to as the Design Standard) [2].

In the rainfall and loading experiments, the embankment was sprinkled intermittently with 30 mm/h in rainfall intensity to induce the collapse of the embankment. After a partial collapse occurred, the sprinkling was stopped, and large sandbags equivalent to the train load were loaded on top of the embankment. The cumulative rainfall at the end of the experiment was 3734 mm. After the loading experiment, the large sandbags were removed, and rainfall sprinkling continued until the prescribed collapse occurred. The rainfall-induced failures of the embankment were targeted up to the toe of the slope (hereafter referred to as small collapse), up to the middle of the slope (hereafter referred to as medium collapse), and up to the shoulder of the slope (hereafter referred to as significant collapse).

2.2 Stability of the damaged embankment under train loading

The appearance during the loading experiments at each col-

lapse phase is shown in Fig. 2, and the sketch of the collapsed embankment shape is shown in Fig. 3. As shown in Fig. 2, no visible progression of the collapse was observed in each collapse phase, even when large sandbags equivalent to the train load were loaded. Figure 3 shows that the collapse areas observed in each phase were located on the slope side of the embankment, below the 45-degree line starting from the loading end of the large sandbags. This 45-degree line is the zone influenced by the train load in the new construction design. The loading experiments were carried out under conditions where the collapse zone did not extend into the influence zone of the train load.

The changes in bearing capacity properties with the progression of collapse are discussed by evaluating the depth distribution of converted N-values N_d correlated with bearing capacity properties at each collapse phase. The depth distribution of converted N-values N_d obtained by the portable dynamic cone penetration test carried out at the locations shown in Fig. 1 is shown in Fig. 4. The collapse heights for each collapse phase shown in Fig. 3 are also shown in Fig. 4. In the case of significant collapse, only the test was carried out in the crest because the collapse area extended to the slope shoulder. Converted N-values N_d for small and medium collapse identified at the slope shoulder (Fig. 4 (a)) showed a decrease near the bottom of the embankment compared to before the rainfall sprinkling. The decrease in converted N-values N_d was observed in the lower range, starting at about 0.5 m below the collapse height for each phase. On the other hand, no such change in the depth distribution of converted N-values N_d was observed at the crest (Fig. 4 (b)). The decrease in converted N-values N_d observed at the slope shoulder is presumably due to the decrease in confining pressure caused by the collapse. However, the fact that no decrease in converted N-values N_d was observed at the crest suggests that the slope collapse had only a minor effect on the bearing capacity characteristics immediately below the crest.

The time histories of the slope shoulder settlement during rainfall and loading experiments are shown in Fig. 5. The loading histories of the loading experiments conducted at each collapse phase are also shown in the figure. The settlement at the slope shoulder was 3.1 mm at the onset of the small collapse and progressed to 4.1 mm with the loading. Subsequent collapse progression and loading experiments showed settlement progression to 6.1 mm. In the significant collapse, after 166.6 kN had been loaded, the load was increased to 236.6 kN, but the settlement progress was insignificant.

In conclusion, it was confirmed that the damaged embankment of the collapse scale confirmed in this experiment had a certain degree of stability against loading equivalent to that of a train.

2.3 Stability analysis to reproduce experimental behavior

The stability analysis method for railway embankments during rainfall was used to study the reproducibility of the embankment collapse shape. Circular slip stability analyses [2, 3] were carried out using the analytical models, considering the degree of saturation distribution and the water level in the embankment obtained from the seepage flow analysis.

Table 1 shows the strength characteristics used in the stability analysis. The strength characteristics were determined based on the results of saturated and unsaturated triaxial compression tests on the Inagi sand used in the rainfall and loading experiments. The strength characteristics are determined at threshold values of 80% and 100% in the degree of saturation. The stability analysis model was established by applying each strength characteristic to the degree of saturation distribution evaluated by the seepage flow analysis.

An overview of the cohesion used in the stability analysis is shown in Fig. 6. The cohesion in the unsaturated state was evaluated

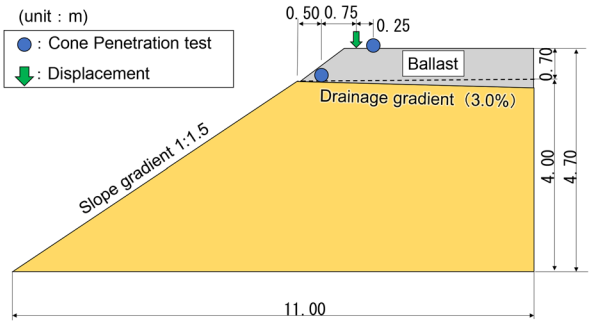

Fig. 1 Outline of full-scale embankment for rainfall and loading experiments

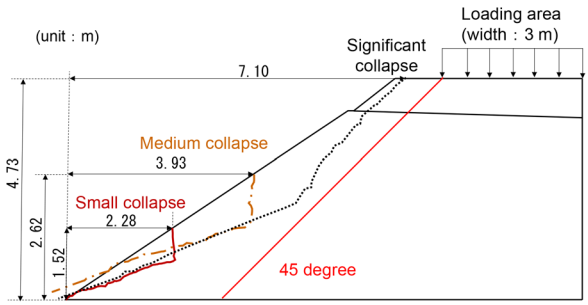

Fig. 3 The sketch of the collapsed embankment shape

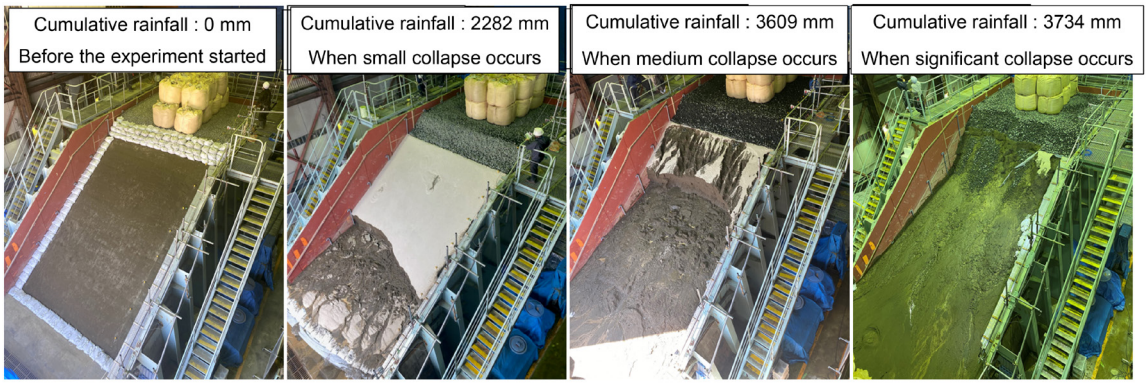

Fig. 2 Appearance of loading experiments at each collapse phase

to be small by treating the internal friction angle in the unsaturated state as approximately equal to that in the saturated state because the cohesion significantly impacts the stability analysis results. In other words, as shown in the figure, if the internal friction angle in the unsaturated state is assumed to be equal to that in the saturated state, the resulting cohesion c is less than the cohesion c_{net}.

For the circular-slip stability analysis, only the embankment body was considered and the roadbed ballast was considered with a distributed load of 10.2 kN/m^2. For the case simulating the loading experiment, 29.2 kN/m^2 of distributed load was considered in the area where large sandbags were loaded.

Figure 7 shows the stability analysis results for the medium collapse case. The red and orange lines show that the slip surface has a factor of safety below 1.0, indicating that the collapse will occur at this slip surface. In the case of the occurrence of the medium collapse shown in Fig.7 (a), the slip surface is reproduced in general agreement with the experimentally obtained collapse geometry by considering the cross-sectional geometry of the small collapse.

In the case of the collapse(medium) shown in Fig.7 (b), slip surfaces below a factor of safety of 1.0 occurred in the loading range, which differs from the behavior confirmed experimentally in the experiments where no collapse progression was observed during loading experiments. It is assumed that the causes are (i) the method for evaluating the strength of the embankment material and (ii) the influence of load dispersion of the overburden load. Regarding (i), the internal friction angle in the unsaturated state is generally smaller than that in the saturated state, and the cohesion in the unsaturated state tends to be greater than that in the saturated state. However, in this study, the internal friction angle in the unsaturated states was the same as that in the saturated state, and the cohesion in the unsaturated state was considered minor. This is because the value of cohesion, which significantly affects the analysis results, is assumed to be minor, allowing the results to be on the safe side. Regarding (ii), although the stress acting on the slip surface is assumed to be reduced by the dispersion of the overburden load in the ground, the stability analysis assumes that the embankment body is rigid and does not consider load dispersion. Therefore, the influence of the overburden load on the slip force is considered significant. Due to these factors, the analysis results for the loading case are considered that the factor of safety is low compared to the experimental results.

3. Dynamic subsidence properties of damaged and emergency restoration embankments

This chapter presents the results of evaluating embankment dynamic subsidence properties using model tests simulating their damaged and emergency restored states. The results obtained in this chapter are used to determine the range of collapse to be covered by the damaged embankment stability nomogram shown in Chapter 4, and to determine the standard specifications for emergency restoration using large sandbags.

3.1 Dynamic subsidence properties corresponding to extent of damaged embankment collapse

In this study, cyclic loading tests were carried out using the embankment model to simulate the collapse of the embankment slope. Figure 8 shows an overview of the embankment model. The model was constructed at a scale of 1:5, and its depth is 1.0 m, which corresponds to the length of seven sleepers.

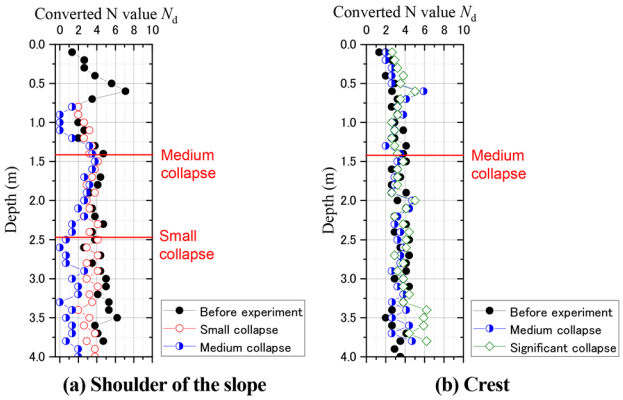

Fig. 4 Depth distribution of converted N-values N_d

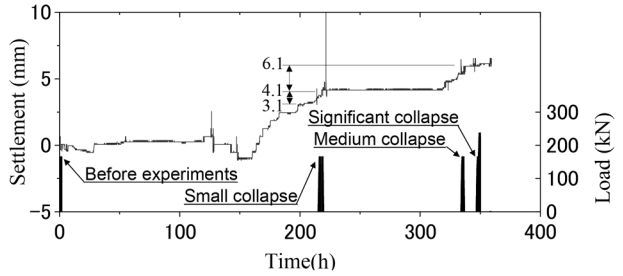

Fig. 5 Time history of settlement at the shoulder of the embankment

Table 1 List of the strength characteristics of embankment material used in the stability analysis

Degree of saturation S_r (%)	Unit volume weiht γ_t (kN/m^2)	Internal friction angle φ (°)	Coheision c (kN/m^2)
$S_r < 80$	17.3	36.1	6.5
$80 \leqq S_r < 100$	18.2	36.1	2.4
$S_r = 100$	19.1	36.1	0.9

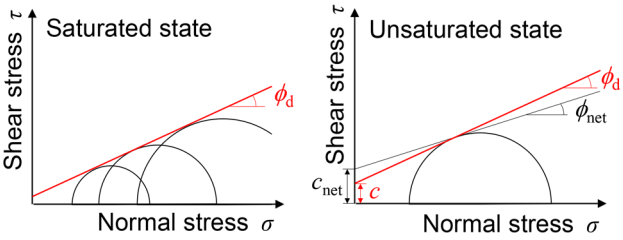

Fig. 6 An overview of the cohesion used in the stability analysis

The dimensional effect on the applied load is proportional to the third power when the stress and strength of the geomaterial are considered. Therefore, the applied load for one carriage (160 kN per axle × 2 axles = 320 kN) is reduced to 2.56 kN when scaled down by a factor of 1:5^3. On the other hand, the effect of scale cannot be considered in terms of the influence of cohesion (suction) between soil particles of the Inagi sand used as fill material. This fact caused a concern, as even with load, in which the size effect was considered, the deformation would be small. A static linear elastic analysis was therefore carried out using a 1:5 scale embankment model to ensure the deformation where the scale is considered specifically, and a load of 7.68 kN, which would result in a sleeper displacement

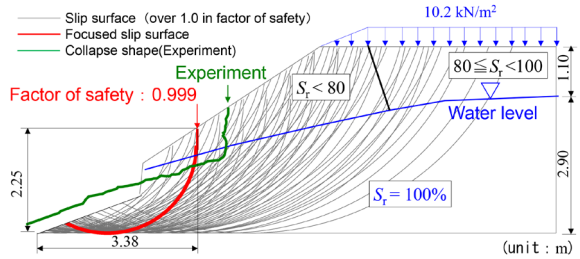

(a) At the onset of medium collapse

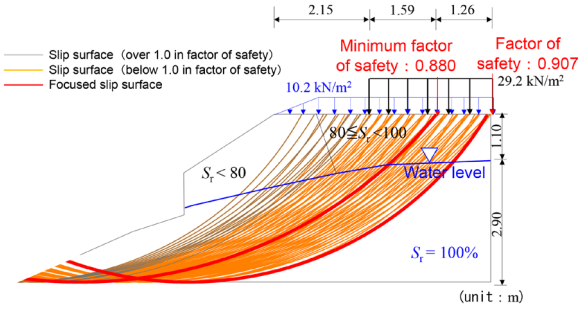

(b) During the loading experiments under medium collapse conditions

Fig. 7 Results of the stability analysis

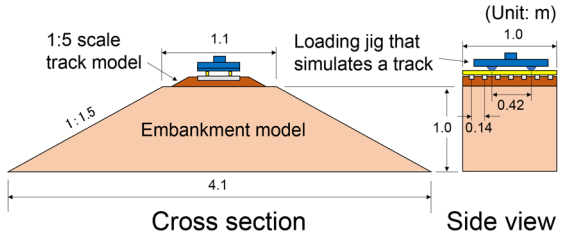

Fig. 8 Outline of the embankment model for cyclic loading test

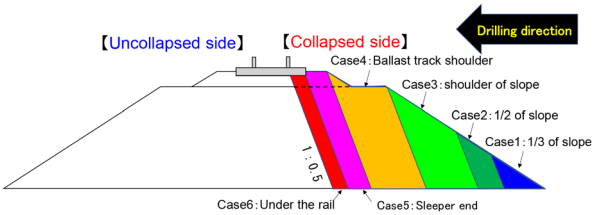

Fig. 9 Range of embankment excavation changed according to test cases

of approximately 0.2 mm (approximately 1.0 mm in actual size), was used for the model test. Previous studies [4] have shown that the track displacement progress tends to increase when roadbed displacement (elastic deformation) exceeds approximately 1.0 mm, when a train passes over it. Considering that the elastic deformation of the ballast roadbed is relatively small and that the roadbed displacement and sleeper displacement show close values, a sleeper displacement of 1.0 mm was set as the target displacement in actual size.

In this study, six cases of cyclic loading tests were carried out using different excavation ranges to simulate collapse. The extent of embankment excavation for each test case is shown in Fig. 9. In this study, the same embankment model was used, and the tests were carried out in order of case number. Hence, the evaluation from Case 2 onwards includes the effect of the loading history of the previous tests. The number of cyclic loadings for each test case was set at 100,000 cycles for Cases 1 to 5, and Case 6 was discontinued after 20,000 cycles due to the significant progress in sleeper settlement.

The sleeper settlement and its displacement amplitude at the last loading cycle for each case are shown in Fig. 10. Note that the sleeper settlement was reset to 0 mm for each case. No significant changes in sleeper settlement and displacement amplitude were observed from Cases 1 to 4, but significant increases in both sleeper settlement and displacement amplitude were observed in Cases 5 and 6. These results indicate that the cumulative settlement of the ballasted track would not be significant if the collapse of the embankment did not extend to the side of the track above the shoulder of the roadbed.

3.2 Dynamic subsidence property of the emergency restoration embankment with large sandbags

The effect of repeated loading on the suppression of track settlement was evaluated for the emergency restoration embankment with large sandbags. Figure 11 shows the appearance of the emergency restoration embankment model. In this test, there were two cases of embankments with different collapse areas which were assumed to have had emergency restoration using large sandbags. These were Case 7 (which collapsed up to the shoulder of the embankment slope), and Case 8 (which collapsed up to the edge of the sleeper). The large sandbags were constructed to the same 1:5 scale as the embankment model. Each case (Case 7 and 8) was examined with the two rows of large sandbags placed on top of the embankment, and with the large sandbags removed, respectively.

Figure 12 shows the settlement at the edge of the sleeper on the collapsed side. In Case 7, where the collapse occurred to the shoulder of the slope, there was little change in the amount of settlement with or without the sandbags, as shown in Fig. 12 (a). On the other hand, in Case 8, where the collapse occurred to the edge of the sleeper, the amount of settlement of the sleeper increased by a factor of two in the case that the sandbags were removed, as shown in Fig. 12 (b).

These results confirm that even if the embankment collapses up to the edge of the sleeper, emergency restoration using large sandbags can reduce the cumulative settlement of the ballasted track to the same extent as the area of the embankment collapse does not reach the shoulder of the roadbed.

4. Method for determining the resumption of operation on embankments damaged by rainfall

This chapter examines nomograms that determine the stability of damaged embankments according to the shape of the collapse. When the stability is not satisfied, standard specifications for emergency restoration using large sandbags can be utilized. The chapter also proposes the decision-making method for resuming train operations using these results.

4.1 Nomograms for the stability of damaged embankments

In this study, the stability analysis method validated in Chapter 2 was used to evaluate the stability of the damaged embankments under train loading, which changed the conditions such as collapse shape and water level in the embankment. The results of the study showed that the range in which the embankment satisfies stability

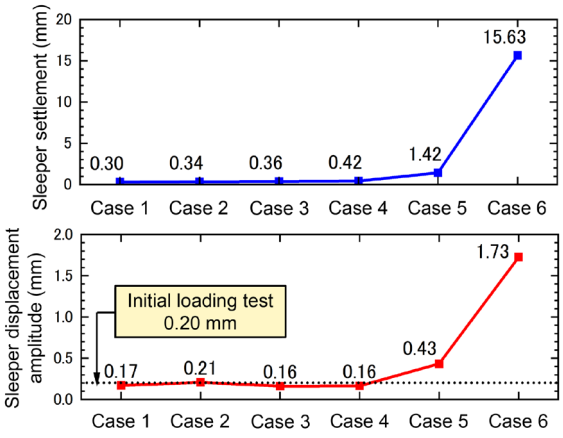

Fig. 10 Result of cyclic loading test for each cases

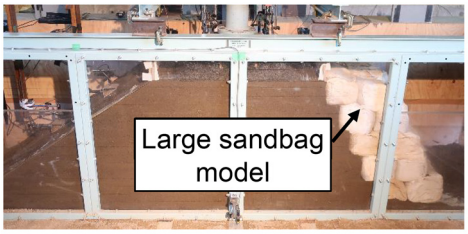

Fig. 11 The appearance of the emergency restoration embankment model (Case 7)

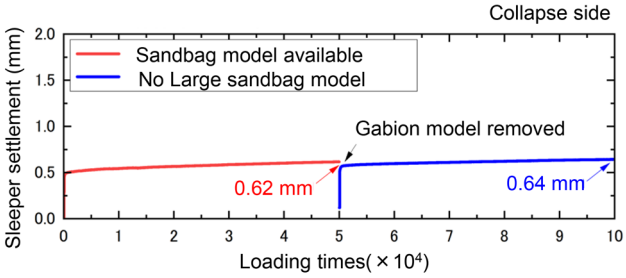

(a) Case 7: the emergency restoration embankment model where collapse reaches up to the shoulder of the embankment slope

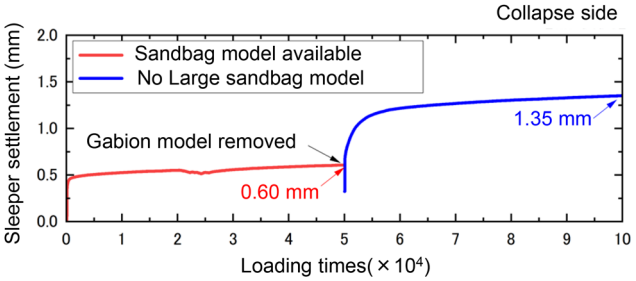

(b) Case 8: the emergency restoration embankment model which collapse reaches up to the edge of the sleeper

Fig. 12 Effect of sandbags on settlement

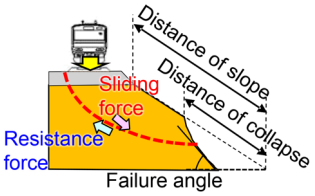

Fig. 13 Outline of the index used for nomogram

under train loading is organized by the relationship between the collapse distance ratio and the collapse angle, as shown in Fig. 13. Note that the collapse angle is the ratio of the collapse distance and slope length in the slope direction. In Chapter 3, it was confirmed that the dynamic subsidence of the track due to train running is slight if the scale of collapse is up to the shoulder of the embankment slope. Therefore, this study considered the range of collapse up to the shoulder of the embankment.

Figure 14 shows the nomogram for the stability of the damaged embankment under train loading. The plots in the figure show the conditions under which the stability analysis was carried out. The green areas represent regions where the factor of safety exceeds 1.0, indicating that stability is ensured. Red plots represent conditions where the factor of safety is less than 1.0 and stability is not satisfied. Areas of satisfactory and unsatisfactory stability are classified based on the results. In the stability analysis, relatively safe strength characteristics were used, specifically, internal friction angle φ = 30°, and cohesion c = 5 kPa were obtained by geotechnical material tests of existing embankment material classified as soil type 3 in the Japanese railway design standard [2]. The circular-slip resistance coefficient was set to f_{rs} = 0.91, considering that the structure is temporary and the trains run slowly.

Taking the case where soil type and water level are unknown under train loading, for example, at an embankment height of 3 m, a region satisfying the stability for resumption of train operation is observed when the collapse angle is slight, and it is possible to resume train operation without emergency restoration. On the other hand, at an embankment height of 6 m, stability is not satisfied for any combination of collapse distance ratio and angle, so emergency restoration is required.

Consequently, when detailed information about an embankment, such as its water level and strength characteristics of reinforcement materials can be obtained through field investigations, the area that satisfies stability can be extended to cases where soil conditions and water level are unknown. The damaged embankment, whose stability is, can be used without the need for emergency restoration, and trains are expected to be able to resume operations soon.

4.2 Standard specifications for emergency restoration of damaged embankments

A study on the placement of large sandbags is carried out to simplify the restoration specifications in the case of emergency restoration. Specifically, the placement of large sandbags was examined to satisfy the stability of sliding and overturning failure [5] of large sandbags against earth pressure acting on large sandbags under train loading.

Figure 15 shows the standard specifications of the embankment for emergency restoration with large sandbags. Six cases, according to the availability of information on soil conditions and water level in the embankment, were examined, changing the height of the embankment. In cases where the soil conditions and water level were unknown, the internal friction angle of the embankment material was set to 30°, and the water level in the embankment was set to one-third of the embankment height. The cohesion of the embankment material was not considered, and the effect of the water level

in the embankment on its stability was considered as the water pressure acting on the sandbags. When local conditions were deemed good after field surveys and tests, the standard specifications for emergency restoration were examined according to actual conditions.

For example, in the case where the water level of the embankment was low, it was not taken into account. In the case where the internal friction angle of the embankment material was large, a stability analysis was carried out with $\varphi = 35°$ as its internal friction angle. In the stability study, the allowable factor of safety against sliding was set to 1.1. The sliding stability was verified by comparing the earth pressure acting on the embankment with the frictional resistance at the bottom of the embankment due to the dead weight of the embankment. Toppling failure was verified at the point where the combined force of the earth pressure and the dead weight of the sandbags acted on the embankment. The allowable eccentricity was set to be one-third of the width of the bottom of the sandbag from the center point of the bottom of the sandbag.

In the case of unknown soil conditions and water level, it is necessary to ensure a safety factor against sliding caused by earth pressure and water pressure at any embankment height. Therefore, the number of sandbags at the lowest level should be three rows at a height of 3 m and four at a height of 6 m. On the other hand, when there is no water level in the embankment, the water pressure does not act on the sandbags. Therefore, this means that the arrangement of large sandbags in the restoration embankment with a height of 3 m is the same as when the soil conditions and water level are unknown. As a result, the number of sandbags can be reduced by one row for a height of 6 m. In addition, when the internal friction angle of the embankment material is large, the overall earth pressure acting on the sandbags is reduced. In this case, the number of sandbags is then reduced from two to one in the third and fourth rows from the top for an embankment 6 m high.

Using this selection table, as shown in Fig. 15, emergency restoration can be carried out according to local conditions, and furthermore, the number of sandbags can be reduced compared to conventional restoration.

4.3 Method for determining resumption of operations on embankments damaged by rainfall

Figure 16 shows the method for determining resumption of

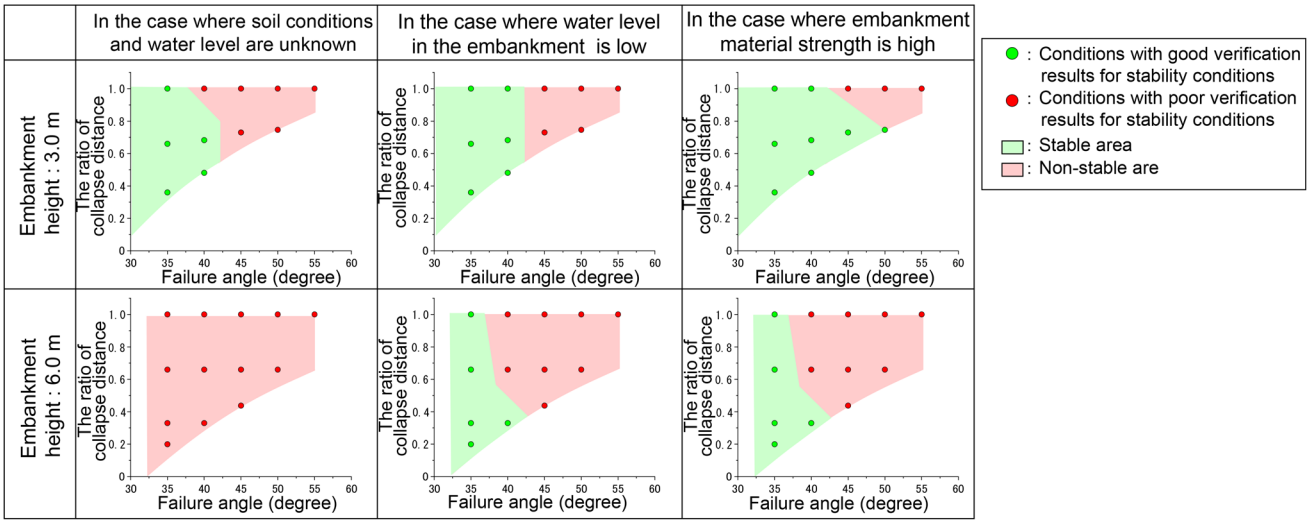

Fig. 14 Nomogram of stability of a damaged embankment under a train load

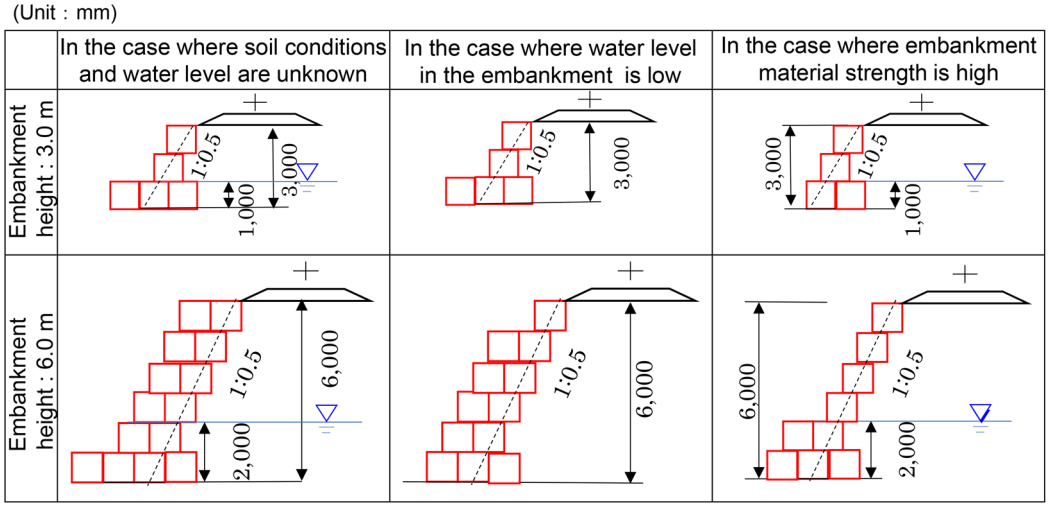

Fig. 15 Standard specifications for embankments for emergency restoration with large sandbags

operations on embankments damaged by rainfall. In this method, the stability of the affected embankment under train loading is assessed using the nomogram shown in Fig. 14, according to height of the embankment and the collapse geometry.

This study is carried out in cases where the soil conditions and water table are unknown. If the results are not satisfactory, further field surveys can be conducted to obtain information on the embankment.

Suppose information such as the embankment's water level and the embankment material's strength can be obtained. In that case, a nomogram based on the local conditions can determine whether emergency restoration is required according to the situation. If emergency restoration is required, the specifications can be quickly determined based on the standard specifications shown in Fig. 15.

Note that the proposed method is intended to facilitate early resumption of operations. When operations are resumed speed restrictions should be put in place, and trains operated with lower operating limits than usual during rainfall. It should be noted that the saturation and water level in the embankment after the cessation of rainfall are expected to decrease with time. However, it should be remembered that significant settlement may occur if the saturation and water level are high.

5. Conclusions

This paper focuses on embankments which have sustained damage and undergone emergency restoration. Stability of an embankment was examined according to type of collapse and its dynamic subsidence properties were clarified through loading tests to simulate repeated passing of trains. A nomogram to guide decisions on whether emergency restoration work is needed or not, and a method to support decisions about when train operations can be resumed based on standard emergency restoration specifications, were also developed. The proposed method is expected to help quickly determine the need for emergency restoration of embankments damaged by rainfall.

In the future, this method is expected to inform not only emergency restoration but also main restoration work. In addition, a rapid restoration method that does not involve an emergency restoration step will be studied. It is planned to compile the outcome of this work into a 'Restoration Manual for Damaged Embankments.'

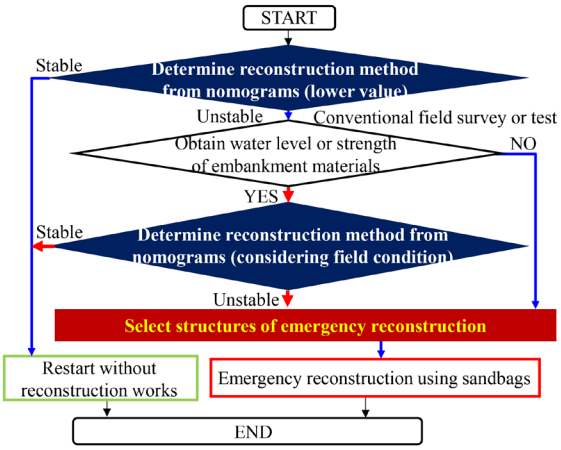

Fig. 16 The method for determining the resumption of operation of damaged embankments

Acknowledgment

This research was funded in part by a railway technology development subsidy from the Ministry of Land, Infrastructure, Transport and Tourism.

References

[1] Matsumaru, T., Sato, T., Ito, K. and Ozaki, T., "Emergency reconstruction method of embankment damaged by rainfall," *Japanese Railway Engineering*, No. 221, pp. 21-23, 2024.

[2] Railway Technical Research Institute, *Design standard for railway structure and commentary (Earth structures)*, 2007.

[3] Kojima, K. and Tateyama, M., "Seepage Analysis of Rainfalls for Embankments," *RTRI Report*, Vol. 19, No. 10, pp. 39-44, 2005 (in Japanese).

[4] Sekine, E. and Muramoto, K., "Bearing Capacity of Actual Existing Roadbed," *RTRI Report*, Vol. 9, No. 7, pp. 19-24, 1995 (in Japanese).

[5] Railway Technical Research Institute, *Design standard for railway structure and commentary (Retaining structures)*, Maruzen Publishing Co., Ltd., 2012 (in Japanese).

Authors

Taketo SATO
Assistant Senior Researcher, Foundation and Geotechnical Engineering Laboratory, Structure Technology Division
Research Areas: Geotechnical Engineering

Kazuki ITO, Ph.D.
Senior Researcher, Track Structure and Geotechnology Laboratory, Track Technology Division
Research Areas: Track Engineering

Takaki MATSUMARU, Ph.D.
Chief Researcher, Foundation and Geotechnical Engineering Laboratory, Structure Technology Division
Research Areas: Geotechnical Engineering

Takumi OZAKI
Assistant Senior Researcher, Foundation and Geotechnical Engineering Laboratory, Structure Technology Division
Research Areas: Geotechnical Engineering

Wear Mechanism of Current Collecting Materials due to Frictional Heat

Chikara YAMASHITA **Koki NEMOTO**
Current Collection Maintenance Laboratory, Power Supply Technology Division

To reduce wear of current collecting materials such as contact wires and contact strips on electric railways, it is necessary to clarify the wear mechanism, especially mechanical wear due to frictional heat. In this study, the authors carried out wear tests using a new rotary wear tester capable of measuring the contact temperature and analyzed the temperature rise using a new contact model that takes into account the number of contacts. From the test and analysis results, the authors classified wear modes into four types based on the softening of materials and clarified that the seizure wear mode occurs when the contact pressure exceeds the hardness of the material.

Key words: *mechanical wear mode, frictional heat, contact temperature, softening, hardness, contact pressure*

1. Introduction

In electric railways, current collecting materials such as the contact wire and the contact strip are subject to wear due to friction under current flow conditions and the timing of their replacement depends on the rate of wear. Therefore, in order to reduce the maintenance costs, it is necessary to clarify the wear mechanism and take measures for reducing the wear.

The wear modes of current collecting materials have been conventionally classified into two types: electrical wear caused by an arc discharge at contact loss point, and mechanical wear caused by contact adhesion [1-4]. However, in reality, wear phenomena are diverse and cannot be explained by just these conventional classifications.

Recently, the authors carried out wear tests with a linear wear tester capable of measuring the contact temperature caused by Joule heat and analyzed the temperature distribution around contact spots [5, 6]. From test and analyses results, the authors classified electrical wear modes into three types and clarified that these mode transitions occur due to a molten bridge occurring prior to arc discharge. However, mechanical wear mechanisms have not yet been clarified.

In this paper, the authors therefore develop a rotary tester capable of measuring the contact temperature caused by frictional heat and carry out wear tests in order to classify mechanical wear modes. The authors then clarify the mechanism of occurrence of these modes based on the contact temperature and the number of contacts.

2. Wear tests and test results

2.1 Wear tester and test conditions

The rotary wear tester developed to monitor the contact temperature during the test is shown in Fig. 1. The contact strip specimen is pressed against the rotating copper plate which imitates the contact wire. The contact force N [N] and the friction force F [N] are measured with bi-axial load cells set between the contact strip and the linear actuator. The contact temperature T [K] is calculated from thermoelectromotive force V [μV] using (1) [7].

$$T = \frac{V}{S} + T_0 \quad (1)$$

Here, S is the relative Seebeck coefficient [μV/K], T_0 is the temperature at the electric potential measurement point [K].

The material properties of each specimen are shown in Table 1. The copper plate and contact strip should be of different materials because otherwise the relative Seebeck coefficient is 0. As test conditions, the apparent contact area between the contact strip and the copper plate is 10×10^{-4} m^2, the contact force is set to 30 N, 60 N, 80 N, and the sliding speed is set to 0.56-27.8 m/s. The sliding time is set to within 60 s so that the temperature at the electric potential measurement point does not rise more than 10 K.

2.2 Test results

Figure 2 shows the classification of four types of wear mode for each test condition. The wear modes are classified based on the contact temperature shown in Fig. 3, the friction coefficient shown in Fig. 4 and the observation results of typical wear surface and wear

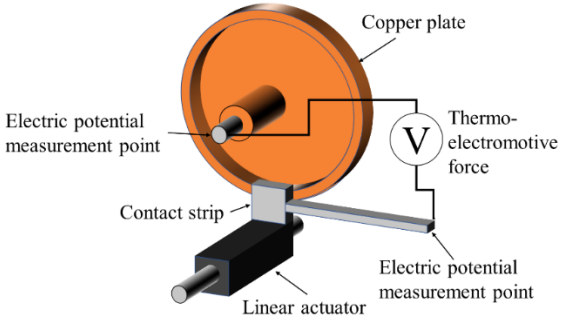

Fig. 1 Diagram of rotary wear tester

Table 1 Material properties

Specimen	Copper plate	Contact strip
Material	Tough pitch copper	Iron-based sintered alloy
Principal component	Cu	Fe
Additive	-	Cr, MoS_2, Bi, BN
Softening point	Approximately 473 K	Approximately 673 K
Relative Seebeck coefficient	9.6 μV/K	

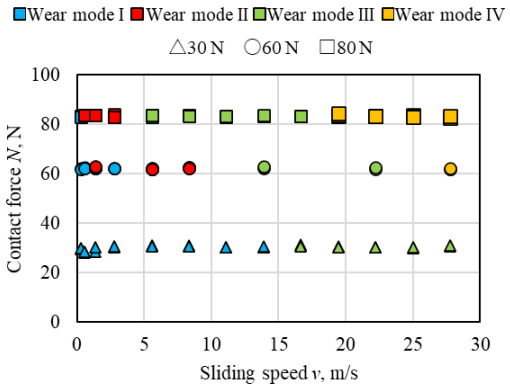

Fig. 2 Occurrence condition of each wear mode (test condition)

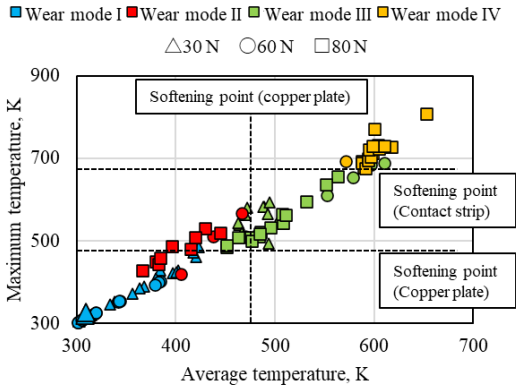

Fig. 3 Occurrence condition of each wear mode (contact temperature)

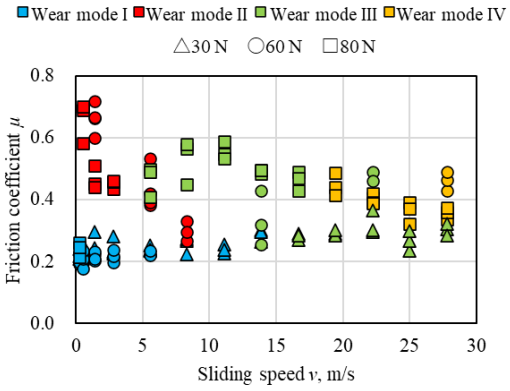

Fig. 4 Relationship between sliding speed and friction coefficient for each mode

particles shown in Fig. 5. In Fig. 3, the horizontal axis is the average temperature, and the vertical axis is the statistical maximum temperature calculated by adding 3σ (σ: standard deviation) to the average temperature. The softening points of both materials are shown as dashed lines in Fig. 3. In Fig. 5, wear surfaces are observed using an optical microscope and the wear particles are observed using scanning electron microscope (SEM). The four types of wear modes are specifically classified as follows:

(i) Wear mode I

This wear mode is observed under conditions of relatively low sliding speed and low contact force as shown in Fig. 2. Note that neither material will soften, since even the maximum temperature is below the softening point of the copper plate as shown in Fig. 3.

The features of this mode are that the friction coefficient is in the range of 0.2-0.3 regardless of the sliding speed, as shown in Fig. 4, and the size of wear particles is in the order of a few microns, shown in Fig. 5. Coulomb's law [8] states that the friction coefficient does not depend on the sliding speed and that the wear particles become finer in the adhesive wear mode.

Based on these features, wear mode I is classified as the adhesive wear mode. This classification indicates that the other wear modes are not adhesive wear modes, and is an important classification.

(ii) Wear mode II

This wear mode is observed under conditions of relatively low sliding speed and high contact force as shown in Fig. 2. In Fig. 3, the average temperature is below the softening point of the copper plate, but the maximum temperature is around the softening point. This means that wear mode II occurs under the conditions where the copper plate temporarily softens but the contact strip never softens.

The features of this mode are that the friction coefficient is greater than for wear mode I and tends to decrease as the sliding speed increases, as shown in Fig. 4, and the contact force fluctuates significantly due to stick-slip. In addition, the copper plate surface becomes significantly rougher as shown in Fig. 5.

These features suggest that significant sticking, like a seizure, occurred at the contact spot, causing stick-slip and roughening of the wear surface. It should be noted that although the wear mode II is clearly different from the wear mode I, both modes can occur under the same conditions as shown in Fig. 2. The mechanism of the wear mode II is clarified by considering the difference from wear mode I and the speed dependence of the friction coefficient is considered in Chapter 3.

(iii) Wear mode III

This wear mode is observed under conditions of moderate sliding speed as shown in Fig. 2. In Fig. 3, the average temperature is above the softening point of the copper plate, but the maximum temperature is below the softening point of the contact strip. This means that the wear mode III occurs under the conditions where the copper plate softens on average, but the contact strip never softens.

The features of this mode are that the friction coefficient increases as the contact force increases as shown in Fig. 4, and the copper plate surface shows wear tracks along the sliding direction as shown in Fig. 5. Wear tracks on the copper plate are also observed in wear mode I. The differences between wear mode III and wear mode I are that many copper pieces are transferred to the contact strip surface and the wear particles of the wear mode III are long and thin.

These features of the wear mode III are consistent with those of abrasive wear mode [9]. The abrasive wear occurs when there is a large difference in hardness between two materials, and the harder material digs into the softer material, producing long and thin wear particles. The friction coefficient in the abrasive wear mode increases as the amount of indentation of an asperity increases [10]. Therefore, it is sufficiently considered that the indentation of contact strip asperities increases as the contact force increases, resulting in an increase in the friction coefficient as shown in Fig. 4.

(iv) Wear mode IV

This wear mode is observed under conditions of high sliding speed and high contact force as shown in Fig. 2. As shown in Fig .3, the average temperature is above the softening point of the copper plate, and the maximum temperature is above the softening point of the contact strip. This means that the wear mode IV occurs under the

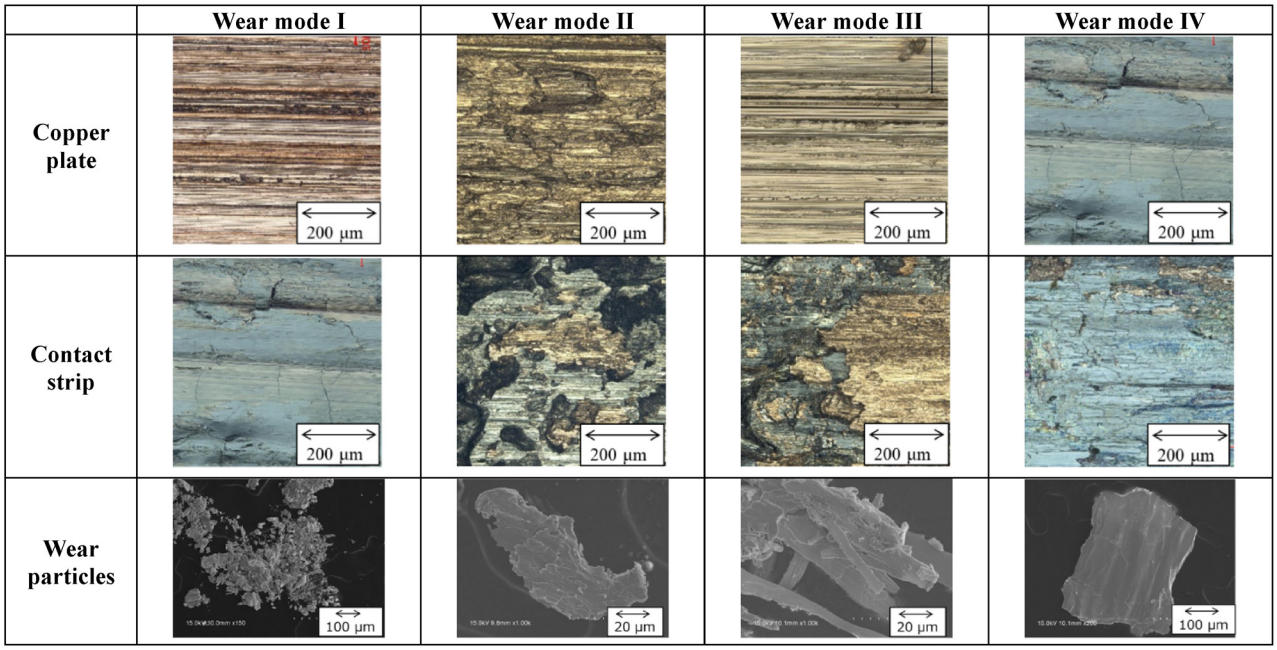

Fig. 5 Optical microscope images of wear surface and SEM images of wear particles (sliding directions in wear surface are from left to right)

conditions where both materials soften.

The features of this mode are that the friction coefficient tends to decrease as the sliding speed increases, as shown in Fig. 4. From the observation result as shown in Fig. 5, the copper plate surface is smooth and an iron, which is the main component of the contact strip, is transferred to the surface. There are some cracks and peeling marks on the copper plate surface. On the other hand, some plastic flow marks in the sliding direction are observed on the contact strip surface. Wear particles are wavy flakes that seem to have peeled off from the copper plate surface.

Based on these features, the authors consider the mechanism of the wear mode IV. In this mode, both materials soften and undergo plastic flow, resulting in iron transfer to the contact wire surface. The shearing force due to friction force accumulates in the subsurface of the copper plate because the wear amount due to the plastic flow is small, resulting in cracks on the surface. These cracks lead to delamination wear [11] and peeling wear [12], resulting in flake wear particles. It is assumed that the sliding contacts between the copper plate and the contact strip are terminated by softening of the contact strip, regardless of the sliding speed. Since the softening point of the contact strip is constant and the softening occurs due to temperature increase caused by the friction force and sliding speed, the friction force decreases as the sliding speed increases in this mode. This is the reason why the friction coefficient in wear mode IV decreases as the sliding speed increases in Fig. 4.

3. Analysis of wear mode II mechanism

In this chapter, the authors analyze the wear mode II mechanism in terms of differences with wear mode I. It has been previously reported that a reduction in the number of contacts is one of the factors leading to sticking and seizure at the contact spot as observed in the wear mode II [13]. Therefore, the authors estimate the number of contacts in wear mode I and II using a heat conduction analysis.

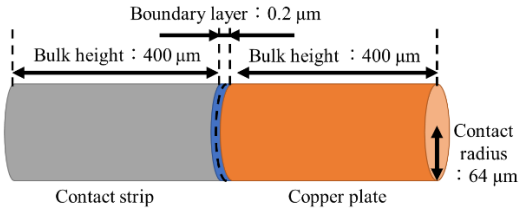

Fig. 6 Analysis model

3.1 Analysis model

The authors use the analysis software FEMTET, which is capable of unsteady heat conduction analysis. The analysis model is a static contact between two cylinders, as shown in Fig. 6. There is the boundary layer between the copper plate and the contact strip which is a mixture of both materials. By inputting frictional heat into this layer, it is not necessary to consider the heat distribution rate which has not been determined. The heat transfer properties of the boundary layer are assumed to be the average of the transfer properties of the copper plate and the contact strip as follows:

$$\rho_B = \frac{\rho_C + \rho_S}{2} \tag{2}$$

$$\lambda_B = \frac{2\lambda_C \lambda_S}{\lambda_C + \lambda_S} \tag{3}$$

$$c_B = \frac{c_C + c_S}{2} \tag{4}$$

Where, ρ is the weight density [kg/m^3], λ is the thermal conductivity [W/(mK)], c is the specific heat [J/(kgK)], and the subscripts B, C and S represent the boundary layer, the copper plate and the contact strip, respectively.

The frictional heat Q [W] input into the boundary layer is calculated by (5). It is assumed that the work done by friction is not 100% converted into frictional heat but also converted into friction noise and contact erosion. Therefore, the work done by the friction

is converted into frictional heat by multiplying it by the heat conversion efficiency η.

$$Q=\eta\frac{\mu N v}{n} \tag{5}$$

Where, μ is the friction coefficient, N is the contact force [N], v is the sliding speed [m/s] and n is the number of contacts calculated using (6) proposed by Lim and Ashby [12].

$$n=\left(\frac{r_0}{r_a}\right)\left(\frac{N}{A_0 H_0}\right)\left(1-\frac{N}{A_0 H_0}\right)+1 \tag{6}$$

Where, r_a is the radius of real contact area [m], r_0 is the radius of apparent contact area [m], A_0 is the apparent contact area [m^2] and H_0 is the hardness of the copper plate [Pa]. The analysis time t [s] is calculated by (7) as relative sliding time.

$$t=\frac{2r_a}{v} \tag{7}$$

The boundary conditions are that the temperatures at the end of both cylinders are set to 298 K and that the circumferences of both cylinders are insulated. Since both cylinders are assumed to be in perfect contact, the heat transfer resistance between them is set to zero. The analysis parameters and material properties are shown in Tables 2 and 3.

The output of analysis is the maximum temperature rise in the boundary layer from room temperature, since the thermoelectromotive force in Fig. 1 is theoretically dependent on the temperature difference between contact surface and the electric potential measurement point (= room temperature). According to previous study between the analytical accuracy and the model size [14], the bulk height is set to 400 μm, the thickness of the boundary layer is set to 0.2 μm, and the mesh size of the boundary layer is set to 0.1 μm.

3.2 Analysis results

As an example of the analysis results, the estimated contact temperature rise under the condition of η 0.6 is shown in Fig. 7 (a), and the average temperature rise measured for comparison is shown in Fig. 7 (b). The analysis error δ for each wear mode is calculated by (8).

Table 2 Analysis parameters

Radius of real contact area r_a, m	64x10^{-6}
Apparent contact area A_0, m^2	100x10^{-6}
Radius of apparent contact area r_0, m	5.6x10^{-3}
Vickers hardness of copper plate H_0, Pa	980x10^6
Heat conversion efficiency η	0.4–0.8

Table 3 Material properties

	Copper plate	Contact strip	Boundary layer
Weight density ρ, kg/m^3	8,910	6,910	7,910
Heat conductivity λ, W/(mK)	361 (293 K) 337 (573 K) 312 (783 K) 286 (1,173 K)	20.0 (293 K) 19.3 (573 K) 18.5 (783 K) 17.7 (1,173 K)	37.9 (293 K) 36.5 (573 K) 34.9 (783 K) 33.3 (1,173 K)
Specific heat c, J/(kgK)	394 (293 K) 416 (573 K) 440 (783 K) 464 (1,173 K)	491 (293 K) 576 (573 K) 666 (783 K) 756 (1,173 K)	443 (293 K) 496 (573 K) 553 (783 K) 610 (1,173 K)

$$\delta=\sum\left(\left|\Delta T_A-\Delta T_T\right|/T_T\right)/D \tag{8}$$

Where, ΔT_A is the analytical temperature rise [K], ΔT_T is the measured average temperature rise [K], T_T is the measured average temperature [K], and D is the number of data.

Figure 8 shows the analysis errors for the four types of wear mode and the average error for all the types of wear mode when η is

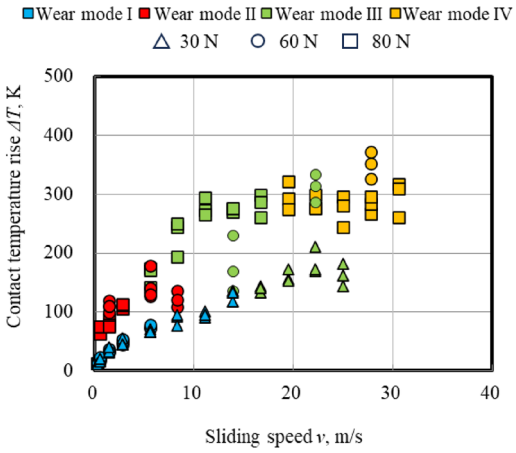

(a) Analysis result (η=0.6)

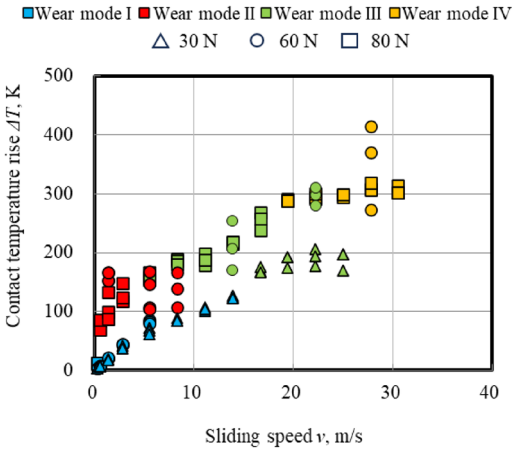

(b) Experimental result

Fig. 7 Relationship between sliding speed and contact temperature rise (analysis and experimental result)

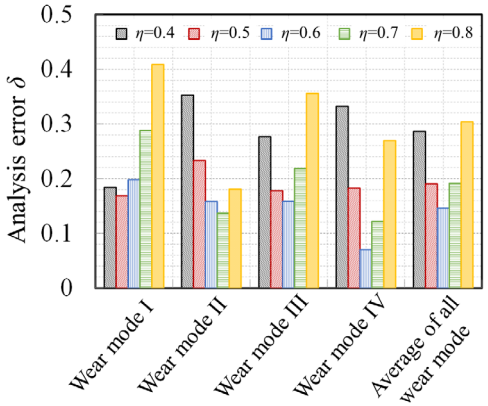

Fig. 8 Analysis error

varied from 0.4 to 0.8. This figure shows that the average error is smallest when η is 0.6, and the value of η at which the analysis error is smallest varies depending on the wear mode. The reason for this variation is that unconsidered factors not considered in the analysis model, such as softening of material and formation of an alloy layer at the contact boundary, may affect the temperature rise.

3.3 Occurrence mechanism of wear mode II

To estimate the number of contacts from experimental and analysis results, it is necessary to apply a relationship between friction, taking into account the number of contacts, and the contact temperature rise. The authors assumed the contacts to be a semi-infinite solid as shown in Fig. 9 and supplied the heat flux q_0 [W/m^2] to the contact surface ($x = 0$). In the thermal conduction theory [15], the temperature $T_{x,t}$ [K] at the distance from contact surface x [m] after the contact time t [s] is calculated by (9).

$$\frac{\lambda\left(T_{x,t}-T_{\mathrm{i}}\right)}{q_0\sqrt{\alpha t}}=\frac{2}{\sqrt{\pi}}\exp\left(-\frac{x^2}{4\alpha t}\right)-\frac{x}{\sqrt{\alpha t}}\mathrm{erfc}\left(\frac{x}{2\sqrt{\alpha t}}\right) \tag{9}$$

Where, T_{i} is the initial temperature [K], α is the thermal diffusivity [m^2/s]. The heat flux supplied to one contact spot is calculated by (10).

$$q_0=\beta\eta\frac{\mu N v}{n\pi r_{\mathrm{a}}^2} \tag{10}$$

Where, β is the heat distribution rate. Since the analysis result shown in Fig. 7 (a) is the temperature in the boundary layer, which means contact surface, the surface temperature $T_{0,t}$ [K] and the temperature rise $\Delta T_{0,t}$ [K] of the solid are calculated by (11) and (12) as $x = 0$.

$$T_{0,t}=T_{\mathrm{i}}+\frac{2\sqrt{\alpha t}}{\lambda\sqrt{\pi}}\beta\eta\frac{\mu N v}{n\pi r_{\mathrm{a}}^2} \tag{11}$$

$$\Delta T_{0,t}=T_{0,t}-T_{\mathrm{i}}=\frac{2\eta\beta\sqrt{\alpha}}{\pi r_{\mathrm{a}}^2\lambda\sqrt{\pi}}\frac{\mu N v}{n}\sqrt{t}=C\frac{\mu N v}{n}=CE \tag{12}$$

Since the material properties and the radius of real contact area are constant, the temperature rise is proportional to the work done by friction and square root of the contact time per contact spot. Therefore, the authors define the variable in (12) as E [W/s$^{-0.5}$].

Figure 10 shows the analyzed temperature rise obtained by converting the horizontal axis of Fig. 7 (a) into E. From Fig. 10, it is confirmed that the coefficient of determination is 0.9999, so that the proposed analysis model shown in Fig. 6 satisfies (12). Figure 11 shows the measured temperature rise in wear mode I and II obtained by converting the horizontal axis of Fig. 7 (b) into E and approximate curve of Fig. 10. From Fig. 11, it is found that measured temperature rise in the wear mode I is generally proportional to E, but in the wear mode II it is not proportional to E and some data exceed the approximate curve.

The reason why the temperature rise in the wear mode II exceeds the approximate curve is thought to be because C and E in the experiment are greater than those in the analysis. The factors that increase C and E are as follows:

(a) The number of contacts n in the experiment was lower than that estimated by (6) in the analysis model, so that E was greater than it was in the analysis model. Previously, it has been proposed that the transition to the seizure wear mode under unlubricated conditions is caused by a reduction in the number of contacts due to wear particles and uneven contact [13].

(b) The real contact area πr_{a}^2 in the experiment was smaller than in the analysis model, so that C was greater than it was in the analysis model. On the other hand, it has been reported that the real contact area increases in the seizure wear mode [13], so it is unlikely that the real contact area decreased in this experi-

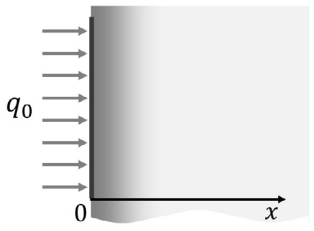

Fig. 9 Semi-infinite solid model for heat conduction calculation

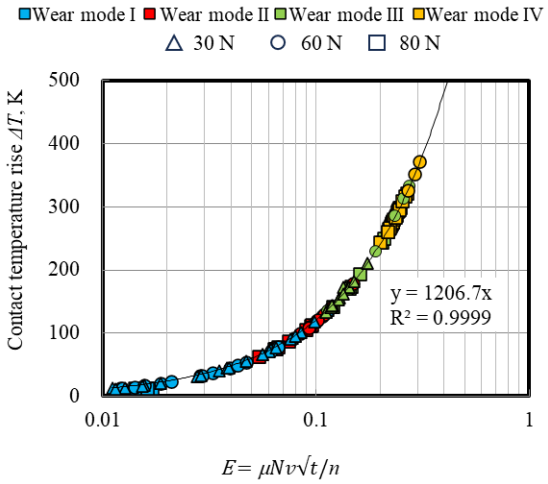

Fig. 10 Analytical relationship between temperature rise and friction, taking into account number of contacts and contact time (Analysis result: η = 0.6)

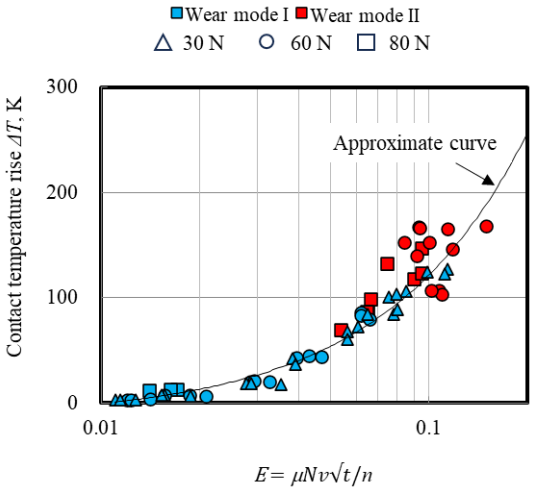

Fig. 11 Experimental relationship between temperature rise and friction, taking into account number of contacts and contact time (Experimental result: wear mode I and II)

ment.

(c) The heat conversion rate η in the experiment was greater than the 0.6 in the analysis model, so that C was greater than it was in analysis model. As mentioned in section 2.2, stick-slip occurred during the wear mode II test. Since friction noise and vibration due to stick-slip were significantly higher, the heat conversion rate might lower than in other wear modes. Additionally, even if the heat conversion rate differs according to wear mode, the temperature rise must be proportional to another approximate curve, but the measured temperature rise in wear mode I is not proportional to E. Therefore, it is unlikely that the heat conversion rate increased in this experiment.

(d) The contact time t in the experiment was greater than that in the analysis model, so that E was greater than it was in the analysis model. According to (7), the factor that increases the contact time is the increase in the radius of the contact spot r_a. However, as the radius of the contact spot increases, the heat flux supplied to the contact surface decreases, so the temperature rise must decrease. It is therefore unlikely the contact time increased in this experiment.

From the above, it can be assumed that the reduction in the number of contacts is the most influential factor.

The number of contacts in the experiment can be calculated using the approximated relationship between the temperature rise and E. From the approximation and the temperature rise curve ΔT_T in Fig. 11, the number of contacts in the experiment n_T is calculated by (13).

$$n_T = 1206.7 \frac{\mu N v \sqrt{t}}{\Delta T_T} \tag{13}$$

Figure 12 shows the number of contacts calculated using (13), and Fig.13 shows the contact pressure per contact. These figures indicate that the number of contacts in wear mode II is less than that in wear mode I, as expected above, and that the contact pressure boundary between the wear mode I and II is approximately 900 MPa, which is similar to the hardness of the copper plate, 980 MPa. According to the Goddard's report [10], the condition for the occurrence of the seizure wear mode is expressed by (14).

$$\frac{N}{n_T \pi r_a^2} = H \tag{14}$$

Here, H is a hardness [Pa]. This equation shows that if the contact pressure exceeds the hardness of material, plastic flow occurs rapidly around the contact spot, causing the seizure.

Based on the above considerations, the wear mode II is classified as the seizure wear mode. It is assumed that if the seizure occurs between the copper plate and the contact strip, crack will occur inside the contact point of the copper plate. It is also thought that seizure at the contact point is released by the softening of the copper plate regardless of the sliding speed. Since the softening occurs due to the friction force and sliding speed, the friction force decreases as the sliding speed increases in this mode. This is the reason why the friction coefficient in wear mode II decreases as the sliding speed increases in Fig.4.

In this study, the authors classified the mechanical wear mode, which had previously been considered to be solely the adhesive wear, into four types based on the material softening. The transition mechanism of wear modes due to material softening is universal and can be applied to different equipment, so that the wear phenomena caused in an actual railway field can be explained using this study. In actual railway field, it is thought that differences in the wear rate and the wear surface of the contact wire lead to the occurrence of different wear modes. Since the wear mechanism differs according to wear mode, this knowledge will be useful for considering fundamental measures for wear reduction.

4. Conclusions

In this study, the authors carried out wear tests with a new rotary wear tester, which can measure the contact temperature, and analyzed the contact temperature with the new contact model, taking into account the number of contacts. From the test and analysis results, the authors classified wear modes into four types and clarified the conditions under which each mode occurs. The results obtained in this study are as follows:

(1) The wear modes under the material combinations of the hard-drawn copper plate and the iron-sintered alloy contact strip are classified into four types as follows:
Wear mode I: Adhesive wear mode
Wear mode II: Seizure wear mode
Wear mode III: Abrasive wear mode
Wear mode IV: Soften and flow wear mode

(2) The conditions of occurrence of each wear mode are clarified based on the softening of materials due to frictional heat as follows:
Wear mode I, II: Neither material is softened.
Wear mode III: Only copper plate is softened.

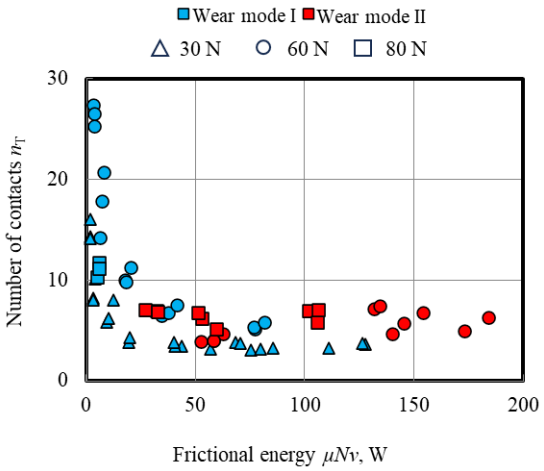

Fig. 12 Estimated number of contacts

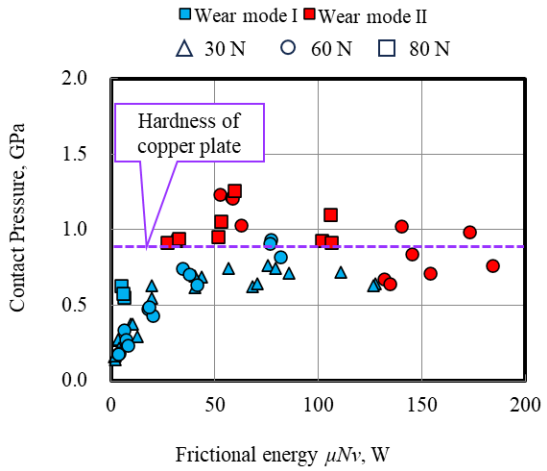

Fig. 13 Estimated contact pressure

Wear mode IV: Both materials are softened.

(3) Heat transfer analysis taking into account the number of contacts revealed a mechanism of occurrence of wear mode II, which is caused by the surface pressure at the real contact point exceeding the hardness of the copper.

(This paper is the updated version of the reference [16] [17])

References

[1] Iwase, M., "Current Collecting by the Pantograph and its Wear (III)," *Railway Technical Research Report*, Vol. 217, 1961 (in Japanese).

[2] Kohno, A., Ohyabu, H. and Soda N., "Effect of Discontact Arc on Wear of Materials for Current Collection (Part 1)," *Journal of Japan Society of Lubrication Engineers*, Vol. 27, No. 4, pp. 283-287, 1982 (in Japanese).

[3] Kohno, A., Ohyabu, H. and Soda N., "Effect of Discontact Arc on Wear of Materials for Current Collection (Part 2)," *Journal of Japan Society of Lubrication Engineers*, Vol. 27, No. 7, pp. 527-532, 1982 (in Japanese).

[4] Jia, S. G., Liu, P., Ren, F. Z., Tian, B. H., Zheng, M. S., Zhou, G. S., "Sliding wear behavior of copper alloy contact wire against copper-based strip for high-speed electrified railways," *Wear*, Vol. 262, No. 7-8, pp. 772-777, 2007.

[5] Yamashita, C., Adachi, K., "Influence of Current on Wear Modes and Transition Condition of Current Collecting Materials," *Journal of Japanese Society of Tribologist*, Vol. 58, No. 7, pp. 496-503, 2013 (in Japanese).

[6] Yamashita, C., Adachi, K., "Wear Mode Map of Current Collecting Materials," *Journal of Japanese Society of Tribologist*, Vol. 62, No. 2, pp. 129-136, 2017 (in Japanese).

[7] Hirata, T., Tanaka, M., Kumano, H., Hada, Y., *Illustrated Energy Engineering*, Morikita Publishing Inc., pp. 173-174, 2011 (in Japanese).

[8] Sasaki, S., *Elucidation and Control of Tribology by numerical Simulation and Surface Analysis*, Technosystem, pp. 47-56, 2018 (in Japanese).

[9] Mizumoto, M., Usami, K., "Why does wear occur," *Turbomachinery*, Vol. 24, No. 5, pp. 267-273, 1996 (in Japanese).

[10] Goddard, J., Wilman, H., "A theory of friction and wear during the abrasion of metals," *Wear*, Vol. 5, No. 2, pp. 114-135, 1962.

[11] Suh, N. P., "The delamination theory of wear," *Wear*, Vol. 25, pp. 111-124, 1973.

[12] Ashby, M. F., Lim, S. C., "Wear-mechanism Maps," *Acta metal*, Vol. 35, No. 1, pp. 1-24, 1987.

[13] Sasada, T., *Wear*, Yokendo, 2008 (in Japanese).

[14] Nemoto, K., Yamashita, C., "Elucidation of Transition Mechanism of Adhesive Wear Mode and Seizure Wear Mode between Copper Plate and Iron Based Sintered Alloy Contact Strip by Analysis of Contact Temperature," *Journal of Japanese Society of Tribologist*, Vol. 69, No. 4, pp. 301-311, 2024 (in Japanese).

[15] The Japan Society of Mechanical Engineers, *Heat Transfer Engineering*, Maruzen Publishing Inc., 2005 (in Japanese).

[16] Yamashita, C., Nemoto, K., "Classification of Mechanical Wear Mode of Contact Wire and Contact Strip caused by Frictional Heat," *RTRI Report*, Vol. 35, No. 12, pp. 11-16, 2021 (in Japanese).

[17] Nemoto, K., Yamashita, C., "Transition Mechanism between Adhesive Wear Mode and Seizure Wear Mode of Current Collecting Materials," *RTRI Report*, Vol. 38, No. 10, pp. 23-30, 2024 (in Japanese).

Authors

Chikara YAMASHITA, Ph.D.
Senior Chief Researcher, Head of Current Collection Maintenance Laboratory, Power Supply Technology Division
Research Areas: Overhead Contact Line, Tribology, Electric Contact, Fatigue

Koki NEMOTO
Researcher, Current Collection Maintenance Laboratory, Power Supply Technology Division
Research Areas: Overhead Contact Line, Tribology

Development of Non-loosening Rail Fastening System with Leaf Spring Clip Applicable to Existing PC Sleeper

Daiki YAMAOKA
Track Structures and Components Laboratory, Track Technology Division

Tadashi DESHIMARU
Rail Maintenance and Welding Laboratory, Track Technology Division

Shingo TAMAGAWA
Track Structures and Components Laboratory, Track Technology Division

Rail fastening systems using bolts and leaf spring clips are widely used in Japan. This rail fastening system requires regular maintenance to prevent the bolts from loosening. To eliminate the need for retightening bolts, some railway companies are replacing rail fastening systems using leaf spring clips with boltless rail fastening systems using round bar clips. This replacement involves replacing the existing PC sleepers with another type of sleepers for round bar clips. Therefore, some railway companies find it difficult to introduce boltless rail fastening systems using round bar spring clips due to construction costs and labor. In response to this problem, we have developed non-loosening rail fastening systems using leaf spring clips that are compatible with existing PC sleepers.

***Key words*:** *rail fastening system, leaf spring clips, non-loosening bolt, PC sleeper, washer*

1. Introduction

Rail fastening systems currently used in Japan generally use a method in which rail clips are deflected by bolts to fasten the rails. This rail fastening system uses leaf spring clips made from processed spring steel plates. Figure 1 shows an example of this type of rail fastening system, specifically the commonly used 5N-type rail fastening system (for 3-type PC sleepers and JIS 50kgN-rails applied to conventional lines) in Japan. This rail fastening system requires periodic monitoring of bolt loosening to maintain the rail clamping force. If loosening is detected, retightening must be performed based on indicators such as tightening torque.

In contrast, rail fastening systems that do not require bolt retightening are referred to as boltless rail fastening systems. Figure 2 shows an example of a boltless rail fastening system, specifically the e2009 type which is widely used in Japan. This rail fastening system utilizes wire spring clips made from processed spring steel. The rails are fastened by inserting the wire spring clips into the shoulder embedded in the PC sleepers by a specific tool. Therefore, replacing the rail fastening system with bolts and leaf spring clips with the boltless rail fastening system eliminates the need to retighten the bolts. However, this requires the existing PC sleepers to be replaced with PC sleepers compatible with wire spring clips. As a result, some railway operators face difficulties in introducing boltless rail fastening systems from the viewpoint of the associated costs. Therefore, in this study, we developed a non-loosening rail fastening system using leaf spring clips that can utilize the structure of the existing PC sleepers without removal [1, 2].

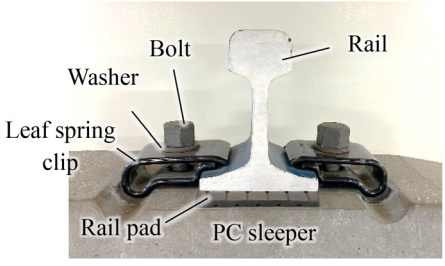

Fig. 1 Rail fastening system using leaf spring clips and bolts (5N-type)

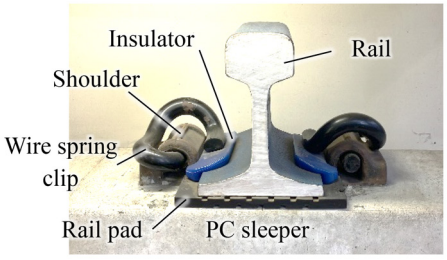

Fig. 2 Boltless rail fastening system using wire spring clips (e2009 type)

2. Structural consideration for the non-loosening rail fastening system

2.1 Requirements of the rail fastening system

The 5N-type rail fastening system mentioned above was selected as the application for the boltless rail fastening system. The requirements for examining the structure of this rail fastening system are as follows:

- The structure of existing PC sleepers can be utilized
- Easy installation on existing PC sleepers
- No loosening of the components after rail fastening

2.2 Structural proposal

We devised the structure shown in Fig. 3, based on the total

number of components, ease of manufacturing, and material strength. The components consist of leaf spring clips, bolts and washers. This structure is designed to fasten the rail by adhering bolts to the plugs embedded in the PC sleeper, placing a leaf spring clip on top of the sleeper, and inserting a washer between the bolt and the leaf spring clip.

2.3 Prototype of structural components

Based on the structure devised in the previous section, the leaf spring clip, bolt and washer were prototyped, as shown in Fig. 4. The cross section of the leaf spring clip was designed identical to that of the leaf spring clip consisting of the 5N-type rail fastening system. The circular hole in the leaf spring clip was made larger than the bolt head so that it can be fitted after the bolt adheres to the PC sleeper. Additionally, the tip of the upper spring section of the leaf spring clip was shortened to prevent it from contacting the rail. This ensured that the tip of the upper and lower spring sections make contact after rail fastening. The washer was shaped in a U-configuration to be inserted between the bolt and the leaf spring clip. The bolt was designed with stepped sections of different diameters, not to be inserted above the stepped section. This ensures that the distance from the underhead of the bolt to the top of the sleeper remains constant. The distance from the underhead of the bolt to the stepped section of the bolt was set at 51 mm ± 0.5 mm, including the permissible dimensional tolerance during manufacturing.

2.4 Rail fastening process

Figure 5 shows a diagram of the rail fastening process. Each step in the figure is specifically as follows:

1) Bend the leaf spring clip to make the upper and lower spring sections contact.
2) Place the washer in the gap between the bolt and the leaf spring clip.
3) Release the bending force applied to the leaf spring clip and allow it to clamp the washer between the bolt and the spring, thereby fastening the rail.

Following the process, it was confirmed that the rail could be fastened as shown in Fig. 6 without applying significant load on the bolt.

2.5 Rail clamping force

It is a concern that the rail clamping force of the developed rail fastening system may be less than that of the 5N-type rail fastening system. Therefore, this section examines the rail clamping force of the developed rail fastening system.

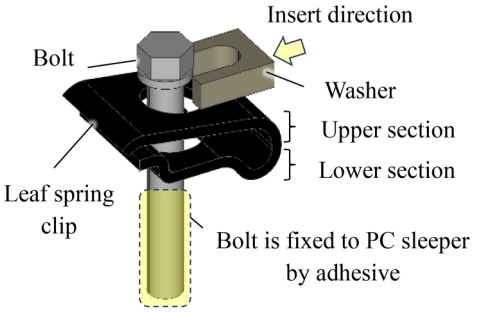

Fig. 3 Proposed structure of rail fastening system

The following equation expresses the relationship between the rail clamping force and the rail creep resistance. [3]:

$$\gamma = 2P\mu_1 + 2P\mu_2 \quad (1)$$

Where γ is the rail creep resistance per set of rail fastening systems (kN), P is the clamping force per leaf spring clip (kN), μ_1 is

Fig. 4 Components of the proposed rail fastening system

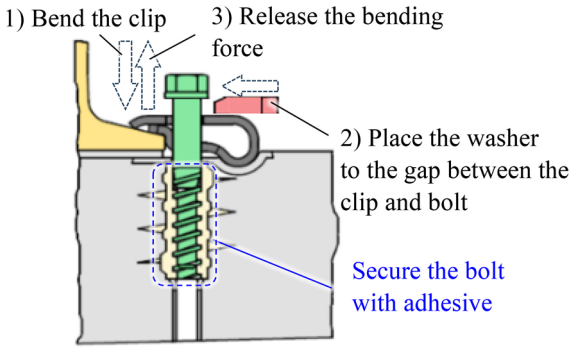

Fig. 5 Rail fastening process

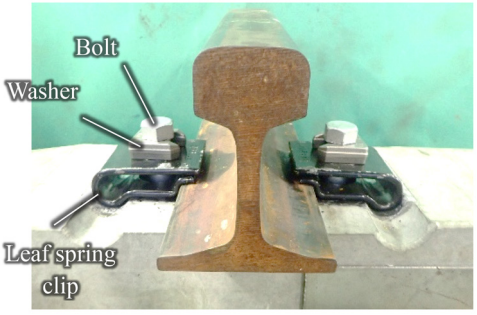

Fig. 6 Assembled rail fastening system

the coefficient of friction between rails and leaf spring clip, and μ_2 is the coefficient of friction between rail and rail pad.

The rail creep resistance of the rail fastening system for ballast tracks must generally exceed the standard values for longitudinal ballast resistance, which range from 6 to 10 kN/m [3]. Therefore, in order to achieve a rail creep resistance greater than 10 kN/m, the required rail clamping force per leaf spring clip P is estimated to be 3.56 kN, calculated from equation (1) with a sleeper spacing of 641 mm, $\mu_1 = 0.25$ [4], $\mu_2 = 0.65$ [4].

A linear elastic FEM analysis was conducted using NX Nastran ver. 10.0 to determine the rail clamping force of the developed rail fastening system. Figure 7 shows the analysis model of the leaf spring clip. In this model, the bolt axial force is assumed to act vertically downwards at the center of the upper spring section of the leaf spring clip. As a reaction force, the rail clamping force is generated at the tip of the lower spring section, and the remaining reaction force is generated at the rear end of the lower spring section. The clearance at the tip of the leaf spring clip before fastening is set to 9 mm and the contact between the upper and lower spring sections is not considered. The deflection of the leaf spring clip is the value at the tip of the upper spring section and at the point of application of the bolt axial force.

Figure 8 shows the relationship between the deflection of the leaf spring clip and the rail clamping force obtained from the FEM analysis. When the upper and lower spring sections make contact, the rail clamping force is 4.08 kN, which exceeds the required rail clamping force of 3.56 kN mentioned above. Additionally, at the rail clamping force of 4.08 kN, the deflection at the point of application of the bolt axial force is 3.97 mm, and at the required rail clamping force of 3.56 kN, the deflection is 3.46 mm. In this case, the difference in deflection at the point of application of the bolt axial force is 0.51 mm. On the other hand, the distance from the underhead of the bolt to the stepped section of the bolt is set with a tolerance of ± 0.5 mm for the permissible dimensional tolerance when manufacturing. Since the deflection at the point of application of the bolt axial force in the leaf spring clip is within a ± 0.5 mm tolerance, when deflected to contact the upper and lower spring sections, it can be concluded that the design ensures that the required rail clamping force is achieved.

3. Performance tests

To evaluate the performance of the prototype, we conducted a tip spring constant test and a two-directional loading test to verify the safety of the rail fastening system against fatigue failure. In addition to these tests, we performed a creep resistance test.

3.1 Tip spring constant test

A tip spring constant test was conducted to assess the rail clamping force, and to determine the tip spring constant, which represents the vertical spring constant at the tip of the leaf spring clip. Figures 9 and 10 show the setup of the tip spring constant test, and the test results, respectively. In this test, the actuator was fixed to the test rail head, and the rail pad was removed by lifting the rail. Subsequently, repeated vertical load was applied. The sign of the rail displacement was defined as positive for upward movement and negative for downward movement. The tip spring constant and rail clamping force were determined based on the relationship between the load and rail displacement during rail lifting. As a result, the tip spring constant converted to per leaf spring clip was 1.0 MN/m. In addition, the rail clamping force converted to per leaf spring clip was 4.10 kN, which was generally in agreement with the results of the FEM analysis conducted in Section 2.5.

3.2 Two-directional load test

As well as the tip spring constant and rail clamping force obtained from the test in section 3.1, based on the design loads and track conditions shown in Table 1, using the loading conditions for the two-directional load test were calculated [5] as shown in Table 2, the test was conducted. In this test, the bolts were fixed to the PC sleepers using an epoxy resin-based adhesive.

Figure 11 shows the setup of the two-directional load tests. First, a static load test was conducted using two actuators to apply static alternating loads to the rail from inside and outside the track gauge to measure the leaf spring clip stress and the lateral rail head displacement. Then, a dynamic load test was performed to check for any abnormalities in the components when the two actuators applied alternating dynamic loads to the rail. Figure 12 shows leaf spring clip stress obtained from the static load test, plotted on the fatigue limit diagram of SUP9 steel. The leaf spring clip stress was within the Goodman line for 10^5 cycles and yield limit line, so there was no problem to solve. Additionally, the displacement of the lateral rail head was approximately 0.5 mm, which was less than the design limit of 7.0 mm for conventional railway lines.

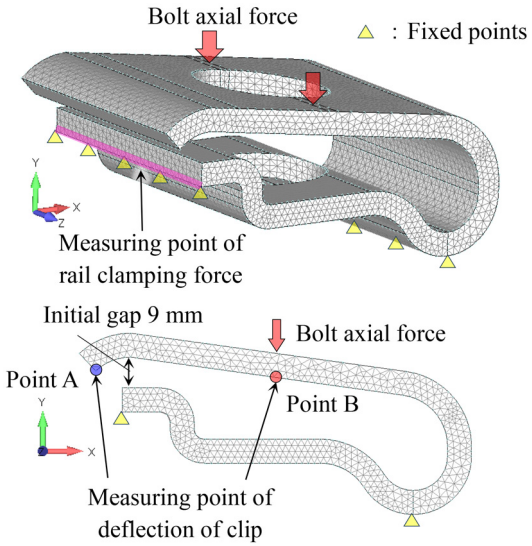

Fig. 7 Analysis model of leaf spring clip

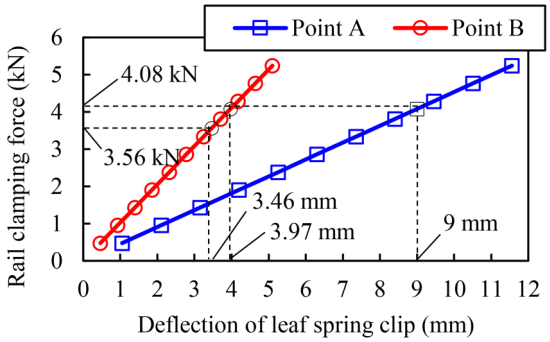

Fig. 8 Relationship between rail clamping force and deflection of leaf spring clip

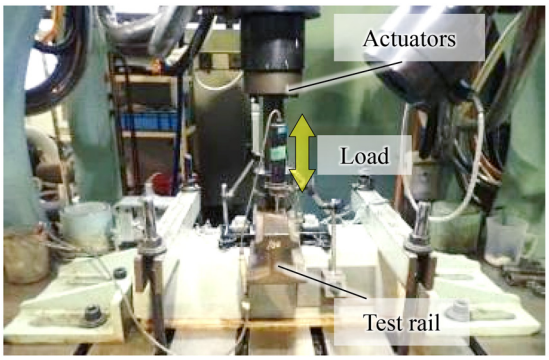

Fig. 9 Setup of tip spring constant test

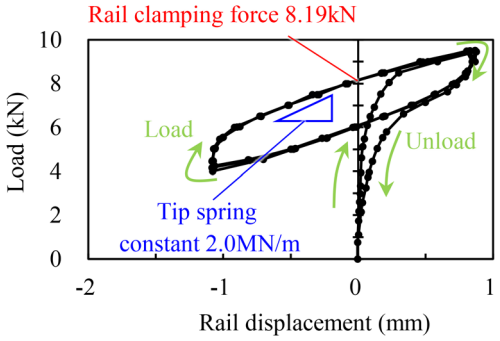

Fig. 10 Result of tip spring constant test

Table 1 Design loads and track conditions

Design wheel load	Load A (kN)	98
	Load B (kN)	86
Design lateral load	Load A (kN)	30
	Load B (kN)	15
Sleeper span (mm)		641
Vertical coefficient of rail pad (MN/m)		110
Vertical coefficient under sleeper (MN/m)		40
Lateral coefficient of rail fastening system (MN/m)		90

Table 2 Loading conditions

Test load P_A	Max. value (kN)	34.2
	Min. value (kN)	10.0
Loading angle θ_A (°)		58.7
Test load P_B	Max. value (kN)	27.7
	Min. value (kN)	10.0
Loading angle θ_B (°)		67.1
Height of load application h (mm)		100

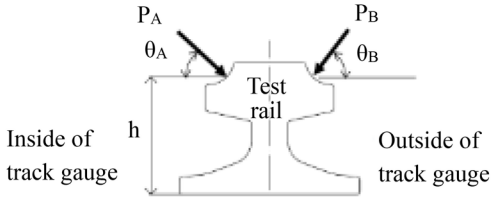

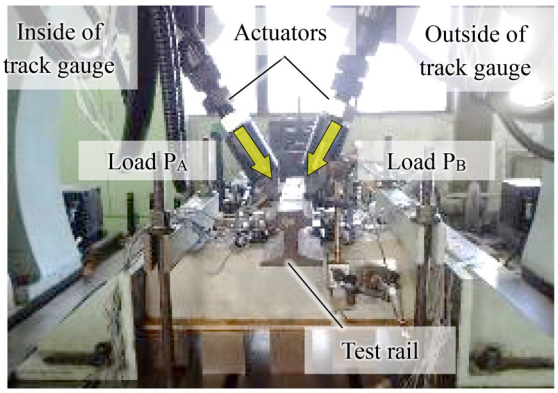

Fig. 11 Setup of two-directional load test

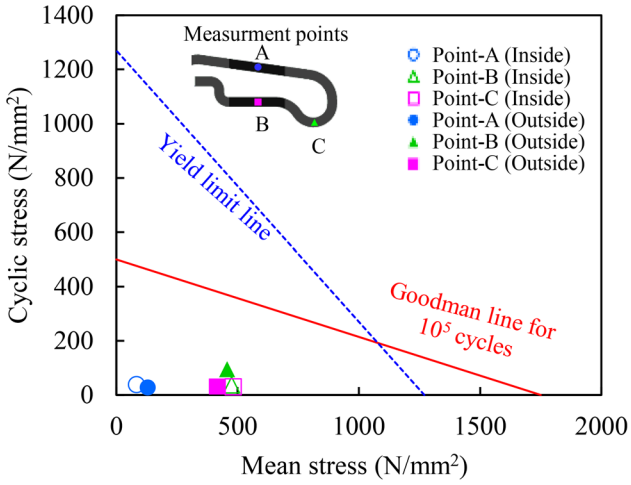

Fig. 12 Stress of leaf spring clip obtained from the static load test

The dynamic load test was conducted for 1 million cycles at a loading frequency of 5.5 Hz. As a result, no loosening or displacement of the washers was observed after the test, and no abnormalities were found in the components.

3.3 Rail creep resistance test

Figure 13 shows the setup of the rail creep resistance test. In this test, the PC sleeper was fixed to the test machine table, and the rail was loaded twice in its longitudinal direction to measure the rail creep resistance. Figure 14 shows the test results. The rail creep resistance averaged 7.78 kN per rail fastening system over two loadings. Converted to a sleeper spacing of 641 mm, this is equivalent to 12.1 kN/m, exceeding the ballast longitudinal resistance of 10 kN/m.

4. Development of installation tool

To implement the proposed rail fastening method, a tool with a mechanism for bending the leaf spring clip is required. For the purpose, two types of installation tools were developed, a manual installation tool and a mechanical installation tool as shown in Fig. 15. The manual installation method is a tool that bends the leaf spring clip by hand without the use of electric machinery. This method

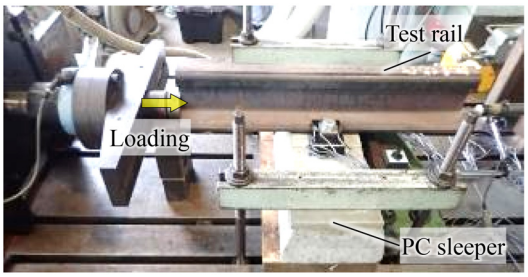

Fig. 13 Setup of rail creep resistance test

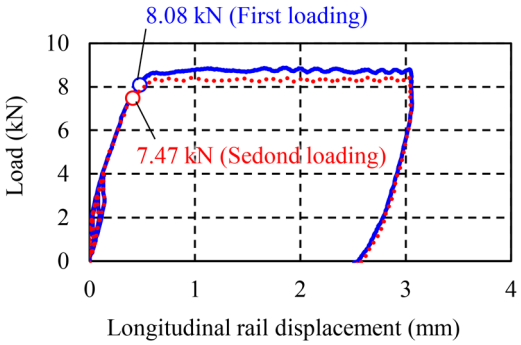

Fig. 14 Result of rail creep resistance test

utilizes the principle of leverage, where the reaction force is taken from the rail, and the leaf spring clip is bended at the tip of the arm by tilting the arm. The mechanical installation method is a tool that bends the leaf spring clip using an electric wrench or similar device. It operates by taking the reaction force through two plates attached to the bottom of the tool and placed against the rail's underside. The hexagonal section at the top of the tool is connected to a standard maintenance wrench or similar tool and rotated to bend the leaf spring clip. Using these two types of installation tools, we conducted a workability evaluation. As a result, both tools were confirmed to effectively bend the leaf spring clip, allowing the upper spring section to be tightly pressed against the lower spring section. In addition, it was verified that the fastening washer could be installed properly in the gap between the bolt and the leaf spring clip in this state.

5. Test installation on an operational line

A test installation was conducted on an operational line to verify the performance of the developed rail fastening system under actual installation conditions. A straight section of a conventional railway line was selected as the installation site. Figure 16 shows the installation process using the manual installation tool. The developed rail fastening systems were installed on five sleepers, with one sleeper skipped between each installation, totalling ten sets of rail fastening systems. The installation was carried out following the rail fastening process described in Section 2.4 using the manual installation tool. As shown in Fig. 17, it was confirmed that the rail fastening system could be successfully installed on the operational line without any issues.

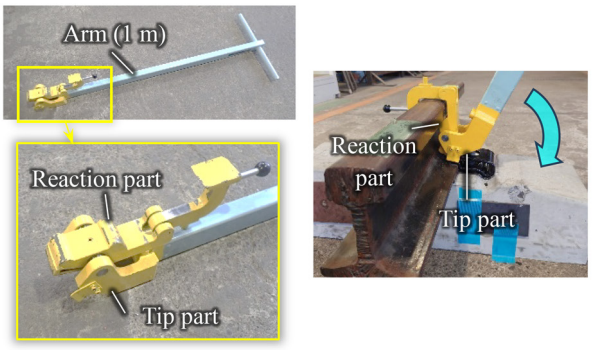

(a) Manual tool

(b) Mechanical tool

Fig. 15 Installation tools

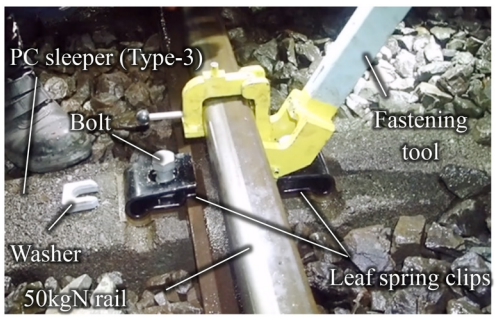

Fig. 16 Situation of installation on an operational line

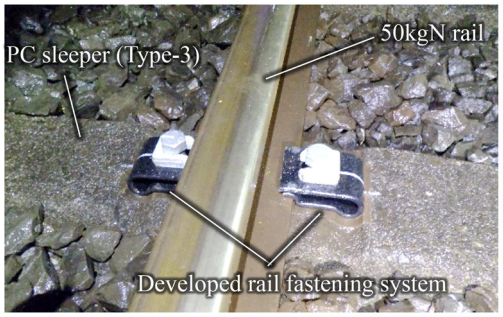

Fig. 17 Condition after installation

6. Conclusion

A non-loosening rail fastening system with leaf spring clips was developed that does not require the replacement of PC sleepers and utilizes their existing structure. Performance tests confirmed that the fastening system possesses the necessary performance for application on actual tracks. In addition to the fastening system, two types of installation tools were developed to facilitate rail fastening, and their workability was verified.

In this rail fastening system, even with the smooth shape of the upper surface of the washer and the bolt neck, no detachment or movement of the washer was observed during a dynamic load test. However, for mass production, a spherical surface processing is planned for the washer and bolt to ensure that they do not prevent detachment or movement. Additionally, after the test installation on the operational line, ongoing monitoring will be conducted, including durability testing of the adhesive, and further improvements will be made as necessary.

Acknowledgment

In conducting the field installation tests for this research, we received significant cooperation from the West Japan Railway Company. We would like to express our sincere gratitude to them here.

References

[1] Yamaoka, D., Deshimaru, T. and Tamagawa, S., "Development of non-loosening rail fastening system with leaf spring clip," *Japan Society of Civil Engineers 2024 Annual Meeting*, VI-696, 2024 (in Japanese).

[2] Yamaoka, D., Deshimaru, T., Tamagawa, S. and Sato, H., "Development of non-screw plate-shaped spring clip rail fastening system," *Shinsenro*, Vol. 78, No. 7, pp. 26-28, 2024 (in Japanese).

[3] supervised by Ministry of Land, Infrastructure, Transport and Tourism, *Design Standards for Railway Structures and Commentary (Track Structures)*, Maruzen, 2012 (in Japanese).

[4] Miyamoto, T. and Watanabe, K., "*Senro*," Sankaido, 1980 (in Japanese).

[5] Tamagawa, S., Kataoka, H. and Deshimaru, T., "Practical model for rail tilting and its application to performance test of rail fastening system," *Journal of JSCE*, Vol. 7, pp. 1-14, 2019.

Authors

Daiki YAMAOKA
Researcher, Track Structures and Components Laboratory, Track Technology Division
Research Areas: Continuous Welded Rail, Rail Fastening System

Tadashi DESHIMARU, Ph.D.
Senior Chief Researcher, Head of Rail Maintenance and Welding Laboratory, Track Technology Division
Research Areas: Railway Rails, Rail Fastening Systems

Shingo TAMAGAWA, Ph.D.
Senior Researcher, Track Structures and Components Laboratory, Track Technology Division
Research Areas: Continuous Welded Rail, Rail Fastening System

Rail Gas Pressure Welding with Short Upset Distance Using Variable Pressure Method

Hajime ITOH **Yuki KONAYA**
Rail Maintenance and Welding Laboratory, Track Technology Division

In order to reduce the bulge of gas pressure welding and finish by grinding only, the authors carried out rail gas pressure welding tests and numerical analysis to reduce the upset distance. In the tests, a new rail gas pressure welding method using a variable pressure method was achieved with a compression of the upset distance of about 6 mm, which is 1/4 of the conventional method, with sufficient strength for practical use. As the trimming process is not necessary, there is no need for a trimming device. This also reduces the weight of gas pressure rail welding machines.

Key words**:** *gas pressure welding, numerical analysis, weld strength, variable pressure method*

1. Introduction

Gas pressure welding (GPW) is a type of solid-state welding using a gas flame, and is a major rail welding method, accounting for about 40% of rail welding in Japan. Because of its high reliability and relatively good portability of equipment, GPW is the main welding method used for welding of rails arranged along the side of railway tracks. The welding principle of GPW is to achieve metallic bonding by breaking up and reducing the size of oxide inclusions in the weld interface by increasing the temperature due to heating by a gas flame from the outside of the component and the plastic deformation of the weld due to pressure applied in the axial direction. Figure 1 shows the process of GPW for rails. In GPW for rails, the excess weld metal generated by plastic deformation during GPW is trimmed with a special tool in the hot state immediately after welding, thereby reducing the amount of finishing work needed with a grinder.

(a) Grinding of end surface

(b) Setting of the GPW machine to rail

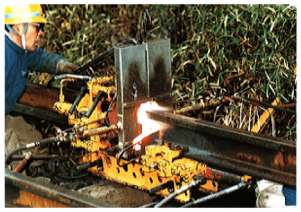

(c) Heating and pressing for rail

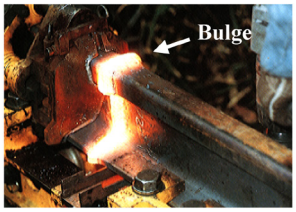

(d) Bulge of GPW after upsetting

(e) Trimming of the bulge

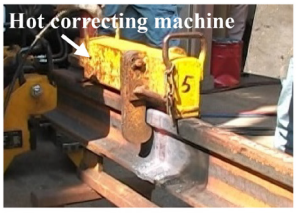

(f) Hot correcting

Fig. 1 Gas pressure welding (GPW) procedure for rail

However, this process requires heavy equipment such as a hydraulic pump and a tool (in the case of the TGP-H-A rail GPW machine, the total weight of the trimming tool is 145 kg) [1]. Therefore, to address the problem of a shrinking working population and reduce the labor intensity of this work, automation of various rail welding methods is required. However, simplification of these welding methods to achieve this, is a major challenge. As such, we tried to omit the trimming phase in this work by reducing the upset distance during rail GPW.

Previous studies have shown that the upset distance is a factor that significantly affects weld strength. A decrease in the upset distance is expected to result in a decrease in weld strength. On the other hand, a method that can increase the temperature of the weld interface while suppressing the oxidation of the weld interface has been proposed by using a variable pressure method that varies the applied pressure during GPW (a method in which compressive deformation is started early in the initial process at a high applied pressure and then the applied pressure is immediately reduced after the start of compressive deformation to suppress deformation and increase the temperature of the weld interface) [2]. Therefore, it is considered possible to increase the welding temperature and secure weld strength while suppressing the upset distance by applying this method.

On the basis of the above concept, we carried out GPW tests and numerical analyses using a constant pressure method and a variable pressure method and carried out performance evaluation tests on gas pressure welds with the low upset distance to assess their practical performance.

2. GPW test with low upset distance

2.1 Upset distance to exclude trimming operation

In order to determine the upset distance at which the finishing time with the grinder is equivalent to that under standard conditions, we carried out GPW tests on rails, with different upset distances and measured the finishing times. The upset distances are 6 mm and 10 mm without trimming and the standard condition of 24 mm (which includes trimming). Table 1 shows the finishing times measured at each upset distance. According to this, the finishing time under standard conditions is approximately 42 minutes. To achieve the same amount of work, the upset distance must be reduced to about 6 mm (finishing time of about 39 minutes). In order to develop a rail GPW method with a compression of around 6 mm, we produced rail gas

pressure welds with an upset distance of about 6 mm using the constant pressure method and the variable pressure method and evaluated the weld strength in slow bending tests.

Table 1 Comparison of finishing time

Upset distance (mm)	Finishing time (min)
6	39
10	59
24 (with trimming)	42

2.2 Preparation conditions for gas pressure welds using short upset distance

As a preliminary study, we carried out numerical analysis and GPW tests on rails with various pressure patterns. As a result, it was found that the early closure of the weld surfaces by high pressure in the initial heating phase and the promotion of interdiffusion of metal atoms by maintaining pressure and heating, contributed to the improvement of the welding condition.In this test we employ the variable pressure method as follows:

1. The initial applied pressure is set at 28 MPa and held until the upset distance reaches 1 mm.
2. After the upset distance reaches 1 mm, the hydraulic pump is stopped and heating and pressing is maintained by the residual pressure of the hydraulic cylinder.

The heating time was set to 420 s, which is the heating time of the standard condition (24 mm upset distance), to ensure that sufficient heat was applied. The resulting upset distance was approximately 6 mm.

Figure 2 shows examples of the results of measuring the applied pressure and upset distance, and Table 2 shows the GPW conditions under each condition.

A 0.75 m JIS 60 kg standard carbon rail was prepared for the tests and, a TGP-H-A type rail GPW machine was used. For the constant pressure method, the applied pressure was 22 MPa. The pressure was stopped when the upset distance reached 6 mm. The gas flow rates were 100 L/min oxygen and 110 L/min acetylene for all conditions. Two test welds were made under each condition, for a total of four welds. The trimming process was omitted, and the excess of weld metal was ground with a grinder. Note that an upset distance of 6 mm enables a 60% reduction in the volume of the excess weld metal compared to the standard condition. A magnetic particle test was carried out on the gas pressure welds and no defects were detected in any of them.

2.3 Slow bending test of gas pressure welds

Slow bending tests were carried out on the gas pressure welds by three-point bending with a central concentrated load between the fulcrums of 1 meter distance. The fracture positions were rail head-upward (HU) and rail head-downward (HD), and one of each was subjected to a slow bending test. Figure 3 shows the slow bending test results for each gas pressure weld. In both the HU and HD positions, the gas pressure welds with an upset distance of 6 mm using the constant pressure method barely met the threshold values for the breaking load and deflection of the gas pressure weld on JIS 60 kg standard carbon rail (HU: 1,400 kN-24 mm, HD: 1,250 kN-20 mm). However, all of the gas pressure welds with an upset distance of 6 mm using the variable pressure method exceeded the threshold values. Figure 4 shows the fracture surfaces for each condition in the HU position. Flat fracture surfaces were observed in the regions where tensile stresses act (HU: bottom region, HD: head region) in the gas pressure welds with an upset distance of 6 mm using the

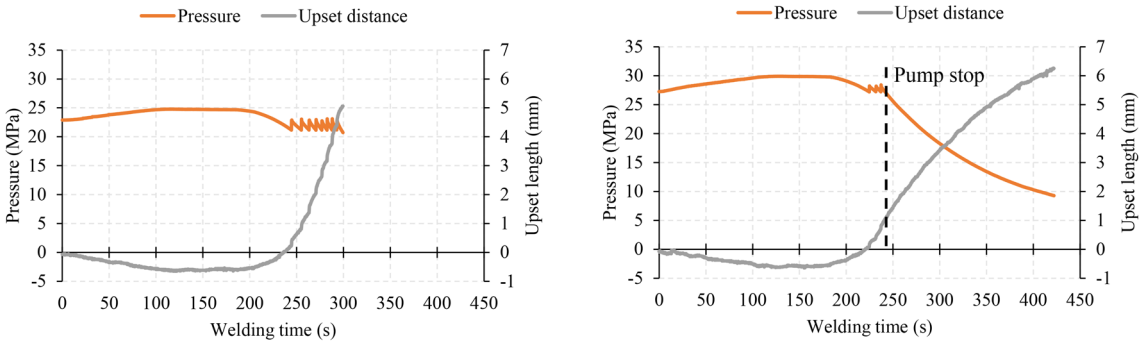

(a) Constant pressure pattern (b) Variable pressure pattern

Fig. 2 Examples of measurement results of pressure and upset distance

Table 2 GPW test conditions of low upset distance

No.	Pressure pattern	Initial pressure (MPa)	Initial upset distance (mm)	Heating time (s)	Total upset distance (mm)
1-1	Constant	22	—	310	6
1-2					
2-1	Variable	28	1	420	6
2-2					

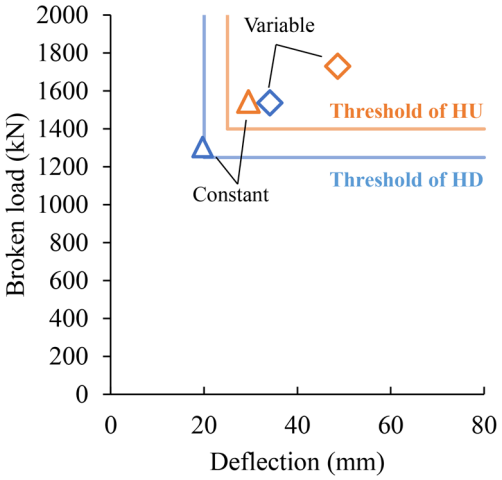

Fig. 3 Results of slow bending test

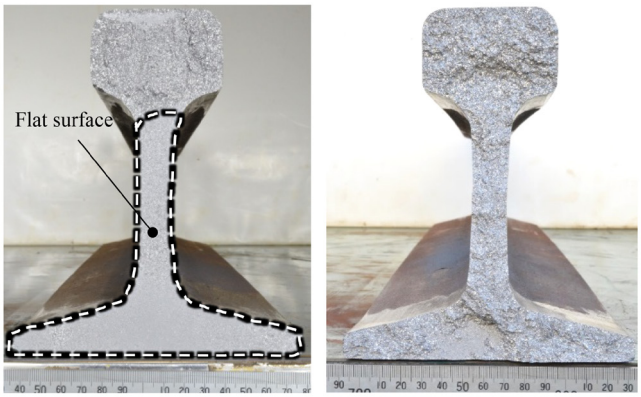

(a) Constant pressure (b) Variable pressure

Fig. 4 Fracture surface on HU position

constant-pressure method, but hardly any were observed in the gas pressure welds with an upset distance of 6 mm using the variable pressure method. The flat fracture surfaces are a mixture of cleavage fracture surfaces and dimpled fracture surfaces with fine inclusions, indicating that the fracture occurred at the weld interface. In the case of the fracture surface at the gas pressure welds with an upset distance of 24 mm, such a flat fracture surface rarely appears on the fracture surface, and in many cases a cleavage fracture surface is observed on the fracture surface.

The results above show that, at an upset distance of 6 mm, the application of the variable pressure method resulted in a strength that met the threshold value and no flat fracture surfaces.

3. Numerical analyses for rail GPW

3.1 Analysis model

In a previous study, we developed an analytical model for the heating and deformation of rail gas pressure welds, which accurately predicts the temperature distribution and deformation of rail gas pressure welds [3]. Here, the analytical model is used to evaluate the temperature and deformation at the weld interface of the rail gas pressure weld when the constant pressure method and the variable

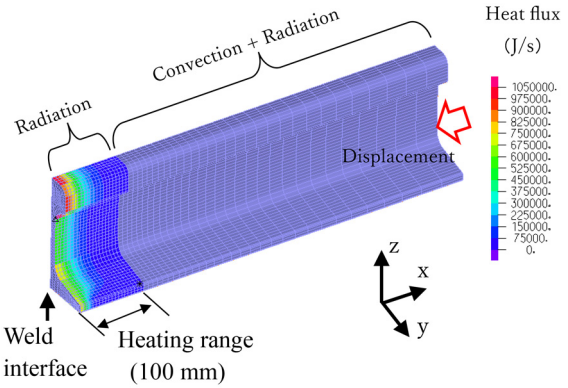

Fig. 5 Heat deformation analysis model

pressure method are applied. Figure 5 shows the analytical model used in this study. The analytical model was a quarter-symmetrical model centered on the weld interface of the rail gas pressure weld. Boundary conditions were set for the heat flux distribution due to the gas flame and radiation in the area defined as the heating range (100 mm longitudinally from the weld interface), and for the radiation and the atmospheric convection outside the heating range. Thermal conductivity properties and material constants were used to account for the temperature dependence. The mesh shape was hexahedral (27 nodes), with the heating range 100 mm longitudinally from the weld interface, divided by approximately 1 mm on each side. Solid-liquid phase transformation is not taken into account in this analytical model. In this model, the transition of the upset distance obtained during the GPW was set as the boundary condition at all nodes on the rail end face (opposite the weld interface), 750 mm away from the weld interface.

3.2 Analysis results

In this study, the equivalent plastic strain, which has been validated in previous studies, was used as an indicator of the degree of deformation on the weld interface of the rail gas pressure weld.

Figure 6 shows the temperature and equivalent plastic strain distributions on the weld interface and the central longitudinal section at an upset distance of 6 mm. The results of the analysis show that the temperature of each part is approximately 100°C higher in the variable pressure method (heating time 420 s) than in the constant pressure method (heating time 310 s), i.e. the temperature of the weld interface increased due to the longer heating time. In addition, the equivalent plastic strain increases in any part of the weld interface. The distribution of the equivalent plastic strain in the longitudinal direction shows that, compared to the constant pressure method, the area of strain is narrower and, the deformation is concentrated closer to the weld interface in the variable pressure method. In the results of previous studies on gas pressure welds of steel bars, it has been found that the temperature distribution affects the equivalent plastic strain distribution and that the higher the temperature gradient, the higher the equivalent plastic strain near the weld interface [4]. As shown in Fig. 6(a), it is assumed that the increase in the temperature gradient in the longitudinal direction due to the increase in the temperature of the weld interface results in concentration of deformation in the vicinity of the weld interface, which increases the equivalent plastic strain in the weld interface on the variable pressure method.

These results suggest that the application of the variable pressure method increased the temperature and deformation, which

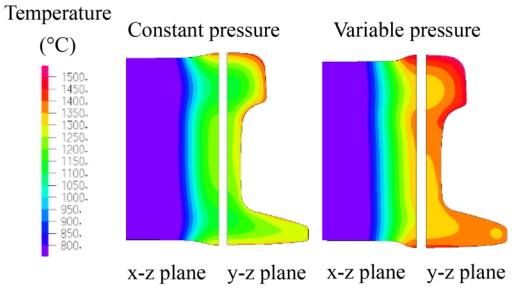

(a) Temperature of contour diagram for each pressure pattern

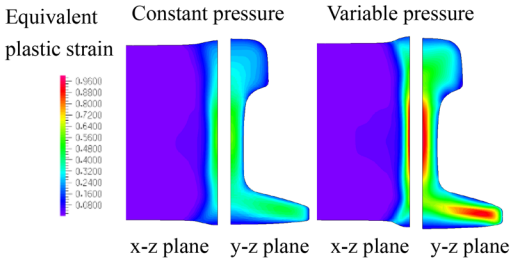

(b) Equivalent plastic strain of contour diagram for each pressure pattern

Fig. 6 Analysis result of temperature and plastic strain on the weld interface

promoted the breaking up and refining of the oxidized inclusions on the weld interface, resulting in improved weld quality.

4. Performance evaluation tests of rail gas pressure welds by variable pressure method

We carried out performance evaluation tests on rail gas pressure welds with 6mm upset distance using the variable pressure method. No defects were observed in any of the test welds by the magnetic particle test. The fracture positions were HU and HD postures, and two of each were carried out.

4.1 Slow bending test

Slow bending tests were carried out in the same way as in Chapter 2, with a concentrated load applied to the center of the distance between the fulcrums (1 m). Figure 7 shows the results of the slow bending tests. All welds met the threshold values for the breaking load and deflection of the gas pressure weld on JIS 60 kg standard carbon rail. As in Chapter 2, results showed that the fracture surfaces were good, with no welding defects or flat surfaces.

4.2 Hardness test on rail head

Brinell hardness (HB) was measured on the rail head surface to investigate the hardness distribution. The measurement area was 300 mm centered on the weld interface, with a measurement interval of 10 mm. Figure 8 shows the Brinell hardness distribution on the rail head surface of the rail gas pressure weld with 6 mm upset distance using the variable pressure method, together with the standard method. The hardness of the heat affected zone (hereinafter, referred to as HAZ), which is the area heated above the A1 transformation point (723°C), is slightly higher than that of the rail base metal, and a softened zone of about 10 mm width is observed at the boundary of the HAZ.

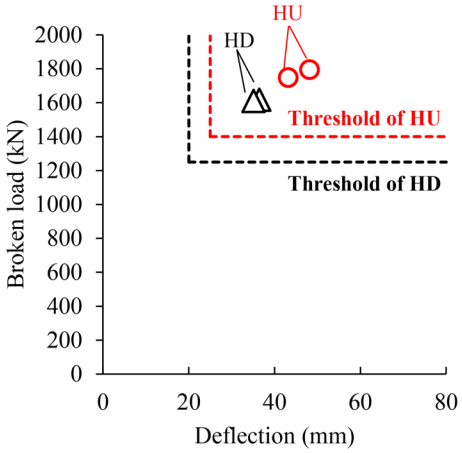

Fig. 7 Results of slow bending test

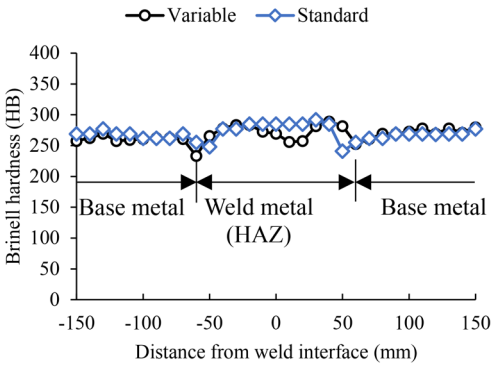

Fig. 8 Brinell hardness distribution on rail head surface

These are the same hardness distributions as those of the standard rail gas pressure welds and are not considered to cause problems such as localized indentations in practical use.

4.3 Bending fatigue test

Bending fatigue tests were carried out in the HU position with tensile stresses applied to the rail base. In order to evaluate the fatigue strength of the gas pressure welds including the HAZ, a four-point bending fatigue test was used with a distance of 1,300 mm between the fulcrums and a distance of 150 mm between two central loading points. The minimum stress was set at 30 MPa with pulsating stress and the number of cycles was limited to 2 million. The rail base was ground with a grinder to prevent fatigue failure from the rail base due to rust surface irregularities. This allowed only the fatigue strength of the gas pressure welds to be evaluated. Figure 9 shows the bending fatigue test situation and Table 3 shows the results of the bending fatigue test. First, two gas pressure welds were tested at a stress amplitude of 320 MPa, which is the 2 million cycles fatigue limit of a standard gas pressure weld. As a result, one weld was unbroken after 2 million cycles, while one weld failed after about 1.3 million cycles. Therefore, tests were carried out on two welds under conditions where the stress amplitude was reduced to 300 MPa. The results showed that the two welds were unbroken after 2 million cycles.

Figure 10 shows a photograph of the fracture surface of the No. 2 weld that broke at a stress amplitude of 320 MPa and a magnified observation of the crack initiation point. A circular flat fracture sur-

Fig. 9 Bending fatigue test situation

Table 3 Results of the bending fatigue test

No.	Stress (MPa)			Cycles
	Max	Min	Stress amplitude	
1	350	30	320	2,000,000
2	350	30	320	1,298,000 (Broken)
3	330	30	300	2,000,000
4	330	30	300	2,000,000

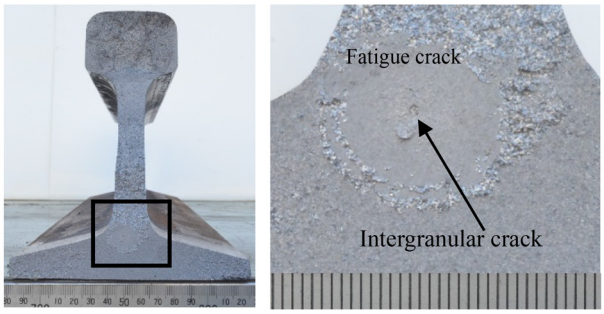

(a) Fracture surface of No. 2 (b) Magnified rail base

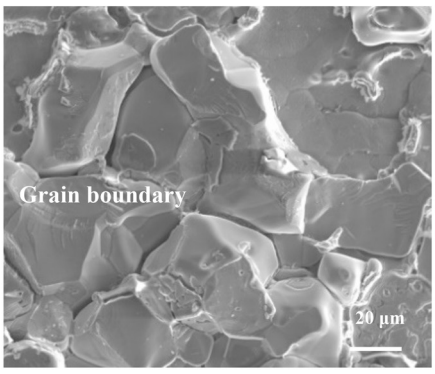

(c) Intergranular crack

Fig. 10 A photograph of the fracture surface of weld No. 2

face was observed in the lower neck region, indicating fatigue crack propagation. Magnified observation of the center of the flat fracture surface revealed a fracture surface of an intergranular crack presenting a grain boundary as shown in Fig. 10(c). Intergranular cracking is a form of hot cracking caused by the melting of old austenite grain boundaries in the rail base metal. It is a typical welding defect that occurs internally in flash and enclosed arc welding on rails. In addition, such defects may occur on the surface in the vicinity of the weld interface due to excessive heat input in standard gas pressure welds, but such defects do not occur internally due to compression. It is assumed that intergranular cracks will remain internal to the rail because of the reduced upset distance in the present method.

The fatigue test conditions with a stress amplitude of 320 MPa are extremely severe compared to the rail stresses that occur in practical use. It is also known that in practical use, fatigue failure occurs from the rail base, initiated from the rust surface irregularities, as described above [5]. From these facts, it is considered that this defect is not the initiating point for fatigue failure in practical use.

4.4 Macro and micro examination

One prepared weld was cut in the central longitudinal section of the gas pressure weld and, the macrostructure was observed. Figure 11 shows the macrostructure of the etched gas pressure weld. In the head, web and base regions, the HAZ was found to be 20 mm wider than the standard rail gas pressure weld [6]. This is thought to be because the heat input remains the same and only the upset distance is less. The web has a smaller cross-sectional width than the head and base and is more affected by heat, resulting in a larger width of the HAZ, which is similar to that of standard rail gas pressure welds.

Figure 12 shows the microstructure observed by optical microscopy on the central longitudinal section of the gas pressure weld. Observations were made at five locations 5 mm below the rail head surface: (1) center of the weld, (2) center of HAZ and the boundary of the HAZ, (3) boundary of the HAZ, (4) base metal in the vicinity of the HAZ, and (5) base metal. Large grains were observed in the vicinity of the center of the weld where the temperature was higher, while fine grains were observed in the vicinity of the boundary of the HAZ. No abnormal microstructure such as martensite was observed at any of the observation points, and the metallurgical structure was similar to that of a standard gas pressure weld.

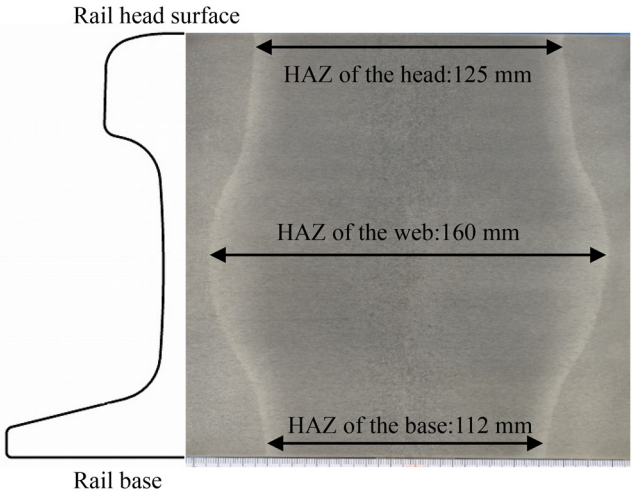

Fig. 11 Macrostructure of etched gas pressure weld

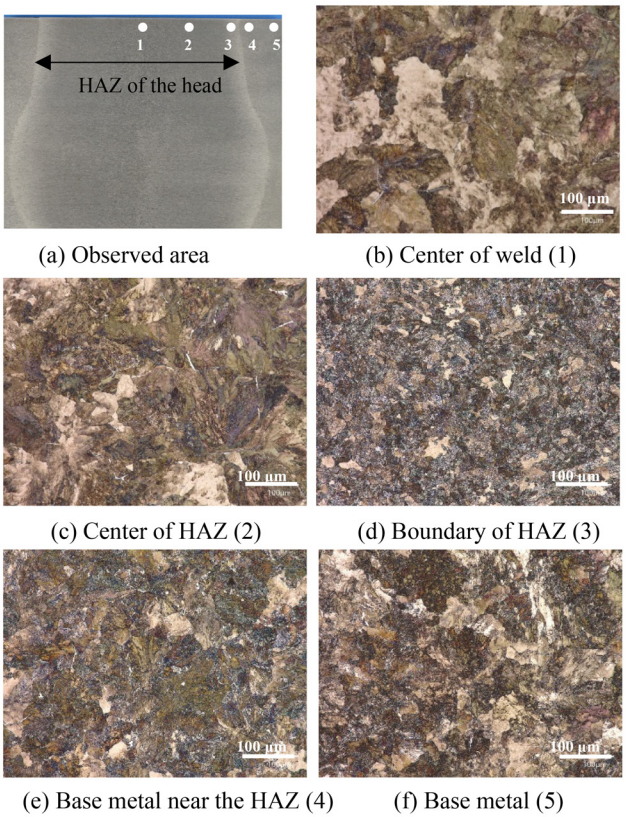

(a) Observed area (b) Center of weld (1)

(c) Center of HAZ (2) (d) Boundary of HAZ (3)

(e) Base metal near the HAZ (4) (f) Base metal (5)

Fig. 12 Microstructure of gas pressure weld

5. Conclusions

In this study, we carried out the various studies by means of rail GPW tests and numerical analysis with the aim of reducing the upset distance and thereby omitting the trimming process. The results are as follows:

(1) A gas pressure welding method with short upset distances has been proposed using the variable pressure method, which allows an upset distance of 6 mm and eliminates the need for a trimming process. The welds produced by the proposed method was found to have a bending strength exceeding the threshold for load and deflection of standard rail gas pressure welds in slow bending tests, and a bending fatigue strength with a stress amplitude of more than 300 MPa in bending fatigue tests.

(2) The weld temperature and deformation of welds in the constant pressure method and the variable pressure method were evaluated using a heating and deformation analysis model of rail gas pressure welds. The results showed that the temperature of each part in the variable pressure method increased by about 100°C compared to the constant pressure method due to the increase in the heating time. The increase in the temperature of the weld interface caused the deformation to concentrate in the vicinity of the weld interface, resulting in an increase in the equivalent plastic strain. These factors are thought to have contributed to the breakup and refinement of the oxide inclusions on the weld interface, thereby improving the weld quality.

References

[1] Hakusan Shoji Co., Ltd., "Rail Gas Pressure Welding Apparatus," https://www.hakusanshoji.co.jp/en/products/rail_gas_pressure.html (Accessed: 16 June 2025).

[2] Tatsumi, M., Fukada, Y., Ueyama, K., Yamamoto, R., "Improvement of Gas Pressure Welding for Rail," *RTRI Report*, Vol. 13, No. 5, pp. 27-32, 1999 (in Japanese).

[3] Itoh, H., Yamamoto, R., Aizawa, H., Izutsu, H., Iwasaki, N., "Thermal Deformation Analysis of Gas Pressure Welding of Rail," *RTRI Report*, Vol. 36, No. 3, pp. 47-52, 2022 (in Japanese).

[4] Itoh, H., Yamamoto, R., Sasaki, T., "Heat Deformation Analysis using a Finite Element Model on Gas Pressure Welding for Steel Bar," *Quarterly Journal of the Japan Welding Society*, Vol. 38, No. 4, pp. 418-428, 2020 (in Japanese).

[5] Deshimaru, T., Kataoka, H., Abe, N., Ohno, M., "Life Prediction of Used Continuous Welded Rail," *RTRI Report*, Vol. 20, No. 4, pp. 5-10, 2006 (in Japanese).

[6] Yamamoto, R., Tatsumi, M., Itoh, H., Terashita, Y., Yoshida, Y., "Gas Pressure Welding Method of Rails by Mixed Gas of Hydrogen and Ethylene Gas," *Quarterly Report of RTRI*, Vol. 55, No. 1, pp. 39-45, 2014.

Authors

Hajime ITOH, Ph.D.
Senior Researcher, Rail Maintenance & Welding Laboratory, Track Technology Division
Research Areas: Rail welding, Inspection of Rail and Weld

Yuki KONAYA
Researcher, Rail Maintenance & Welding Laboratory, Track Technology Division
Research Areas: Rail welding, Inspection of Rail and Weld

Validation of Finite Element Analysis Accuracy through Collision Test Using an Actual Railway Carbody Structure and a Dump Truck

Tomohiro OKINO
Vehicle & Bogie Parts Strength Laboratory, Vehicle Technology Division (Former)

Keisuke NAGATA **Jun-ichi TAKANO**
Vehicle & Bogie Parts Strength Laboratory, Vehicle Technology Division

It is impractical to conduct collision tests with an actual train unit to design crash safety structures. Numerical simulation is effective, but it is important to validate its analytical accuracy. Therefore, the authors conducted a collision test of a full-scale partial stainless steel carbody structure of railway vehicle's lead car and a typical large dump truck. In addition to the test, FE analysis was conducted under the same conditions as the experimental test in order to compare numerical and experimental results, and this obtained agreement between both sets of results. Finally, using the FE analysis, the authors estimated the impact deformation and fracture behavior of the railway carbody under the actual level-crossing accident.

***Key words*:** *carbody structure, crashworthiness, collision test, finite element analysis*

1. Introduction

An essential railway safety measure is to have a carbody structure that mitigates injuries to passengers and crews in the event of a collision. Repeatedly conducting collision tests using actual cars is not a realistic method for designing a carbody structure that is safe in the event of a collision. Numerical analysis is practical. However, ensuring the accuracy of these analyses is important.

The study for this paper was designed to improve understanding about the impact behavior of a lead car in a collision. In a previous study, we conducted a collision test between a full-scale partial stainless steel carbody structure of railway vehicle's lead car and a rigid wall. Subsequently, we conducted an FE analysis simulating the collision test, and the numerical results were compared with the test results in order to improve the accuracy of the FE analysis model (hereinafter referred to as FE model) [1]. We refer to this study as "previous study" for convenience. Furthermore, we also conducted a similar test and analysis for collision with large dump truck [2].

This paper revisits Reference 2, which examined collisions with a large dump truck, with additions and revisions. A full-scale partial carbody structure with the same structure as the previous study was used to collide with a large dump truck. Collision test conditions were based on a level crossing accident scenario corresponding to actual circumstances in Japan. This allowed us to obtain basic data such as the impact deformation and fracture behavior of both the carbody and dump truck structures, as well as the time histories of impact load and impact deceleration. Next, we sought to confirm that the three-step validation program of crashworthiness stipulated in the European standard [3] could be applied under conditions appropriate to actual conditions found in Japan. For this purpose, we conducted an FE analysis that simulates a collision test with a large dump truck using the carbody model constructed in the previous study, and then we compared the test results with the numerical results. In addition, we expanded the model representing a partial carbody structure to a model representing total mass of an actual lead car. By conducting a collision analysis with a large dump truck using this expanded model, we estimated the impact deformation and fracture behavior of the carbody in an actual accident, as well as the time histories of the impact load and impact deceleration.

2. Collision test between carbody structure and large dump truck

2.1 Collision test conditions and measurement system

We conducted the collision test using a disused standard stainless steel lead car that was mass-produced in the late 1980s. Specifically, as shown in Fig. 1, the carbody structure was cut at the rear end of the bolster beam, and a reinforcing plate was attached to the cut surface to prepare a test specimen, which was then attached to a 'running carriage' (used to carry the test specimen) via load cells.

The outer dimensions of the test specimen were approximately 3.2 m long × 3 m wide × 3 m high, and the total mass, including the running carriage, was 10.2 tons. The running carriage with the test specimen was made to collide with the left side of a stationary large dump truck at an average collision speed of 15 m/s, similar to that of serious level crossing accidents that previously occurred in Japan (Fig. 1, Fig. 2). The combined mass of the dump truck itself and 10.1 tons of sandbags loaded on the bed was approximately 22 tons. The height from the ground to the bottom of the underframe of the test specimen was approximately 610 mm, which is approximately 390 mm lower than the actual height (drawing dimensions of 1002 mm). This was to lower the center of gravity to safely operate the running carriage with the test specimen at high speed. The measurement system consisted of six 3-component load cells on the above-mentioned running carriage and four 3-axis accelerometers (including A-1', which is a spare of A-1) on the floor directly above the bolster beam shown in Fig. 3. Each longitudinal component of the outputs

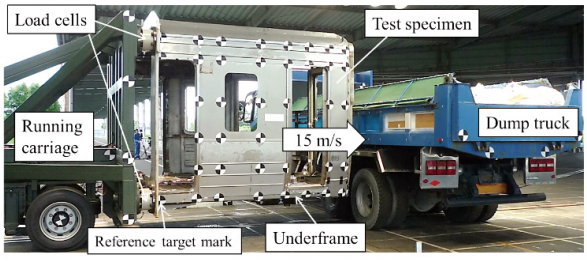

Fig. 1 Test specimen (full-scale partial carbody structure of railway vehicle's lead car) and dump truck

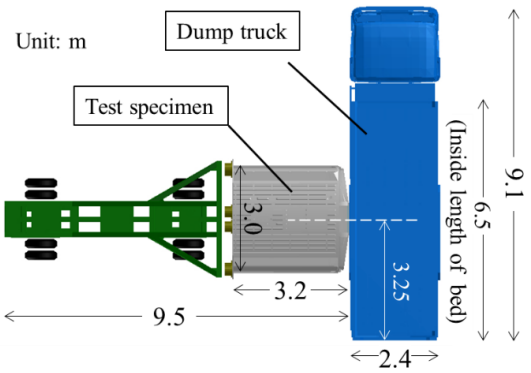

Fig. 2 Horizontal positional relationship between test specimen and dump truck

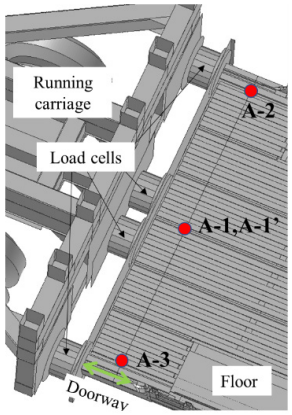

Fig. 3 Location of accelerometers

Fig. 4 Final deformation of dump truck

from these sensors was utilized in this study. Additionally, a tape switch (contact sensor) was attached in front of the gangway pillar, which is expected to make contact with the dump truck first. A datalogger was installed on the running carriage, and the sampling frequency was set to 10 kHz.

The compression load was calculated by applying a CFC1000 filter, which is widely used in the automotive industry [4], to the sum of the compression load values obtained from six load cells. The accelerations obtained from accelerometers were processed using a 50 Hz low-pass filter with no phase delay. The method of calculating the velocity of the test specimen was as follows: first, the coordinates of two reference target marks (on the left and right sides) near the rear end of the underframe, as shown in Fig. 1, were extracted using image processing from the high-speed cameras' images during the collision test process. Each displacement in the longitudinal direction was then calculated and processed using a CFC60 low-pass filter [4]. Finally, their average value was differentiated to obtain the velocity.

2.2 Results of collision test with dump truck

Figure 4 shows the final deformation of the dump truck, Fig. 5 shows the images taken by the high-speed camera during the collision test, and Figs. 6 and 7 show the time histories of the compression load, the velocity, and the acceleration of the test specimen.

As shown in Fig. 5, this collision test was conducted under the condition in which the dump truck bed was located higher than the relatively strong underframe of the test specimen and subsequently overrode the test specimen. This condition is hereinafter referred to as the "overriding condition." When the center of the end face (front face), including the gangway pillars and corner pillars, collided with the bed, the end face was bent, the underframe was also bent so that its front part was lifted upward, and the spot welds on the side outer plate and floor corrugated plate were broken. The center of the gangway frame that connects the upper side of the two gangway pillars was deformed inward in the longitudinal direction by 514 mm. A comparison of the results with those in the previous study showed that the main components of the test specimen were crushed and buckled in the collision test with a rigid wall. In contrast, the main components were bent in the collision test with a dump truck, which resulted in a considerably different impact deformation and fracture behavior.

Meanwhile, the dump truck rotated left when viewed from above, and as shown in Fig. 4, local deformation was observed

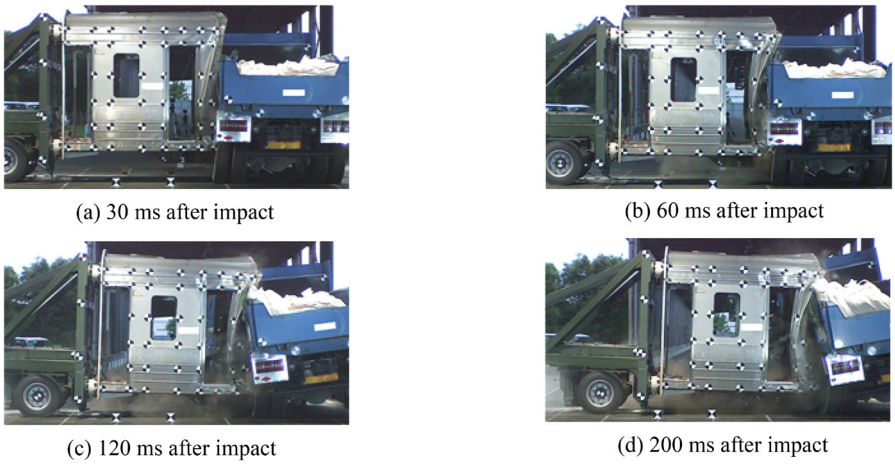

(a) 30 ms after impact (b) 60 ms after impact

(c) 120 ms after impact (d) 200 ms after impact

Fig. 5 High-speed camera images during collision test

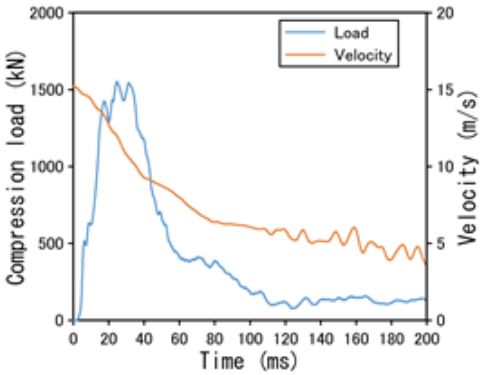

Fig. 6 Time histories of compression load and velocity of test specimen

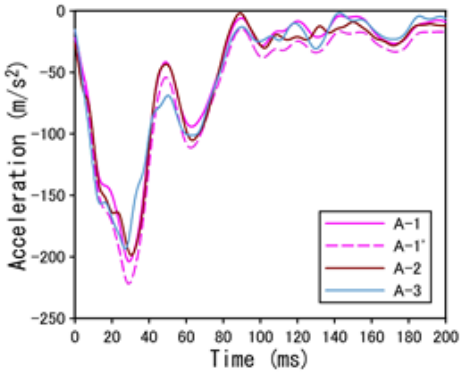

Fig. 7 Time histories of accelerations of test specimen

around the bed where the test specimen came into contact, with the two left rear tire wheels being damaged and breaking. The upper side of the dump truck tire wheels collided with the lower side of the test specimen near the underframe, suggesting that the breaking occurred due to the shear load acting on the tire wheels. A gap was also observed between the main frame and the sub frame, as shown on the right of Fig. 4. This is thought to be due to the main frame being pushed in by the load from the tire wheels in the axial direction of the dump truck.

Figure 6 shows that the compression load acting on the test specimen rose sharply up to 17 ms, maintained a value of approximately 1,500 kN up to 35 ms (maximum load of 1,554 kN), and then dropped sharply to 400 kN at 60 ms, after which the value gradually dropped between 80 and 110 ms, and then maintained a value of approximately 130 kN after 110 ms. Meanwhile, the velocity of the test specimen after the collision at 15 m/s dropped almost linearly to 9 m/s by approximately 40 ms, then 6.4 m/s at 80 ms due to the deceleration rate drop, and finally 3.6 m/s at 200 ms due to further deceleration rate drop. This figure shows that the point where the deceleration rate of the velocity of the test specimen changes almost coincided with the time when the compression load acting on the test specimen suddenly dropped.

Figure 7 shows that the waveforms of the impact deceleration acting on the test specimen were almost identical from A-1 to A-3. The value reached a maximum of 190–220 m/s^2 around 30 ms, then dropped to a local minimum of 40–70 m/s^2 at 50 ms, then increased to a local maximum of 95–110 m/s^2 at 64 ms, and then maintained 17 m/s^2 from 85 ms onwards.

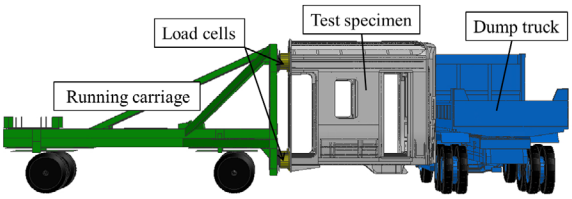

Fig. 8 FE model of test specimen and dump truck

3. Collision analysis between carbody structure and large dump truck

3.1 FE analysis

Figure 8 shows the FE model used in this study. The test specimen and running carriage models were designed to ensure analytical accuracy through comparative verification with the results of collision tests against a rigid wall conducted in the previous study. We considered the strain rate dependency of the various materials used in the carbody and the fracture characteristics of spot welding and arc welding. We conducted an FE analysis in order to simulate the collision test conducted in Section 2. Figure 9 shows the numerical results of the deformation status of the test specimen and the dump truck. Additionally, Fig. 10(a) shows the numerical results of the time histories of the compression load and the velocity of the test specimen, and Fig. 10(b) shows the numerical results of the time history of the acceleration at A-1 in the test specimen along with the test results. A comparison of Figs. 5 and 9 shows that the deformation status of the test specimen over time and the behavior of the dump truck were almost identical. In the test, the final deformation when the center of the gangway frame was pressed in the longitudinal direction was 514 mm, and the numerical result at 300 ms was 488 mm (95% of the final deformation in the test), which was thought to be in good agreement.

A comparison of numerical results (dashed line) with test results (solid line) in Fig. 10(a) showed that the time histories of the compression load and the velocity of the test specimen were in good agreement. The maximum compression load was 1,572 kN, with an error of 1.2%. A comparison of the numerical results (dashed line) and test results (solid line) in Fig. 10(b) showed that the deceleration waveform in A-1 was in good agreement up to approximately 40 ms. However, the fluctuation in deceleration at 40–80 ms could not be simulated, and the steady state after 80 ms was largely simulated. The overall trends were thought to be largely consistent.

The above comparison and verification results of the deformation behavior and various waveform histories confirmed that the test results could be largely simulated. These results confirmed that various deformation and fracture behaviors could be simulated with good accuracy even when the deformation mode is different from a collision test against a rigid wall, such as in the case of a level crossing accident between a train and a dump truck. That is, if a collision test against a rigid wall is conducted using a test specimen from the part of the train where large deformation occurs, and the analysis accuracy of the train model is ensured by comparing and verifying the test results, the model can then be applied to different collision scenarios. Therefore, we confirmed that the three-step validation program of crashworthiness stipulated in the European standard was effective even when adapted to actual circumstances in Japan.

3.2 Estimation of impact behavior at actual height and actual mass

In Section 2.1 we explained that, for safety reasons, the height

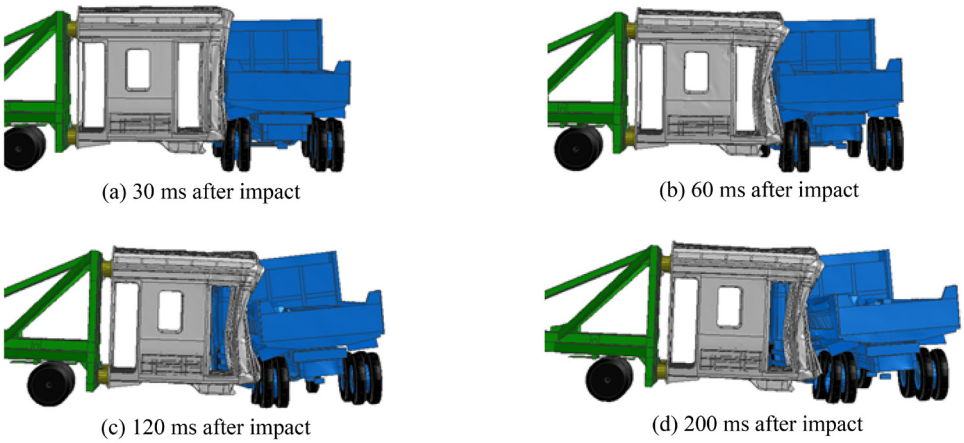

(a) 30 ms after impact (b) 60 ms after impact

(c) 120 ms after impact (d) 200 ms after impact

Fig. 9 FE results of deformed shape and behavior of test specimen and dump truck during collision test

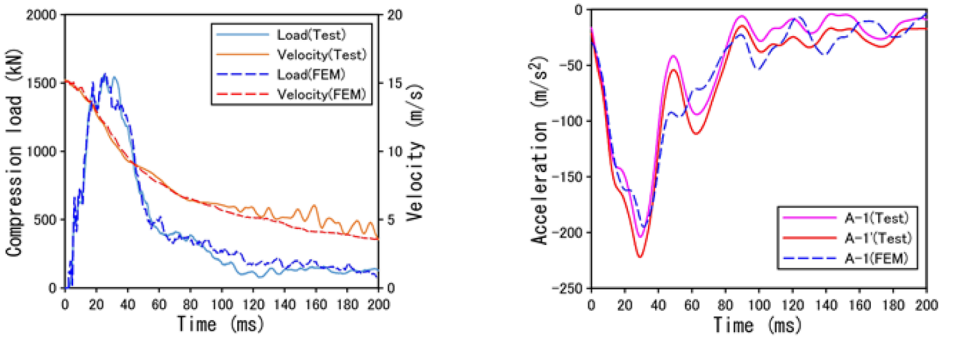

(a) Time histories of compression load and velocity of test specimen

(b) Time history of acceleration (A-1) of test specimen

Fig. 10 Comparison of test and numerical results

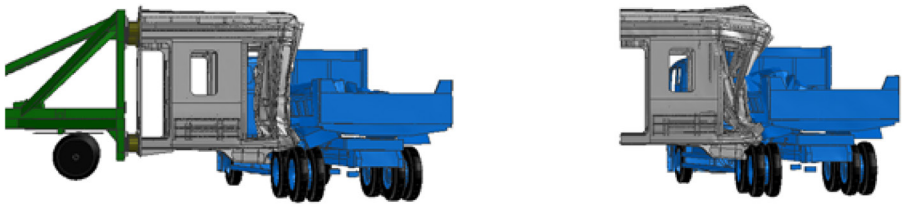

(a) Actual-height setup (200 ms) (b) Actual-car setup (200 ms)

Fig. 11 FE results of deformed shape of test specimen and dump truck under actual-height and actual-car setups

from the ground to the bottom of the underframe of the test specimen was set to approximately 610 mm in the collision test, which is approximately 390 mm lower than the actual height. The FE model simulating the collision test is hereinafter referred to as "experimental setup." We confirmed the impact behavior when the test specimen was at the actual height by conducting FE analysis under the condition where the test specimen height was raised by 390 mm to the actual height ("actual-height setup"). In addition to considering actual height, we added a mass to the FE model to consider the total mass of a lead car ("actual-car setup") and discussed the effect of the mass on the impact behavior. For the actual-car setup, we removed the running carriage, load cells, and reinforcement part attached at the end of the test specimen, leaving only the partial full-scale carbody structure. The unmodeled components from the rear end of the bolster to the rear end of the car were represented using a node. This node, placed at the center of gravity of the unmodeled parts, was assigned the corresponding mass and moment of inertia. It was then attached to the rear end of the FE model. The bogies were modeled in a similar way. The total mass of the model was set to 30.6 tons, and only translational displacement in the longitudinal direction at two nodes representing each bogie's mass was allowed, with all other degrees of freedom of movement and rotation being fixed.

Figures 11(a) and (b) show the numerical results of the deformation of the test specimen and dump truck at 200 ms at the actual-height and the actual-car setup, respectively. Figure 9(d) compares these results and shows that the sinking of the test specimen and the inclination of the dump truck were smaller than those in the experimental setup. This was thought to be because, in the experimental setup, the collision occurred under overriding condition in which the dump truck bed was located above the relatively strong underframe. In contrast, in the actual-height setup, the position of the underframe was relatively higher, and it approached the position of the bed, which decreased the overriding. The increase in train mass also resulted in the test specimen deformation being greater in

Fig. 11(b) than in Fig. 11(a).

Figure 12(a) shows the numerical results of the time history of the compression load, comparing the experimental setup with the actual-height setup. In the actual-car setup, the compression load through the load cells could not be calculated. Therefore, to compare the three FE setups, including the actual-car setup, the contact force between the test specimen and the dump truck was adopted. The numerical results of the time history of contact force under each setup are shown in Fig. 12(b). Figures 12(c) and (d) show the numerical results of the time histories of the velocity of the test specimen and the acceleration at the A-1 position under the three FE setups, respectively.

First, we compared the experimental and the actual-height setups in order to examine the effect of height. Figure 12(a) shows that the compression load in the actual-height setup was smaller than that in the experimental setup up to 45 ms, and was larger from 45 to 100 ms. At 25 ms, the maximum load was 1,374 kN, which was 198 kN smaller than that in the experimental setup. After reaching the maximum load, the load value almost linearly decreased until approximately 120 ms, after which a value of around 140 kN was maintained. Figure 12(c) shows that the velocity of the test specimen was higher in the actual-height setup from 10 to 80 ms. The higher velocity was maintained for a more extended period. Figure 12(d) shows that the deceleration was approximately 195 m/s^2 in the experimental setup, but it was a smaller value of approximately 160 m/s^2 in the actual-height setup. The overall trend was similar to that under the compression load. These differences in the results were suggested to be largely influenced by whether or not the test specimen collided with the tire wheel of the dump truck. In other words, in the experimental setup, the vicinity of the underframe of the test specimen collided with the tire wheel and heavy objects, such as the drive unit of the dump truck, applied a load to the vicinity of the frame through the tire wheel. Meanwhile, in the actual-height setup, no contact was made with the tire wheel, and the load was mainly applied by contact with the dump truck bed. As a result, in the experimental setup, a gap occurred between the main frame and the sub frame, as if the main frame were being pushed in, as shown in the right of Fig. 4. Meanwhile, in the actual-height setup, the gap occurred as if the sub frame were being pushed in. These results suggest that, in the actual-height setup, the mass of the bed, including the sub frame (hereinafter referred to as the upper component), affected the results at first, and that of the main frame of the dump truck, including the drive unit (hereinafter referred to as the lower component), did also but with a delay. In contrast, for the experimental setup, the upper and lower components affect them almost simultaneously, which is thought to be the reason for the above-mentioned difference in results.

Next, we compared the actual-height setup and the actual-car setup in order to examine the effect of train mass. Figure 12(b) shows that the contact force between the test specimen and dump truck was almost identical in the two setups, including the maximum load value, up to 56 ms. Subsequently, the force gradually decreased in the actual-height setup and the force was maintained in the actual-car setup. Finally, the forces at 200 ms were 115 kN in the actual-height setup and 507 kN in the actual-car setup, respectively. These results suggest that the mass added to the rear end of the test specimen did not influence the contact force in the early stage of the collision. Figure 12(d) shows that the deceleration had a maximum value of 160 m/s^2 under the actual-height setup, whereas the value was 51 m/s^2, 32% of the above-mentioned value, under the actual-car setup. This was thought to be because the rate of decrease in the test specimen velocity was smaller in the actual-car setup with a larger train mass, as shown in Fig. 12(c). Since the contact forces in both setups were almost identical up to 56 ms, the deceleration was

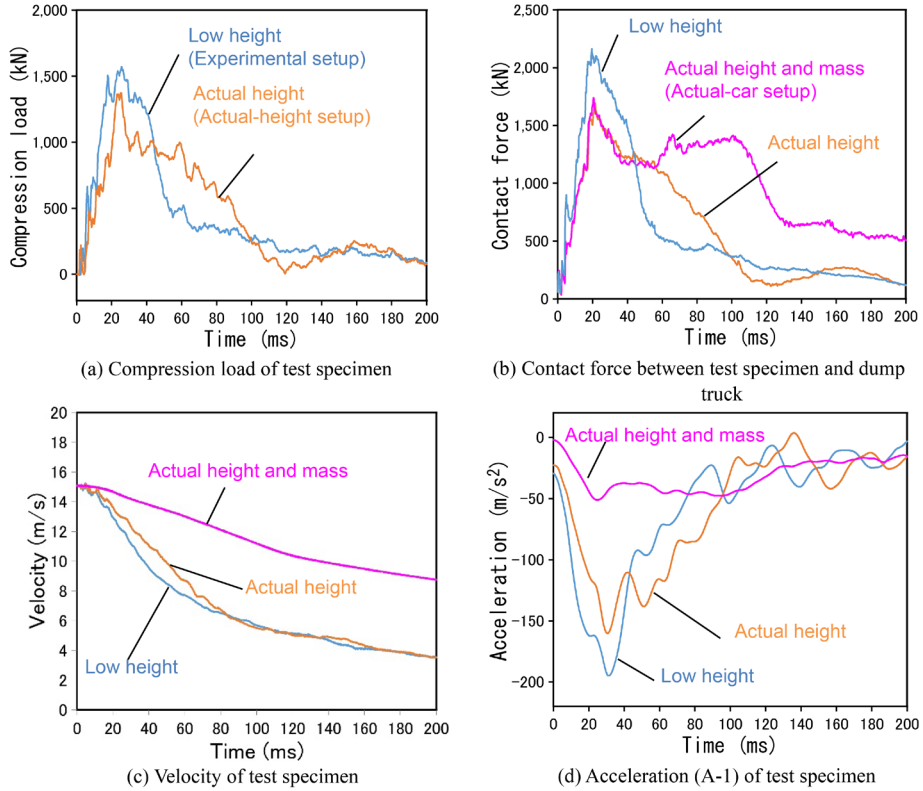

(a) Compression load of test specimen

(b) Contact force between test specimen and dump truck

(c) Velocity of test specimen

(d) Acceleration (A-1) of test specimen

Fig. 12 FE results of time histories of compression load, contact force, velocity and acceleration

thought to be roughly inversely proportional to the train mass up to that time.

4. Conclusions

The goal of this study was to design a carbody structure that mitigates injuries to passengers and crews in the event of a level crossing accident. To this end, this paper sought to improve understanding about the impact behavior of a lead car, and to confirm that the three-step validation program, which combines tests and FE analysis as stipulated in the European standard, can be applied under conditions appropriate to actual conditions found in Japan.

We conducted a collision test on a stationary large dump truck. A full-scale partial stainless steel carbody structure of a lead car was used as the test specimen (total mass of 10.2 tons), and the test specimen collided with the side of a dump truck (total mass of approximately 22 tons) at a velocity of 15 m/s. We then conducted a corresponding FE analysis. The following conclusions were obtained by combining this study with the collision test results and FE analysis conducted in the previous study of a collision between the test specimen and a rigid wall.

(1) The collision of a test specimen with the side of a large dump truck resulted in the front face and front of the underframe of the test specimen being bent and deformed, with fractures being observed in the spot welds of the side outer plate and floor corrugated plate. The dump truck was rotated, and local deformation was observed in the bed. By conducting the test, we clarified basic data, such as impact deformation and fracture behavior associated with the collision, impact compression load, velocity of the test specimen, and time history of the impact deceleration.

(2) Comparing the test results with a large dump truck and with a rigid wall, a collision with a large dump truck exhibited bending deformation as the main behavior, whereas a collision with a rigid wall exhibited compressive deformation as the main behavior. Despite these differences in the deformation modes of the test specimen, the result of the collision test with a dump truck and the result of the FE analysis based on the model constructed from the collision with a rigid wall showed good agreement. Therefore, conducting a collision test against a rigid wall, which is easier to conduct, and validating the FE analysis for the test will also enable the FE analysis of the collision with a large dump truck with sufficient accuracy. The same was thought to apply when the obstacle's main structural components were located above the frame (e.g., the obstacle representing a tank truck defined by European standard). In other words, the three-step validation program of crashworthiness stipulated in the European standard was effective even under conditions that were appropriate for the actual circumstances in Japan.

(3) To estimate impact behavior at the actual height and the actual mass, we conducted FE analysis with the actual-height setup. Numerical results showed that the impact behavior differed greatly depending on whether or not the test specimen collided with the tire wheel of a dump truck. Moreover, we expanded an FE model that was capable of accurately simulating the collision tests with large dump trucks to enable the consideration of the mass of an actual lead car. In the collision analysis assuming an actual accident, we estimated the deformation behavior, the compression load, the car velocity, and the time history of the deceleration. It is expected that the data from this study can make an important contribution to knowledge for setting collision scenarios that correspond the actual conditions found in Japan.

The model for analyzing level crossing accidents between a train and a large dump truck that was constructed in this study will be utilized in our further study, to continue verification under various collision conditions and to continue examining car design guidelines in order to mitigate injury to passengers and crews in the event of a collision.

References

[1] Okino, T., Nagata, K., Sato, H., Horikawa, K. and Kobayashi, H., "Impact test of typical Japanese railway vehicle structure against a rigid wall for validating numerical simulation," *Proceeding of International Symposium on Impact Engineering 2019*; 2nd–5th July, Gmunden Austria.

[2] Okino, T., Nagata, K., Takano, J. and Kobayashi, H., "Collision test and FE analysis of actual railway carbody structure made of stainless-steel against dump truck," *Transactions of the JSME*, Vol. 87, No. 902, 2021, DOI: 10.1299/transjsme.21-00073 (in Japanese).

[3] CEN, "EN15227:2020 Railway applications – Crashworthiness requirements for railway vehicles," 2020.

[4] ISO 6487, "Road vehicles – Measurement techniques in impact tests – Instrumentation," 2015.

Authors

Tomohiro OKINO, Ph.D.
Senior Chief Researcher, Head of Vehicle & Bogie Parts Strength Laboratory, Vehicle Technology Division (Former)
Research Areas: Crashworthiness, Carbody Strength

Keisuke NAGATA
Assistant Senior Researcher, Vehicle & Bogie Parts Strength Laboratory, Vehicle Technology Division
Research Areas: Crashworthiness, Carbody Strength

Jun-ichi TAKANO
Assistant Senior Researcher, Vehicle & Bogie Parts Strength Laboratory, Vehicle Technology Division
Research Areas: Crashworthiness, Carbody Strength, Fire Safety

Numerical Analysis of Mechanism of Aerodynamic Noise Reduction in Bogie Area by Rounding Corners of Bogie Cavity

Tatsuya TONAI **Toki UDA**
Noise Analysis Laboratory, Environmental Engineering Division

Aerodynamic noise radiated from high-speed trains in operation is attracting attention from an environmental point of view. Bogie areas are known to be the main sources of the aerodynamic noise. Rounding the four corners of the bogie cavity has been proposed as a measure to reduce bogie aerodynamic noise, and wind tunnel tests have confirmed its effectiveness. However, detailed flow fields around the bogie area have not been identified and the mechanism of noise reduction by such measures remains unclear. In this study, numerical analyses of the flow field in the vicinity of the bogie area were carried out to investigate the changes in the flow field caused by the proposed measure and to discuss the reduction mechanism.

Key words**:** *high-speed train, bogie, aerodynamic noise, noise reduction, computational fluid dynamics*

1. Introduction

Aerodynamic noise generated by trains travelling at high speeds is a wayside environmental issue. As train speeds increase, the contribution of aerodynamic noise to overall noise at points used for environmental standard evaluations increases. This may lead to wayside noise exceeding these environmental standards. In addition, low-frequency components of aerodynamic noise below 100 Hz and infrasound (pressure fluctuation) below 20 Hz may cause rattling of house fittings and a sense of psychological or physiological oppression in residents, which may affect the wayside living environment.

One of the main sources of such aerodynamic noise from Shinkansen trains during high-speed operation is considered to be the bogies. It is estimated that aerodynamic noise from bogie areas accounts for about 30% of the overall noise at 320 km/h and increases to about 40% when the speed is increased to 360 km/h [1]. In order to increase the speed of commercial trains, it is necessary to reduce the aerodynamic noise from the bogie areas.

There are two ways to reduce aerodynamic noise from bogies: through measures taken on ground equipment and measures on vehicles. From a cost point of view, it is preferable to implement measures on vehicles. Vehicle measures which change the shape of the bogie section, such as adding deflectors or rounding the corners of the bogie cavity, have been proposed, and wind tunnel tests have confirmed their effectiveness [2]. However, aerodynamic noise reduction mechanisms in bogie sections have not been clarified. Clarifying these reduction mechanisms is expected to inform further development of countermeasures to reduce aerodynamic noise in bogie sections.

In this study, numerical simulations were carried out to clarify one of the mechanisms of aerodynamic noise reduction by countermeasures to reduce aerodynamic noise in the bogie section. This report examines the flow field changes with and without the rounded-corner shape which was confirmed to be effective in wind tunnel tests and discusses the reduction mechanism. Chapter 2 gives an overview of the rounded-corner shape and Chapter 3 describes the analysis of the reduction mechanism by numerical simulation.

2. Rounding corners of bogie cavity

Figure 1 shows an overview of the rounded-corner shape. The rounded-corner shape is a simple countermeasure to reduce aerodynamic noise in the bogie section by filling the four corners of the rectangular bogie cavity, which is called baseline in this report. This shape is one of several reduction measures capable of being installed on a real vehicle without compromising the safety and maintainability of the bogie section, and it is the shape with the highest potential for practical application. The radius of the rounded corners is 700 mm in actual vehicle dimensions.

The effectiveness of the rounded-corner shape in reducing aerodynamic noise at the bogie section has been confirmed in several wind tunnel tests carried out in the past [2]. Table 1 shows the reduction in sound pressure level due to the rounded-corner shape, organized by representative frequencies for aerodynamic noise and pressure fluctuation, respectively.

However, while wind tunnel tests have shown its effectiveness, the details of the mechanism of aerodynamic noise reduction in the bogie section by rounding the corners have not been clarified. One reason for this is the difficulty of obtaining experimental information on the entire flow field in the vicinity of the bogie section. The flow field near the bogie is very complicated, and the narrow bogie cavity makes it very difficult to measure flow velocity, pressure distribution, etc. without disturbing the flow field, making it difficult to conduct multi-point measurements of the flow field in wind tunnel tests and on-vehicle tests. If information on the entire flow field in the vicinity of the bogie is obtained and the reduction mechanism is clarified from the changes in the flow field when aerodynamic noise reduction measures are implemented on the bogie, such as rounding the corners, it is expected that the reduction measures can be further refined.

There are two general aerodynamic noise reduction mechanisms: reduction of the flow velocity and change in the vortex motion. The first mechanism, reduction of the flow velocity, is due to the fact that the power of aerodynamic noise is proportional to the 6-8th power of the flow velocity, so reducing the flow velocity leads to a reduction in aerodynamic noise. The second mechanism, change in the vortex motion, is due to the fact that the aerodynamic source is the unsteady motion of the vortex. In the case of the rounded-corner shape, no significant change in the flow velocity is expected, and it is thought that the reduction in aerodynamic noise is largely due to the change in the vortex motion. In the next section, we will focus on the change in vortex motion.

3. Analysis on noise reduction mechanism based on computational fluid dynamics

Numerical simulation on the flow field is useful to clarify the mechanism of aerodynamic noise reduction in the bogie section by rounding its corners. This chapter describes the results of numerical simulations based on computational fluid dynamics for the unsteady three-dimensional compressible Navier-Stokes equations to analyze the flow field near the bogie.

3.1 Methodology: computational model and conditions

Figure 2 shows a computational model. The model consists of a car body with the same dimensions as a real vehicle and a bogie that is located in the center of the car body. The computational domain is a rectangular domain, which includes a car body of uniform cross section with a bogie and rails. To reduce the calculation cost, the bogie was so simplified that it is composed of the bogie frame, wheel axles, main electric motors, gear units, and air springs, with only the main components that affect the aerodynamic noise of the bogie extracted from its shape. Calculations were carried out for two cases: the baseline and the rounded-corner shape.

Figure 3 shows the domain at which the computational grid is generated in the cross-section perpendicular to the rail direction at the center of the bogie and the maximum grid spacing on the boundary line. The maximum grid spacing is 12.5 mm in the area under the floor of the car, and the maximum grid spacing is increased as the distance from the center of the track increases. The maximum frequency of pressure waves propagating through space can be estimated using the value of the maximum grid spacing. Since approximately 8 grids per wavelength are required to resolve spatial pressure wave propagation, it is possible to resolve pressure waves of 3.4 kHz (= 340 m/s / (12.5 mm × 8)) or less under the floor of a vehicle. Assuming that the pressure fluctuations generated by the bogie cavity reach up to the area of 2.7 m away from the track center (maximum grid spacing of 75 mm), the pressure waves can be similarly resolved up to approximately 550 Hz (= 340 m/s / (75 mm × 8)).

The calculation conditions were set for a train running at 360 km/h (= 100 m/s). Since the freestream Mach number is about 0.3, compressible Navier-Stokes equations were used as the governing equations. Large Eddy Simulation was used for the turbulence model, and the standard Smagorinsky model was used for the subgrid scale model. For the equations of motion, the discretization scheme for the advection term consisted of a second-order accurate central difference and a first-order accurate upwind difference with a mixing ratio of 8:2 (partly 5:5), and the Crank-Nicolson method was used for the time integration method. The inflow condition was a constant velocity of 100 m/s perpendicular to the inlet surface toward the interior of the computational domain, and the outflow condition was a constant pressure of 1.0×10^5 Pa at the outlet surface. On the solid surface, the Spalding law was applied, and the ground and rails were subjected to a travel speed of 100 m/s in the freestream direction, and the wheelsets were subjected to a rotational speed equivalent to 100 m/s travel. The movement of the ground and rails and rotation of the wheelsets are conditions that are difficult to simulate in wind tunnel tests, so there are advantages to performing numerical calculations in this respect as well. The free-slip condition was applied to the top and sides, which are the outer boundaries of the analysis domain. The time step was set to 2×10^{-6} s.

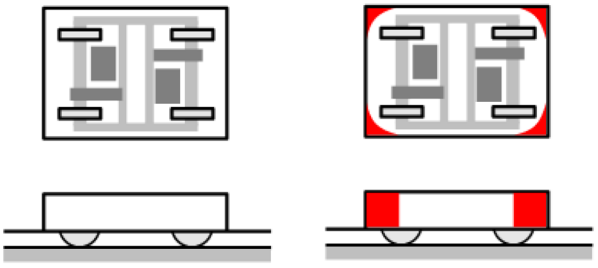

(a) Baseline (b) Rounded-corner shape

Fig. 1 Schematics of bogie cavity

Table 1 Reduction of aerodynamic bogie noise by rounding corners of bogie cavity [2]

Pressure fluctuation				
Frequency band, Hz	< 16	25	50	
Sound pressure level difference, dB	-0.8	-0.1	-0.3	
Aerodynamic noise				
Frequency band, Hz	250	500	1,000	2,000
Sound pressure level difference, dB	-0.3	-0.4	-0.3	0.1

*Negative value means reduction of noise.

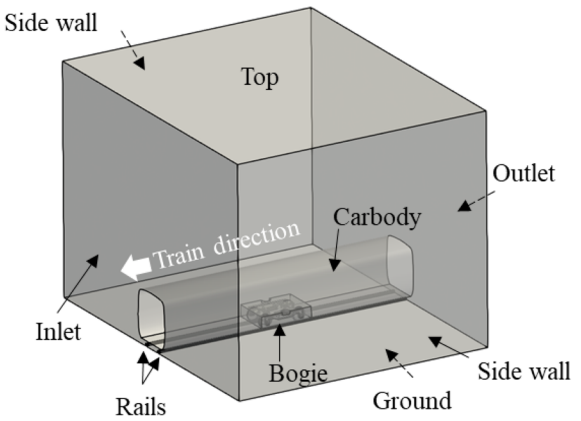

(a) Overview

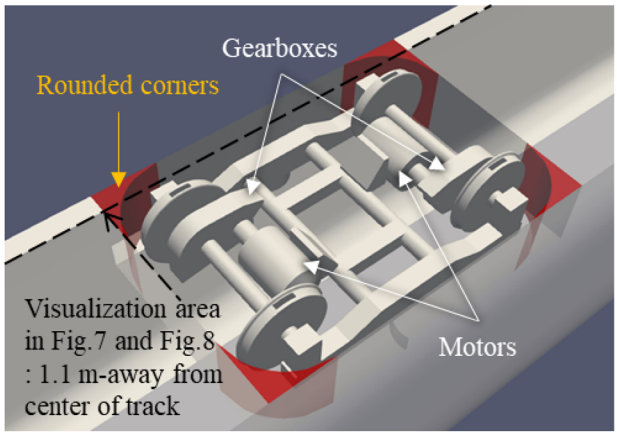

(b) Nearby area of bogie section (upside down)

Fig. 2 Computational model

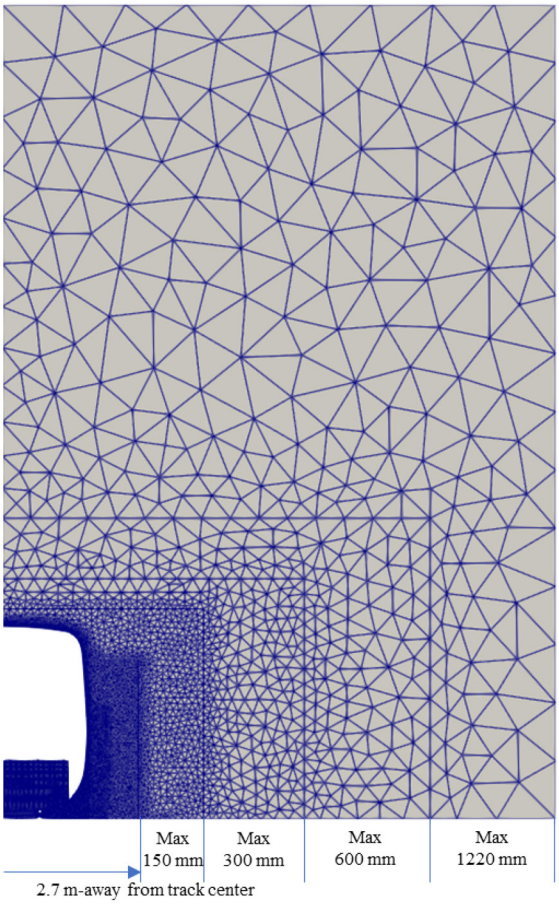

(a) Overview

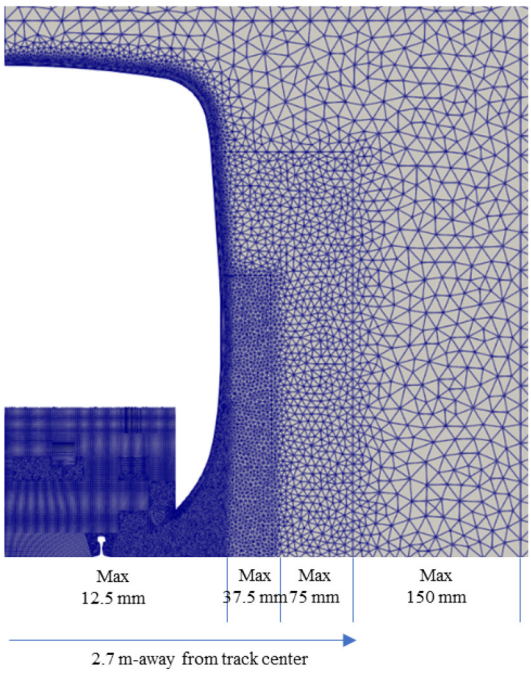

(b) Nearby area of carbody

Fig. 3 Domain when generating computational grid and maximum grid spacing on boundary line

3.2 Results: flow field around bogie

This section describes the trends which are common to the two cases of the baseline and the rounded-corner shape, which is the basic flow field around the bogie. Here we show the visualization results of the vortex based on the Q values and the root mean square (RMS) of the pressure fluctuations on the bogie surface. Q values represent the second invariant of the velocity gradient tensor, and positive Q values represent the vortex strength. By drawing isosurfaces for positive Q values, the vortex distribution can be visualized.

Figure 4 shows the time series variation of the vortex distribution around the bogie section in 3 ms steps. Here, isosurfaces of Q = 10,000 were drawn to represent the distribution of the vortices. The general trend is that vortex-shedding from the leading edge of the bogie cavity and advection along the main flow can be seen. The vortex is a long transverse vortex in the sleeper direction and is periodically shed at a frequency of about 100 Hz. The vortex is transferred downstream over time, impinging on various parts of the bogie (wheels, motors, gearboxes, etc.) and being transformed. The vortex then repeatedly deforms before reaching the trailing edge of the bogie cavity, and the vortex gradually disappears after passing the trailing edge of the bogie cavity. The above trend is common for both the baseline and the rounded-corner shape. On the other hand, a detailed comparison of the figures reveals differences in the distribution of vortices in the vicinity of the side covers, as described in the next section.

Figure 5 shows the power spectral density of each directional component of the velocity variation acquired at the track center position of the front edge of the bogie cavity in the case of baseline. In the power spectral density at about 100 Hz, peaks are observed in the streamwise velocity v and in the vertical velocity w, while not in the velocity u in the sleeper direction. This confirms the presence of transverse vortices periodically shed from the leading edge of the bogie cavity.

Figure 6 shows the RMS of the pressure fluctuations on the bogie surface in the case of the baseline. The streamlines on the surface based on the average velocity are also shown here. Each statistic was calculated in 0.2 seconds. The areas with large RMS of the pressure fluctuation appear locally on the surface of the bogie. Such locations are as follows; (1) the upstream motor, (2) the downstream motor, (3) the downstream gear box, (4) the downstream wheels, (5) the trailing edge of bogie cavity, (6) the side cover edges, (7) the bogie frame corresponding to downstream axle boxes. The streamlines show that these locations are stagnation points, which are thought to be the locations where the advecting vortices collapse. These locations are generally consistent with the locations of the aerodynamic noise sources on the bogie confirmed in previous wind tunnel tests [3].

On the other hand, the RMS of pressure fluctuation does not necessarily increase at stagnation points. In other words, stagnation points are also observed on the upstream wheel and on the surface of the upstream gear unit, but the RMS of the pressure fluctuation does not increase at these locations. These locations are considered to be the positions where the vortices collide with each other, immediately after being shed from the leading edge of the bogie cavity.

Considering the above trends comprehensively, it can be assumed that aerodynamic noise is generated where vortices that were once disturbed by collisions with each part of the bogie, etc., collide again with each part of the bogie.

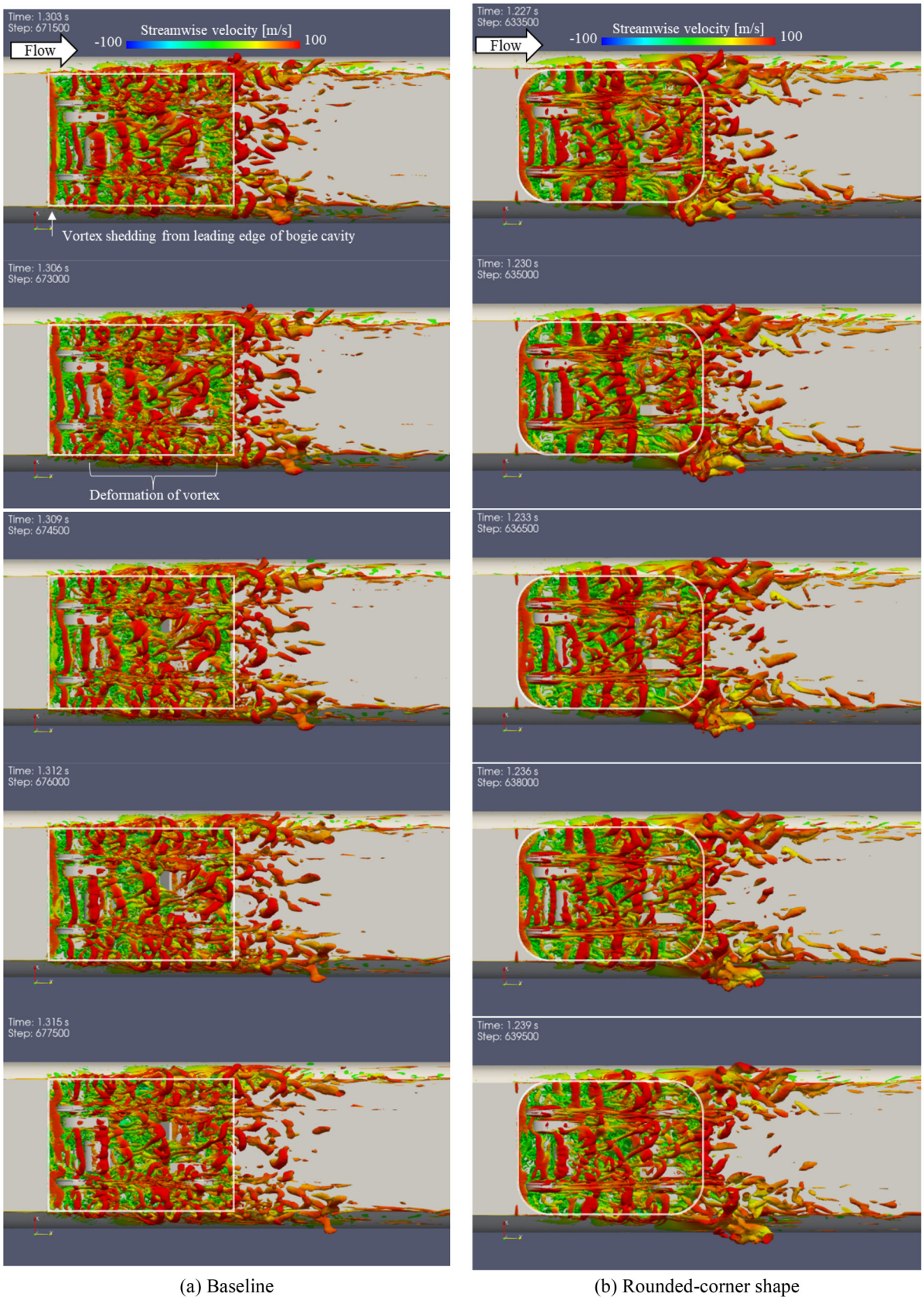

(a) Baseline (b) Rounded-corner shape

Fig. 4 Time series of vortex distribution around bogie (Q = 10,000, colored by streamwise velocity, in 3 ms steps)

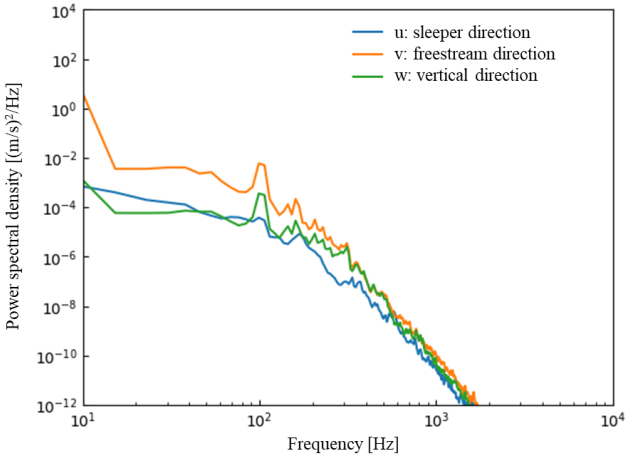

Fig. 5 Power spectral density of each directional velocity component at track center position of leading edge of bogie cavity in case of baseline

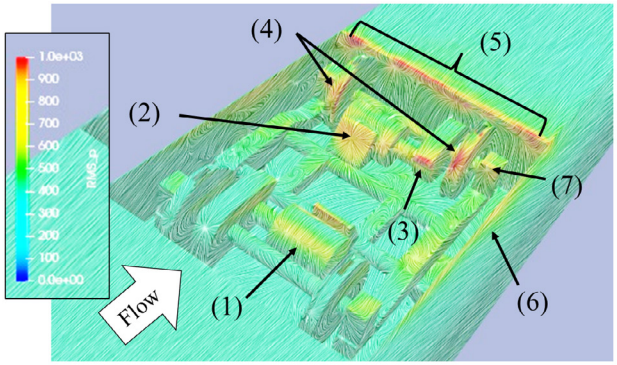

Fig. 6 RMS of pressure fluctuations, unit in Pa

3.3 Results: change in flow field by rounding corners

The change in vortex motion when the corners were rounded was seen in the vicinity of the side covers. Figure 7 shows a comparison of the instantaneous vortex distribution in the vicinity of the side cover when Q = 10,000. The visualization area is the area at least 1.1 m away from the center plane of the track as shown in Fig.2(b). In the rounded-corner shape shown in Fig.7(b), the vortex periodically shed from the upstream corner is advected downstream, keeping its shape. On the other hand, in the case of the baseline in Fig. 7(a), there are not only vortices periodically shedding from the upstream corner, but also vortices appearing as secondary vortices between those vortices. The number of secondary vortices is one or two between the periodically shedding vortices. In both shapes, the spacings between vortices periodically shedding from the corners are approximately equal, so the baseline with secondary vortices has narrower spacings between vortices than the rounded-corner shape. Therefore, it is thought that interference between vortices occurs in the baseline, resulting in fine deformation of the vortices near the downstream corner. The application of the rounded-corner shape is expected to have the effect of suppressing secondary vortex generation and associated vortex deformation.

Figure 8 shows the instantaneous vortex distribution in the vicinity of the side cover when the Q is further increased to 250,000 to see a stronger vortex distribution. The vortex distribution for each shape in Fig. 8 is at the same time as the vortex distribution shown

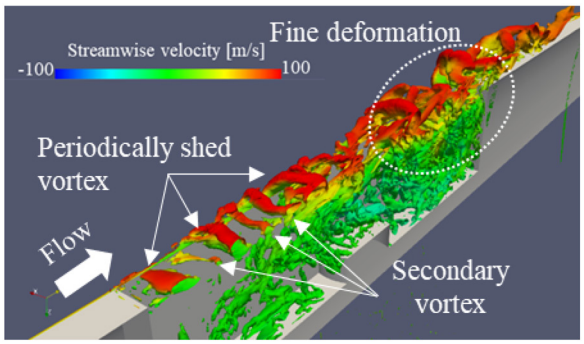

(a) Baseline

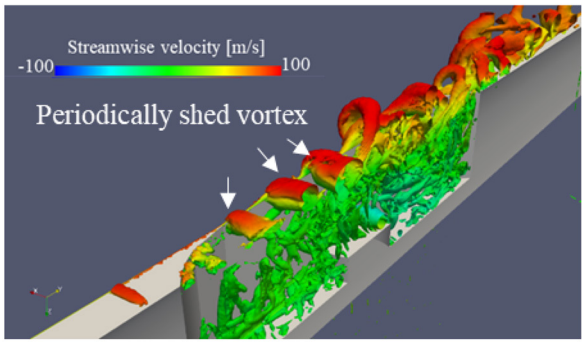

(b) Rounded-corner shape

Fig. 7 Instantaneous vortex distribution near side cover (Q = 10,000, colored by streamwise velocity)

in Fig. 7, with Fig. 8 drawn closer to the vortex core. There are vortices in the vicinity of the upstream corner in the baseline shown in Fig. 8(a), but not in the rounded-corner shape shown in Fig. 8(b). This suggests that the rounded-corner shape has an effect of reducing the strength of the vortices shed from the upstream corner.

3.4 Discussions: noise reduction mechanism by rounding corners

It was found in Section 3.2 that the vortices, once disturbed, collide with various parts of the bogie and generate aerodynamic noise, and in Section 3.3 that the rounded-corner shape suppresses vortex deformation in the vicinity of the side covers and reduces the strength of the vortices shed from the corners. Taking these factors into account together, it can be assumed that turbulent vortices advecting in the vicinity of the side covers collide with the downstream corners of the bogie section and become aerodynamic sources, and that the aerodynamic noise generated here can be reduced by rounding the corners. This therefore suggests that the rounded-corner shape suppresses vortex deformation, which reduces the turbulence of vortices colliding with the downstream corners and thus contributes to the reduction of aerodynamic noise in the bogie section.

4. Conclusions

Numerical analyses were carried out to clarify the aerodynamic noise reduction mechanism on rounded-corner bogie sections, which is one of the countermeasures which can be used to reduce bogie aerodynamic noise. The basic flow field in the vicinity of the bogie is that transverse vortices, which are long in the sleeper direc-

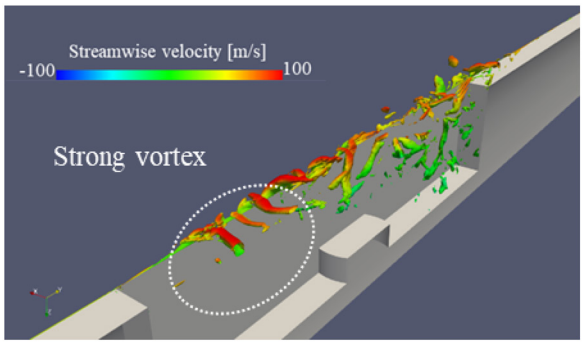

(a) Baseline

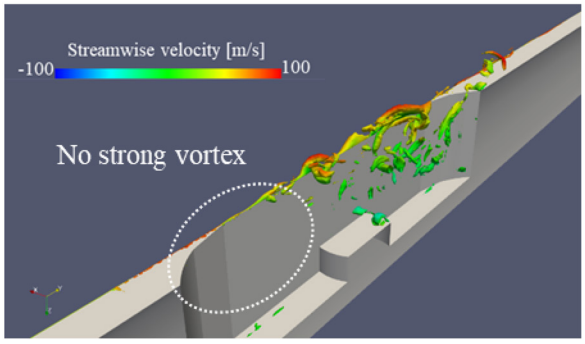

(b) Rounded-corner shape

Fig. 8 Instantaneous vortex distribution near side cover (Q = 250,000, colored by streamwise velocity)

tion, are periodically shed from the leading edge of the bogie cavity and advected along the freestream, repeatedly colliding with each part of the bogie and deforming, and finally the vortex gradually disappears after passing through the trailing edge of the bogie cavity. The vortex shedding frequency is approximately 100 Hz. Furthermore, the rounded-corner shape suppresses vortex deformation in the vicinity of the side covers and reduces the strength of the vortex shedding from the upstream corner. Taking the above into consideration, it is believed that the aerodynamic noise in the bogie generated by the downstream corner is reduced by rounding the corner.

References

[1] Nagakura, K., "Recent Studies on Wayside Environmental Problems, " *Quarterly Report of RTRI*, Vol. 58, No. 2, pp. 88-92, 2017.

[2] Uda, T., Akutsu, M., Kawaguchi, T. and Ogata, Y., "Sound source distribution of high-speed trains and reduction of aerodynamic bogie noise," *INTER-NOISE and NOISE-CON Congress and Conference Proceedings*, InterNoise22, Glasgow, Scotland, Pages 2999-3998, pp. 3709-3716(8), 2022.

[3] Uda, T., Murata, K. and Kitagawa, T., "Identification of aerodynamic bogie noise for high speed trains," presented at the *13th Western Pacific Acoustics Conference*, Delhi, India, November 11-15, 2018, AA3/03.

Authors

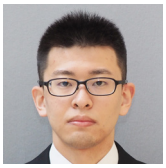

Tatsuya TONAI
Researcher, Noise Analysis Laboratory, Environmental Engineering Division
Research Areas: Railway Noise

Toki UDA, Ph.D.
Senior Chief Researcher, Head of Noise Analysis Laboratory, Environmental Engineering Division
Research Areas: Railway Noise

Aerodynamic Noise Reduction of Pantograph Head Support by Applying Flow Bypass Technique

Takeshi MITSUMOJI **Yuki AMANO**
Current Collection Laboratory, Railway Dynamics Division

Mariko AKUTSU
Noise Analysis Laboratory, Environmental Engineering Division

Kyohei NAGAO
Current Collection Laboratory, Railway Dynamics Division

Isamu MAKARA
Current Collection Laboratory, Railway Dynamics Division (Former)

Yusuke WAKABAYASHI
East Japan Railway Company

Reducing aerodynamic noise emitted by pantographs is one of the key challenges to be overcome to reduce the environmental impact of railways and enable faster train running speeds. Previous studies proposed a method for reducing aerodynamic noise by applying porous material to pantograph head support covers. This study proposes a new practical method to achieve the same aerodynamic noise reduction effect as using porous material. Wind tunnel test results showed that this new method can reduce aerodynamic noise to almost the same extent as using porous material.

Key words**:** *pantograph, head support, aerodynamic noise, porous material, flow bypass technique*

1. Introduction

To achieve higher speed on Shinkansen, it is important to reduce noise generated by trains, particularly aerodynamic noise which increases proportionally from the sixth to the eighth power of the train speed. Among Shinkansen vehicle components responsible for noise, pantographs are one of the main sources of aerodynamic noise. Pantograph heads and head supports (Fig. 1) in particular are known to be major contributors to this noise.

Pantograph heads, which slide against the overhead wire, in particular, are a challenge. This is because not only is it necessary to reduce aerodynamic noise, it is also essential to stabilize lift characteristics (i.e., lift characteristics must not change significantly with variations in the direction of the oncoming wind or changes in contact strip shape caused by wear). Consequently, the most common cross-sectional shape of pantographs is rectangular as shown in Fig. 2(a) (henceforth referred to as "current pantograph head"). Given these considerations, previous research used a combination of CFD (Computational Fluid Dynamics) analysis and shape optimization to propose a pantograph head cross-sectional shape that reduces aerodynamic noise and stabilizes lift characteristics based on the assumption of unidirectional running [1], and also developed a multi-segmented smooth-profile pantograph head with a suspension mechanism based on that cross-sectional shape [2, 3] (Fig. 2(b), Fig. 3).

Another important aspect in reducing aerodynamic noise generated by pantograph heads and head supports is controlling the flow interference caused by these parts. Based on the assumption of running in the knuckle forward direction, a previous study proposed aerodynamic noise reduction measures, such as an improved head support that reduces flow interference by offsetting the pantograph head's installation position upstream and applying a porous material to the cover of the head support [3] (Fig. 3). Of these aerodynamic noise reduction measures, the application of a porous material is straightforward as it only changes the surface properties of the member without significantly changing its shape or structure. The structural characteristics of the porous material also necessitate adhesive installation, but research has confirmed that the installation strength was not inhibited in cases of application to actual vehicles [4], and this is considered to be a technology that has a certain prospect for practical application. However, the porous material may be crushed or deformed when struck by a flying object, and replacing only the porous part is difficult because it is attached with an adhesive. Therefore, to ensure the practical application of aerodynamic noise reduction methods by improving the surface properties of members, such as porous materials, it is essential to improve the strength and maintainability of these members. In some cases, new methods that do not rely on porous materials may be needed. To that end, in this study, we propose a flow bypass method as a practical alternative method that can reduce aerodynamic noise based on the same principle as that of porous materials and improve the strength and maintainability of members. We confirmed the aerodynamic noise reduction effect in a wind tunnel test.

2. Porous material and flow bypass method

A porous material has countless pores, as shown in Fig. 4, and a structure in which adjacent pores are connected to each other is known to be necessary for reducing aerodynamic noise. Previous research has also clarified that the aerodynamic noise reduction effect of porous materials is not due to acoustic effects such as sound absorption, but rather due to a fluid dynamic effect in which the flow field is stabilized by the natural inflow and outflow of air that occur

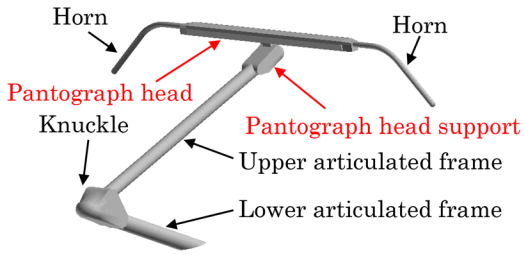

Fig. 1 Configuration of Shinkansen pantograph

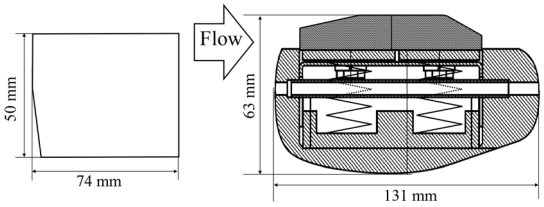

(a) Example of the current pantograph head (b) Multi-segmented smooth-profile pantograph head

Fig. 2 Cross-sectional shape of Pantograph head

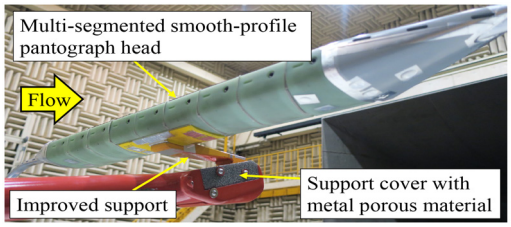

Fig. 3 Aerodynamic noise reduction measures for pantograph head and head support

on the surface of the porous material [5]. Therefore, designing a structure in which natural inflow and outflow of air occurs according to the pressure differential on the member surface is important for achieving the effect of porous materials by another method.

In this study, we assume that a metal porous material is applied to a head support part as shown in Fig. 3, and propose an alternative method to the porous material, in which the flow is bypassed from the upper surface to the side by providing a flow channel at the corner of the upper side of the head support (flow bypass method). Figure 5(a) shows an overview of this method. This method involves connecting the upper side of the head support's upper corner, where the flow stagnates and the pressure rises, to the lateral side, where the flow separates and the pressure falls, with a bypass channel. The aim is to generate a natural inflow and outflow from the upper side to the lateral side.

The test sample was a currently used head support cover widened by 10 mm in the lateral direction and a removable member with a bypass channel at the corner. The area to which the bypass channel is applied generally has a width W = 10 mm, height H = 10 mm, and length L = 128.5 mm in the ridge line direction. As shown in Fig. 5(b), the bypass channel is generally provided in the two directions of "direction 1" perpendicular to the upper surface of the apex and "direction 2" perpendicular to the lateral side, with some tests adding a bypass channel in "direction 3" parallel to the ridge.

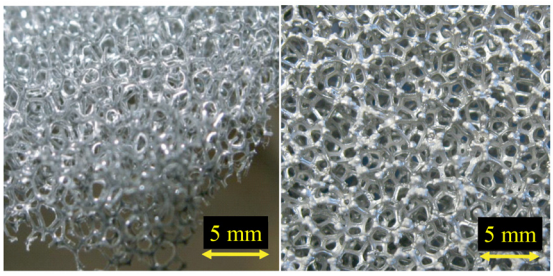

(a) Urethane (b) Metal

Fig. 4 Porous material

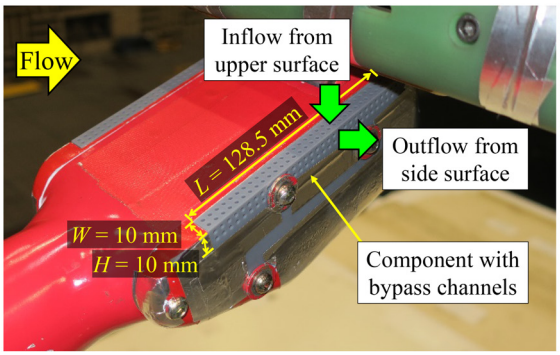

(a) Overview

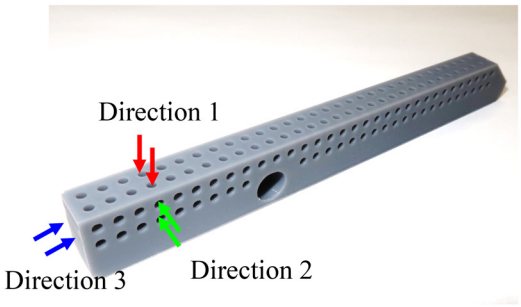

(b) Member with flow channel

Fig. 5 Application of flow channel to head support

3. Overview of wind tunnel test

The wind tunnel test was conducted in the Railway Technical Research Institute's large-scale low-noise wind tunnel (open-type measurement section, air outlet 3 m × 2.5 m, maximum wind speed 111 m/s) using a real pantograph for Shinkansen trains as the test sample. Figure 6 shows the wind tunnel test conditions. The pantograph head was a multi-segmented smooth-profile pantograph head [2, 3], shown in Figs. 2(b) and 3, and the pantograph was installed in the knuckle forward direction. The test wind speed was 100 m/s (360 km/h), and the Reynolds number during the test was 6.5×10^5, which was calculated using the lateral width of the head support as the representative length. The main purpose of this test was to evaluate the aerodynamic noise of the head support and to minimize the noise emitted from other parts, the test was generally performed with all tap holes and movable gaps in the multi-segmented smooth-profile pantograph head sealed off with tape (Fig. 6(b)).

The aerodynamic noise measurement was conducted under conditions where the entire pantograph was exposed to the airflow, and the aerodynamic noise was evaluated using an omnidirectional microphone installed diagonally below the side of the pantograph.

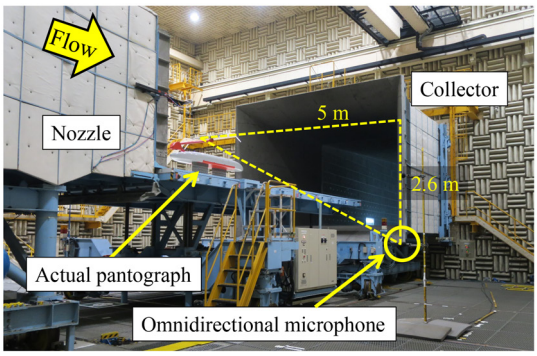

(a) Overview

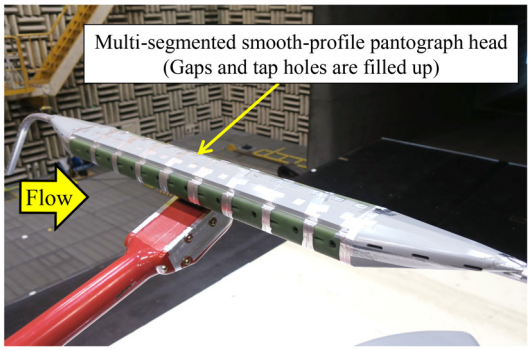

(b) Pantograph head and head support

Fig. 6 Wind tunnel test

The omnidirectional microphone was installed 356 mm upstream from the center of the pantograph head in the flow direction, 5 m to the side of the center of the pantograph head in the lateral direction, and 2.6 m below the upper surface of the pantograph head in the vertical direction. The noise level was calculated by conducting 1/3 octave band frequency analysis on the aerodynamic noise measurement waveform and applying A-weighting correction. The overall value was generally evaluated using the partial overall value ("POA value") calculated from the frequency band of 400 Hz or more, which is the frequency band where the contribution of the head support is dominant. Furthermore, conditions equivalent to background noise were set by conducting tests with the pantograph head removed in order to prevent the influence of flow interference with the pantograph head and head support, and these results were shown with the aerodynamic noise measurement results as needed.

4. Wind tunnel test results

4.1 Effect of bypass channel and influence of internal bypass channel configuration

First, the test conditions for the four types of head support shown in Fig. 7 were set to confirm the effect of applying bypass channels and the influence of the internal bypass channel configuration [6]. In this study, the cover of the currently used head support (Fig. 7(a) hereinafter "currently used") was widened by 10 mm in both the left and right directions (Fig. 7(b) hereinafter "widened"), and a bypass channel was introduced in the corner of the "widened" head cover (Fig. 7(c), hereinafter "bypass"). Furthermore, as a comparison of the aerodynamic noise reduction effect, aerodynamic noise measurements were conducted for the condition where a urethane porous material (Inoac Molto Filter MF-13) was applied to the corner of the "widened" head cover (Fig. 7(d), hereinafter "porous"). Here, for "bypass," circular bypass channels with a diameter of 2 mm were arranged with a center-to-center distance of 4 mm, and three conditions for the direction of the bypass channels were set as shown in Fig. 8. Specifically, the following three conditions were set: "2-axes" (Fig. 8(a)), in which the bypass channels were made in direction 1 and direction 2; "3-axes" (Fig. 8(b)), in which a bypass channel in direction 3 was added to "2-axes" (Fig. 8(b)); and "cavity" (Fig. 8(c)), in which a bypass channel in direction 3 had a rectangular cross-section of 6 mm × 6 mm. For all bypass channel conditions, the members with bypass channels were made using a 3D printer. Furthermore, given the constraints of dividing the parts that constitute the corners, the external dimensions of the porous material were set to W = 10 mm, H = 16.7 mm, and L = 139.1 mm (see Fig. 5(a) for the parts marked with each symbol), which are slightly larger than the applicable area of the bypass channels.

Figure 9 shows the aerodynamic noise measurement results of this study. Referencing the comparison diagram of the POA values (Fig. 9(a)), the POA values of the "currently used" and "widened" support covers were almost identical, and we can confirm that the impact of widening the support cover on the aerodynamic noise was small. Given this, POA values when various bypass channels are made were compared, using "currently used" as the reference, showed an aerodynamic noise reduction effect of 0.6–0.7 dB, where it could be confirmed that the difference in aerodynamic noise due to the internal bypass channel configuration was also small. However, for the "porous" case, the POA value was reduced by 0.9 dB. Therefore, the results showed that the aerodynamic noise reduction effect of making the bypass channel was slightly smaller than that when porous material was applied.

Next, focusing on the comparison diagram of the aerodynamic noise spectrum (Fig. 9(b)), conditions where various bypass channels are applied to the "currently used" system showed that the noise level was reduced over a wide frequency band from 400 Hz to

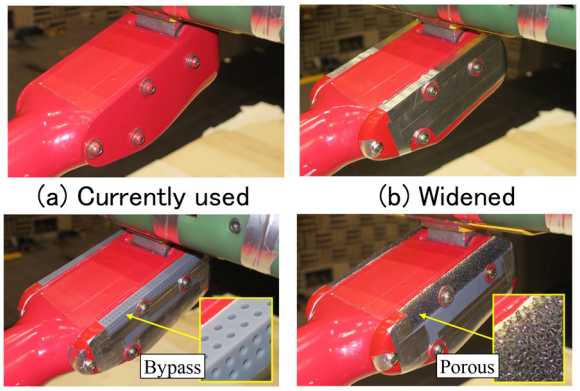

(a) Currently used (b) Widened

(c) Bypass (d) Porous

Fig. 7 Test conditions of head support

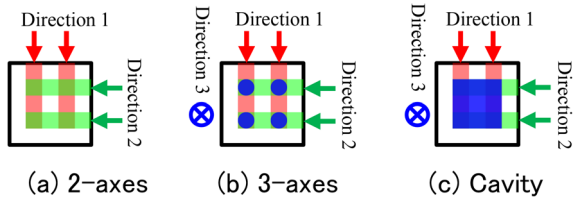

(a) 2-axes (b) 3-axes (c) Cavity

Fig. 8 Bypass channel installation direction (cross-section)

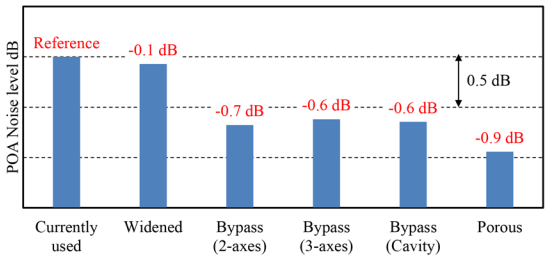

(a) Comparison of partial overall values (POA values)

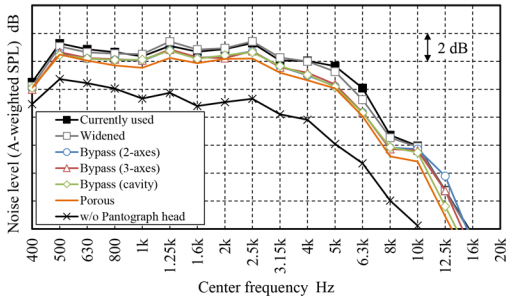

(b) Comparison of aerodynamic noise spectra

Fig. 9 Aerodynamic noise measurement results (wind tunnel test, 360 km/h)

8 kHz, but the aerodynamic noise reduction effect in each frequency band was slightly smaller than that of the "porous" system. Although not at a level that considerably influences the POA value, when focusing on the 12.5 kHz band, we could observe differences depending on the configuration of the internal bypass channel: "2-axes," which omits the bypass channel in direction 3, had a slight peak noise, whereas "3-axes" and "cavity", which add a bypass channel in direction 3, generated no peak noise. The weak peak noise at 12.5 kHz generated in the "2-axes" system was separately confirmed to have no wind speed dependency in its frequency, and because 1/4 of the wavelength of the sound wave (6.8 mm) approximately coincided with the bypass channel depth of 8 mm, this was thought to be air resonance sound with the bypass channel depth being 1/4 of the wavelength. It was also inferred that this peak noise could be reduced by providing a bypass channel in direction 3.

4.2 Effects of bypass channel shape and opening ratio

The results presented in the previous section confirmed that aerodynamic noise can be reduced with a bypass at the corner of the support cover, but the reduction in aerodynamic noise was smaller than that achieved when a porous material was used. This was thought to be due to the insufficient flow rate of the inflow and outflow from the upper surface of the head support to the lateral surface. Therefore, we sought to increase the flow rate of the inflow and outflow by investigating the effect of changes in the cross-sectional shape and size of the bypass channel on aerodynamic noise reduction [7].

Figure 10 shows the opening conditions of the bypass channel. In this section, the internal bypass channel configuration was the same as the "3-axes" system (Fig. 8(b)) described in the previous section, the center-to-center distance of the bypass channels was fixed at 4 mm, and tests were conducted under four conditions: a circular bypass channel with a diameter of 2 mm, as described in the previous section (Fig. 10(a), henceforth "circular (2 mm)"), a square channel with a cross-sectional area of 2 mm on each side (Fig. 10(b), "square (2 mm)"), and two cases where the diameter and side of the bypass channel were respectively expanded to 3 mm (Figs. 10(c), (d), henceforth, "circular (3 mm)" and "square (3 mm)"). For all bypass channel conditions, the members with bypass channels were made using a 3D printer. The conditions for the "currently used" and "porous" used for comparison were the same as those described in the previous section.

Figure 11 shows the results of the aerodynamic noise measurements. Figure 11(a) plots the POA value with respect to the opening ratio of the bypass channel, where the opening ratio is calculated from the total opening area of the bypass channel relative to the bypass application area on the upper surface of the corner (10 mm × 128.5 mm). This figure shows that the POA value tended to decrease with increasing opening ratio of the bypass channel, and that among the samples evaluated in this study, those with an opening ratio of approximately 35% could achieve the same aerodynamic noise re-

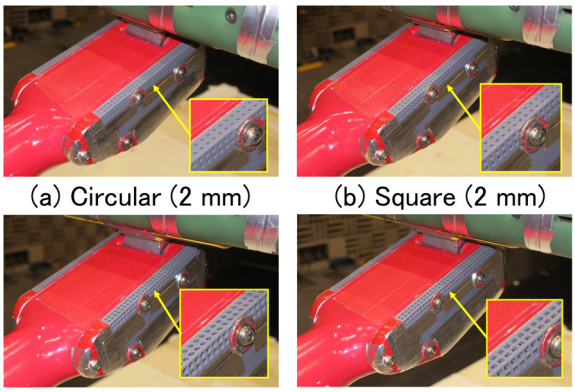

(a) Circular (2 mm) (b) Square (2 mm)

(c) Circular (3 mm) (d) Square (3 mm)

Fig. 10 Opening patterns of bypass channel

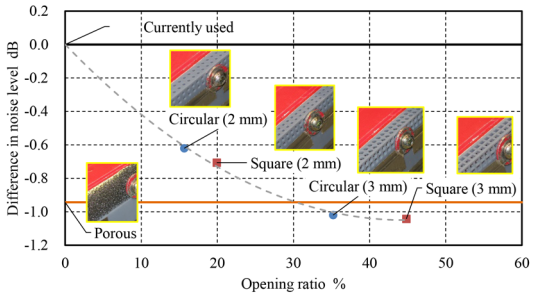

(a) Comparison of POA values

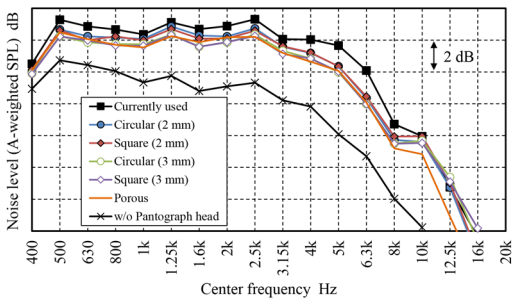

(b) Comparison of aerodynamic noise spectra

Fig. 11 Aerodynamic noise measurement results (wind tunnel test, 360 km/h)

duction effect as that obtained when a porous material is applied.

Referencing the comparison diagram of the aerodynamic noise spectrum (Fig. 11(b)), we could confirm that the noise level was reduced over a wide frequency range from 400 Hz to 8 kHz by applying the bypass channel, as stated in the previous section, and that the aerodynamic noise reduction effect was almost equal to that of the "porous" material for the "circular (3 mm)" and "square (3 mm)" materials with large opening ratios. No significant differences were observed between circular and square channels with similar cross-sectional dimensions, except for slight differences in the POA value and aerodynamic noise spectrum due to differences in the opening ratio. Therefore, the results indicate that the aerodynamic noise reduction effect does not depend significantly on the cross-sectional shape of the bypass channel.

4.3 Aerodynamic noise reduction effect of prototype with actual specifications

Given the study results up to the previous section, the device shown in Fig. 12 was prototyped as an aerodynamic noise reduction device with actual specifications, where we confirmed its aerodynamic noise reduction effect [8]. This device was constructed by making channels in an aluminum plate with a thickness of 10 mm, considering the strength of the members, and the area of the channel was the same as that described in the previous section, with a width W = 10 mm and height H = 10 mm, but the length in the ridge direction was slightly reduced to L = 121.5 mm owing to workability constraints. The results of Section 4.1 confirmed that the direction of the flow channel did not considerably influence the aerodynamic noise reduction effect, so a 2-axis type was selected in which the flow channels were made only in the two directions of "direction 1" and "direction 2," considering the workability of the member. As the results of Section 4.2 also indicated that the size and shape of the bypass channels must ensure an opening ratio of approximately 35%, circular bypass channels with a diameter of 3 mm were arranged with a center-to-center distance of 4 mm. This device was designed to be installed by fastening it to the head support. The device can be independently removed for inspection and replacement during repair, so maintenance is easier than that with porous materials that require adhesive installation. The mass is approximately 300 g for both sides, which is sufficiently small compared to the equivalent mass of the upper frame and is not expected to have a large impact on the current collection performance.

We evaluated the aerodynamic noise reduction effect by applying this method to three types of pantograph head and head support conditions, and the aerodynamic noise reduction effect was compared with that of a support cover with metal porous material developed in a previous study [3] (Fig. 3, area covered by porous material was width W = 10 mm, height H = 40 mm, and length L = 140.3 mm in the ridge direction). The pantograph head and head

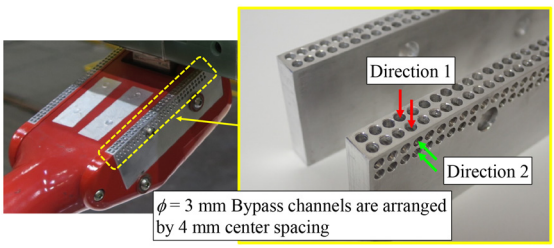

Fig. 12 Aerodynamic noise reduction device with actual specifications

support conditions were as follows: "condition 1," where both the pantograph head and head support were the currently used products; "condition 2," where only the pantograph head was changed to a multi-segmented smooth-profile pantograph head in "condition 1"; and "condition 3," where an improved head support was applied to "condition 2." For all conditions, the reference condition of the support cover was the currently used support cover. The multi-segmented smooth-profile pantograph head and improved head support were modified from those proposed in previous research (Fig. 3), with slight changes to the external shape [9]. Furthermore, in this section, we sought to evaluate the aerodynamic noise of the pantograph during actual running by sealing the gaps between the pantograph head elements of the multi-segmented smooth-profile pantograph head with soft fur material [3] instead of aluminum tape in order to allow for mobility, and the overall noise was evaluated using the OA value instead of the POA value. This resulted in a slightly smaller aerodynamic noise reduction effect than that indicated in the previous section.

Figure 13 shows the aerodynamic noise measurement results. This figure confirms that the aerodynamic noise was reduced over a wide frequency range above 630 Hz by applying the proposed device (bypass channel) for all the pantograph head and head support conditions. The reduction in the OA value obtained using this device was 0.3-0.4 dB, which was slightly smaller than the aerodynamic noise reduction effect of the porous material (0.4-0.5 dB), but it could be said that almost the same aerodynamic noise reduction effect was obtained. Although the effect on the OA value was small, the results showed that when applying this device a weak peak noise in the 12.5 kHz band was generated. This peak noise was inferred to be the air resonance sound that is specific to the 2-axis type channel configuration confirmed in Section 4.1. In the study conducted in this section, where the opening ratio of the channel was increased in comparison to the study conducted in Section 4.1, the peak noise was thought to have occurred more prominently with increasing flow rate through the bypass channel.

The above results confirmed that the proposed device generated a weak peak noise in the 12.5 kHz band, but that it could achieve an aerodynamic noise reduction effect that was almost equivalent to that of a porous material applied under various pantograph head and head support conditions.

5. Summary

In this study, we proposed a method for bypassing the flow in high-speed train pantographs by inserting a flow channel at the corner of a member. It is a practical alternative method to porous materials that is based on its aerodynamic noise reduction mechanism. This achieved a similar effect to the porous material while improving member strength and maintainability. We also conducted a wind tunnel test to confirm the aerodynamic noise reduction effect. From the results, the following conclusions were drawn:

(1)Aerodynamic noise was reduced by making a bypass channel connecting the upper and lateral surfaces of the head support.

(2)Studies on the direction of the bypass channels showed no large differences in the aerodynamic noise reduction effect between a 2-axes type with a bypass channel perpendicular to the upper and lateral surfaces, and a 3-axis type with an additional bypass channel in the ridge direction. However, the 2-axes type generated a weak peak noise that was inferred to be the air resonance sound related to the depth dimension of the bypass channel.

(3)Studies on the opening ratio of the bypass channel showed

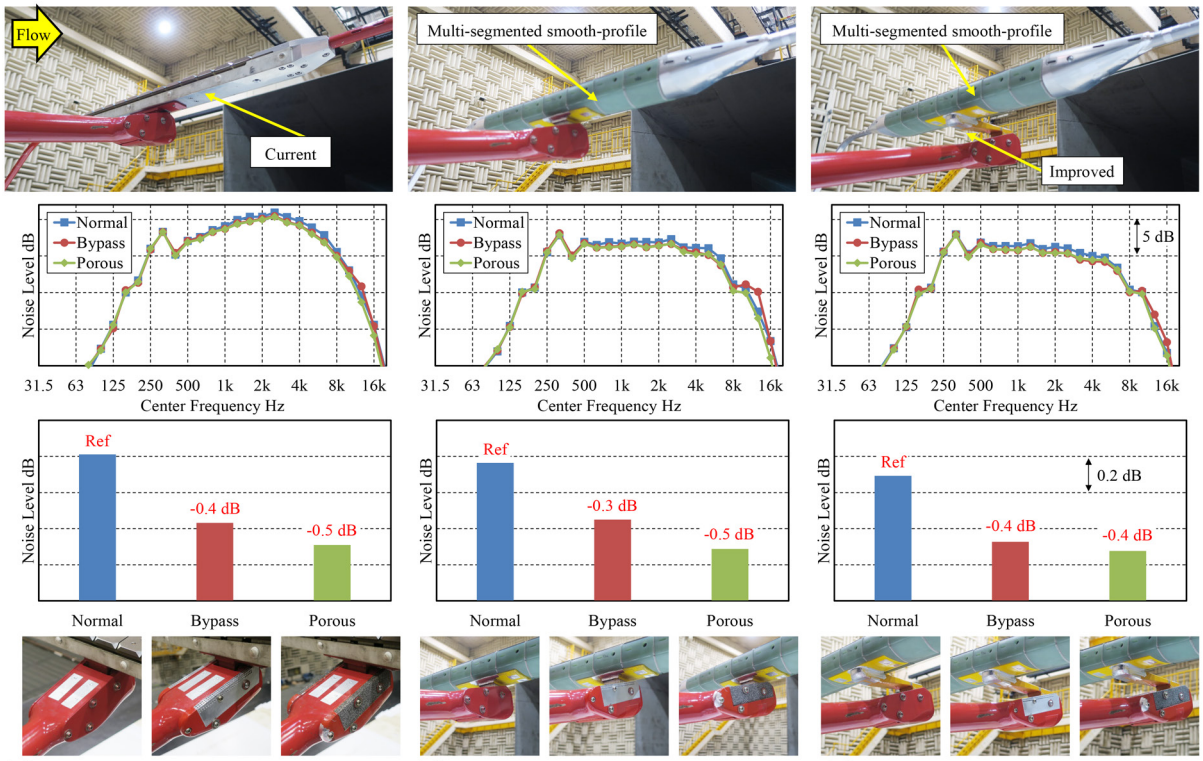

(a) Condition 1 (current pantograph head + currently used head support)

(b) Condition 2 (smooth-profile pantograph head + currently used head support)

(c) Condition 3 (smooth-profile pantograph head + improved head support)

Fig. 13 Aerodynamic noise measurement results (wind tunnel test, 360 km/h)

that among the samples evaluated in this study, an opening ratio of approximately 35% could achieve an aerodynamic noise reduction effect that was approximately equivalent to that of porous material.

(4)We developed a device with bypass channels in an aluminum plate as an aerodynamic noise reduction device with actual specifications, and we evaluated its aerodynamic noise reduction effect. Results showed that an aerodynamic noise reduction effect of 0.3-0.4 dB was achieved, which was approximately equivalent to that of porous materials, for three representative types of pantograph head and head support conditions.

In addition to pantographs, this method could be applied to a variety of equipment and members as a practical aerodynamic noise reduction measure that could replace porous materials.

References

[1] Yoshida, K., Suzuki, M., Ikeda, M., "Study on Optimization of Panhead Shape for Low Noise Pantograph," *RTRI Report*, Vol. 19, No. 9, pp. 23-28, 2005 (in Japanese).

[2] Usuda, T., Kobayashi, S., Yamashita, Y., Mitsumoji, T., Nagao, K., Wakabayashi, Y., "The Contact Mechanism of Multi-segment Pantograph Head and Compensation Method for Lift Force," *RTRI Report*, Vol. 34, No. 8, pp. 5-10, 2020 (in Japanese).

[3] Mitsumoji, T., Usuda, T., Hirakawa, H., Isono, T., Nagao, K., Wakabayashi, Y., "Aerodynamic Noise Reduction of Pantograph by Applying Smooth Profile Pantograph Head and Improving Pantograph Head Support," *RTRI Report*, Vol. 34, No. 8, pp. 11-16, 2020 (in Japanese).

[4] Hirakawa, H., Mitsumoji, T., Usuda, T., Saga, S.," Ice block impact test of metallic porous material for reducing aerodynamic noise of pantograph," presented at *the 26th Jointed Railway Technology Symposium (J-RAIL 2019)*, 2019 (in Japanese).

[5] Takaishi, T., Sueki, T., "Numerical Analysis of Aerodynamic Noise Reduction by Applying Porous Materials," *Transactions of the Japan Society of Mechanical Engineers*, Vol. 77, No. 773, pp. 33-42, 2011 (in Japanese).

[6] Mitsumoji, T., Hirakawa, H., Akutsu, M., Kobayashi, S., Wakabayashi, Y., "A study for alternative technique of porous material aimed at aerodynamic noise reduction of pantograph head support," presented at *the 31th Symposium on Environmental Engineering 2021*, 2021 (in Japanese).

[7] Mitsumoji, T., Amano, Y., Akutsu, M., Kobayashi, S., Wakabayashi, Y., "A study on aerodynamic noise reduction effect of pantograph head support by applying alternative method of porous material," presented at *the 32th Symposium on Environmental Engineering 2022*, 2022 (in Japanese).

[8] Mitsumoji, T., Usuda, T., Kobayashi, S., Nagao, K., Amano, Y., Wakabayashi, Y., "Reduction of Aerodynamic Noise Emitted from Pantograph by Applying Multi-Segmented Smooth Profile Pantograph Head and Low Noise Pantograph Head Support," *Lecture Notes in Mechanical Engineering*, pp. 209-217, 2024. https://doi.org/10.1007/978-981-99-7852-6_19

[9] Mitsumoji, T., Amano, Y., Abe, T., "Achieving a quiet pantograph," *RRR*, Vol. 81, No. 2, pp. 20-25, 2024 (in Japanese).

Authors

Takeshi MITSUMOJI
Senior Researcher, Current Collection Laboratory, Railway Dynamics Division
Research Areas: Aerodynamics of Pantograph

Yuki AMANO, Ph.D.
Researcher, Current Collection Laboratory, Railway Dynamics Division
Research Areas: Catenary-Pantograph Interaction, Dynamics of Machinery, Mechanical Vibration

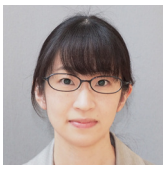

Mariko AKUTSU, Ph.D.
Assistant Senior Researcher, Noise Analysis Laboratory, Environmental Engineering Division
Research Areas: Railway Noise, Acoustics

Kyohei NAGAO
Assistant Senior Researcher, Current Collection Laboratory, Railway Dynamics Division
Research Areas: Catenary-Pantograph Interaction, Dynamics of Machinery, Mechanical Vibration

Isamu MAKARA
Assistant Senior Researcher, Current Collection Laboratory, Railway Dynamics Division (Former)
Research Areas: Aerodynamics of Pantograph, Catenary-Pantograph Interaction

Yusuke WAKABAYASHI, Ph.D.
Chief Researcher, East Japan Railway Company, Next-generation Rolling Stock System Unit, Research and Development Center of JR East Group
Research Areas: Aerodynamic Noise Reduction

Summaries of Papers in RTRI REPORT (in Japanese)

Evaluation of Aerodynamic Noise and Intake Flow Rate of Running Wind Intake by Wind Tunnel Experiment

Yuto ARAKI, Hajime TAKAMI, Akihito KIMURA, Yoshinari YAMAZAKI, Hiromu UMEDA
(Vol.39, No.5, 1-5, 2025.5)

In order to cool the equipment installed under Shinkansen trains, running air is used directly instead of fans. A wind tunnel experiment was conducted to evaluate the shape of the intake, which can draw in a large amount of flow and reduce aerodynamic noise. In the wind tunnel experiment, five types of intake shape were examined using a model to measure the flow velocity inside the duct and the noise generated by the intake. The results showed that the intake flow rate was affected by the shape of the opening and that the aerodynamic noise generated was reduced by rounding the lip of the intake. We also found that placing protrusions or dimples near the lip increased the intake flow rate and the aerodynamic noise. Changing the position of the dimple, rather than making it shallower, also increased the intake flow rate and reduced the increase in aerodynamic noise.

Numerical Analysis of the Hydrogen Leakage from a Fuel Cell Railway Vehicle Stationed in a Tunnel

Takashi FUKUDA, Sanetoshi SAITO
(Vol.39, No.5, 7-12, 2025.5)

One of the initiatives to decarbonize railways is the development of fuel-cell vehicles. However, to put fuel-cell railway vehicles into practical use, it is necessary to confirm their safety, and one particularly important issue is the evaluation of hydrogen concentration in the event of a hydrogen leak in a tunnel. In this study, a numerical analysis was performed to investigate the hydrogen leak flow from a stationary railway test vehicle consisting of a two-car train set with a hydrogen leak in its roof equipment in a tunnel. The tunnel was a single-track, 400 m long mountain tunnel on a conventional Japanese railway. The Fire Dynamics Simulator (FDS) was used for the numerical analysis. The results showed that the leaked hydrogen rose towards the crown of the tunnel and flowed towards both tunnel portals. The hydrogen concentration was the highest immediately above the leak point and decreased rapidly towards both tunnel portals. In addition, the influence of the location of the leak on the hydrogen concentration distribution was also shown.

The Influence Analysis Method of a Shield Tunnel under Construction Extremely Close to an Existing Tunnel

Akihiko MIWA, Tatsuki SHIMIZU, Takashi NAKAYAMA
(Vol.39, No.5, 13-20, 2025.5)

This paper proposes a new numerical analysis method for neighboring construction where a new shield tunnel is excavated under an existing tunnel with a short distance. These tunnels are mathematically modeled using detail 3D shell elements and the ground between the tunnels is modeled using interaction springs. The strength of the interaction springs is determined using stability calculations of the ground above the new shield tunnel. We conducted the trapdoor test that reproduces this neighboring construction and measured the interaction between the intersecting tunnels. The results confirmed that the proposed analysis method can simulate the test result of ground reaction forces and tunnel deformation.

Searching for Sources of Unpleasant Odors in Men's Restrooms in Railway Stations and Verifying the Effectiveness of Countermeasures to Reduce Them

Takashi KYOTANI, Tamami KAWASAKI, Akiko KAMEDA, Tsuyoshi UEDA
(Vol.39, No.5, 21-28, 2025.5)

Unpleasant odors in restrooms in railway stations and on trains are one of the many complaints from railway customers, so there is a need to reduce such odors. We are investigating the sources of ammonia, one of the main unpleasant odorous compounds in public restrooms, in men's restrooms in railway stations. For the investigation, we prototyped a portable, highly sensitive ammonia measuring instrument. We used this instrument to search for the sources of ammonia in men's restrooms in railway stations and confirmed the difference in concentration of ammonia depending on cleaning methods and seasons. In addition, we verified the effectiveness of countermeasures to reduce unpleasant odors implemented by cleaning companies.

Method for Verifying Structural Safety of Steel/Composite Girder against Overturning and Lifting and Its Effect on Design

Nodoka MIYAKE, Yusuke KOBAYASHI, Manabu IKEDA
(Vol.39, No.5, 29-34, 2025.5)

In the design of railway steel girders, it is necessary to prevent overturning and lifting of the girder against possible forces acting on the girder. This paper outlines a verification method against the two limit states of girder overturning and girder lifting, and describes a revised method of calculating the lifting force that takes into account the vibration characteristics of the girder. A trial design of the bearing parts was also carried out using the revised calculation method. The result confirmed that the revised calculation made some parts of the bearing smaller.

Verification Method for Friction Joints Using High-Strength Bolts and Its Effect on Design

Nodoka MIYAKE, Yusuke KOBAYASHI
(Vol.39, No.5, 35-40, 2025.5)

Friction joints using high strength bolts, which are commonly used in the connection of steel structures, resist tensile forces by friction on the contact surface between the bolted plates. This paper outlines a revision of the method of setting the coefficient used to calculate the resistance force. The trial design of the joint was carried out using the revised coefficients. The result confirmed that the new coefficients are effective in reducing the number of bolts. A method for verifying the failure of the jointed plates in the event of tearing and the conditions under which tearing is likely to occur is also outlined.

A Survey of Hearing Tests for Drivers Using Whispered Voices

Kei HOSHINO, Ayano SAITO, Hiroaki SUZUKI, Etsuo KASAHARA, Naotoshi YAMAMOTO
(Vol.39, No.5, 41-44, 2025.5)

In order to obtain a train driver's license, you have to pass a physical examination. The standard for hearing in the physical examination states that "each ear must be able to hear whispered words clearly at a distance of 5 meters," but the specific method of measurement is not clear, nor is the relevance to the audiometer test method used by JR. A survey was conducted to understand the reality of hearing tests using whispered voices. The results confirmed that the peak sound pressure level of a whisper voice is

around 1000Hz, and that the A-weighted sound pressure level in this frequency band is generally 30 dB to 40 dB, which is roughly consistent with the results of audiometer tests.

Applicable Conditions of Polyurea Resin Spraying Method for Seepage and Uneven Surface of Tunnel Lining

Atsuya OE, Keisuke SHIMAMOTO, Tomoya USHIDA, Kazuhide YASHIRO, Masayuki SUZUKI
(Vol.39, No.5, 45-53, 2025.5)

If a piece of tunnel lining falls off and hits a train, it could lead to an accident, so great care is taken every day during tunnel maintenance to prevent this from happening. Repairs are planned and carried out in areas where there is a potential risk of future spalling. We have developed a method, called the "polyurea resin spraying method," to prevent spalling of the lining by spraying polyurea resin on the surface of the tunnel lining. This paper presents the results of a study carried out to extend the applicability of this method and some construction examples: the effect of surface moisture during application on the bond strength of the resin, the long-term durability in a seepage environment, and the bond strength of the resin in an uneven surface environment, as well as the results of its application in a real tunnel.

Derailment Detection of Freight Wagon Using Mechanical Contact Sensors

Shogo MAMADA, Tatsuya OTA, Kohei MIYAHARA, Kazuto KOSUGI
(Vol.39, No.6, 1-9, 2025.6)

In long freight trains, if a freight wagon derails away from the locomotive, there may be a delay in detecting the derailment. In such cases, there is a concern that the wagons may continue to run while derailed, causing severe damage to track components, and therefore there is a need for early detection of wagon derailment. Therefore, the authors investigated a derailment detection method using mechanical contact sensors as one of several methods, since the contact sensors is too useful to detect wagon derailment. In this study, based on the results of past accident investigations and simulation results, two locations on the bogie of a wagon were selected as suitable locations for the installation of contact sensors. In addition, in order to evaluate the derailment detection performance of the proposed method, derailment tests on actual tracks were carried on freight wagons using bogies with contact sensors. The test results showed that the proposed method using contact sensors could detect a derailment immediately after it occurred.

Method for Evaluating Running Safety of Railway Vehicles during Earthquake Using Extensive Characteristics of Seismic Track Vibrations

Kohei IIDA, Kengo NANAMI, Masahito KUZUTA
(Vol.39, No.6, 11-16, 2025.6)

This paper proposes a method for evaluating the running safety of a railway vehicle during an earthquake taking into account the characteristics of seismic waveforms and structures. Firstly, the characteristics of seismic track vibration taking into account both earthquakes and structures are derived from the measured data of past earthquakes and a wide range of structural natural periods. Secondly, the running safety index for seismic wave is calculated from the characteristics of the seismic track vibration and the running safety limit diagram for sinusoidal excitation. It is confirmed that the running safety index has a roughly linear relationship with the estimated derailment occurrence probability during earthquakes using the method described in a previous paper.

Load-bearing Mechanism of Beam-column Joints of Rigid Frame Viaducts Subjected to Horizontal Forces in Two Directions

Ryota KONISHI, Yuki NAKATA, Ken WATANABE
(Vol.39, No.6, 17-25, 2025.6)

In order to clarify the load-bearing mechanism and load-bearing capacity of the joint under two-way loading, we investigated the beam-column joint of a ridged frame viaduct by finite element analysis. The inner radius of axial rebars in the transverse beam affected the load-bearing capacity of the joint, since a compressive strut was formed at the bending inner radius of the bend when the load angle was around 0°. The tie reinforcing bars at in the joint had the effect of increasing the load-bearing capacity by up to 10% in any loading direction. In addition, when the torsional moment of the longitudinal beam was considered, the horizontal force was shared at each fulcrum, but it did not affect the joint bearing force.

Application of Image Analysis Engine around Railway Track to Night Vision Images

Atsushi SHIMIZU, Shintaro MINOURA
(Vol.39, No.6, 27-33, 2025.6)

We developed a method for capturing and analyzing images using images captured at night by a stereo camera. We also verified the feasibility of using the developed methods for platform limit measurement and difference detection of the environment around railway. The result confirmed that by combining infrared light projectors with different irradiation angles and irradiation distances, it is possible to capture a clear image of the rail periphery while capturing the general shape of the image as a whole. We also developed a method for measuring the distances around the platform and examined the measurement accuracy. The average error was less than 20 mm. Furthermore, by setting appropriate parameters, we confirmed that the difference detection can be properly performed even for night vision images.

Numerical Analysis on the Contribution of Each Member to Structure-Borne Sound in Reinforced Concrete Rigid-Frame Viaducts

Tsutomu WATANABE, Toki UDA, Mariko AKUTSU, Tamiko SEINO
(Vol.39, No.6, 35-41, 2025.6)

In this study, a numerical experiment was carried out using a finite element modelling to quantify the contribution of each member to structure-borne sound. As examples of specific results, the contribution to the overall value at the 25m point on a reinforced concrete (RC) rigid frame viaduct was 73% for the center slab, 10% for the soundproof wall, and 17% for the cantilever slab. In addition, the contribution of the RC rigid frame viaduct and the adjacent RC girders was 67% and 33% respectively. This indicates that not only the rigid frame viaduct but also the RC girder may have a relatively large contribution to structure-borne sound along the railway line.

Diagnosis of Engine Condition with an Oil Condition Monitoring System

Junichi SUZUMURA, Sadayuki KIKAWA, Kazuki IKOMA, Tatsuro TAKASHIGE
(Vol.39, No.7, 1-8, 2025.7)

The authors have developed an on-board lubricating oil condition monitoring system, for diesel-powered vehicle, consisting of an oil analyzer and a date logger capable of communicating with an external terminal via Wi-Fi. The performance of the system was evaluated using a bench test which artificially simulates internal engine wear and an on-track test using a commercial vehicle. The results of the tests showed that the monitoring system operated normally and was able to detect an increase in the concentration of

iron powder in the engine oil.

Influence of Nonlinearization of Ground and Structure on Combination of Inertia Force and Ground Deformation Used in Seismic Deformation Method

Niki TANAKA, Kimitoshi SAKAI

(Vol.39, No.7, 9-18, 2025.7)

In order to improve the accuracy of combining inertia force and ground deformation when using the seismic deformation method, we focused on the respective nonlinear behavior of the ground and the structure. Specifically, dynamic analyses were conducted for various types of grounds and structures under the condition that one of them became nonlinear, and the combination coefficients for the ratio of the period of grounds to the period of structures were calculated. As the result, we confirmed that the variation of the combination of actions was reduced by considering not only the relationship between the natural period of grounds and structures, but also the degree of nonlinearity of each. Based on these results, we proposed a new method which simply takes into account the degree of plasticization of the ground and structure. Using the proposed method, it is possible to determine more appropriate combination coefficients of ground deformation and inertial force than conventional methods.

Effect of Interaction between Bedrock and Surface Layer on the Predominant Period of Surface Layer

Kimitoshi SAKAI

(Vol.39, No.7, 19-25, 2025.7)

A study was conducted to understand the effect of engineering bedrock on the predominant period of surface layer. The results confirmed that even when the natural period T_g derived from eigenvalue analysis is the same, the interaction with engineering bedrock can cause significant changes in the predominant period and ground motion. Additionally, it was clarified that the influence of engineering bedrock is likely to shorten the predominant period compared to T_g when the natural periods of the first and second modes from eigenvalue analysis are relatively close or when the shear stiffness of the surface layer is relatively large. We have proposed a method to easily correct this tendency, and have confirmed that it can estimate the dominant period of the ground more accurately. It is expected that the insights obtained in this study will improve the accuracy with which the predominant period of ground during earthquakes can be estimated, and enable ground motion to be evaluated while taking into account the uncertainty of the predominant period.

An Implementation and Verification on a Model for Predicting Level of Train Congestion during Disruptions

Hiroto UEDA, Kosuke NAKABASAMI, Taketoshi KUNIMATSU

(Vol.39, No.7, 27-32, 2025.7)

In recent years, train operators have started to provide real-time information on the levels of congestion on trains to improve customer satisfaction. However, during disruptions such as train service cancellations or schedule changes, the levels of congestion are different from the norm. At such times, it would be beneficial for passengers to receive information about future congestion, since it would help them decide whether or not to change trains. In this study, we developed a model to predict congestion levels during disruptions. The test of the developed model confirmed that it was possible to predict the level of congestion with around 75% accuracy by using features such as the level of congestion at one to three stations and the headway ahead of the train.

Development of an Inspection Support System Using Tunnel Wall Images

Takashi NAKAYAMA, Yudai YAMASHITA, Kazuhide YASHIRO

(Vol.39, No.7, 33-39, 2025.7)

Regular inspections are required for the maintenance of railway tunnels. Inspectors determine soundness through visual inspection and hammering test to ensure proper maintenance. With a predicted decline in the labor force, there is a growing need for the digitization and automation of tunnel inspections. In this study, we developed two technologies to address this need. The first is an “Automatic Tunnel Condition Assessment System,” and the second is a “Critical Area Projection System.” This paper describes the overview and verification results of each system.

QUARTERLY REPORT of RTRI

第 66 巻　第 3 号
2025 年 8 月 1 日　発行
監修・発行所：公益財団法人鉄道総合技術研究所
〒 185-8540　東京都国分寺市光町 2-8-38
発行人：芦谷公稔
問い合わせ：鉄道総研広報

Vol. 66, No. 3
Published date: 1 August 2025
Supervision/Publisher: Railway Technical Research Institute
Address: 2-8-38 Hikari-cho, Kokubunji-shi, Tokyo 185-8540, Japan
Issuer: Dr. Kimitoshi ASHIYA
Contact us: Public Relations, Railway Technical Research Institute
Mail Address: rtripr@rtri.or.jp

QUARTERLY REPORT of RTRI

RAILWAY TECHNICAL RESEARCH INSTITUTE

Printed in Japan